Synthesis of Metal Oxide/Sulfide Monoliths for Photocatalytic Degradation of Organic Pollutants

Thesis submitted for the award of degree of

Doctor of Philosophy

by

Surbhi Sharma

Regn No. 901709009

Under the guidance of

Dr. Soumen Basu

Professor

THAPAR INSTITUTE
OF ENGINEERING & TECHNOLOGY
(Deemed to be University)

School of Chemistry and Biochemistry
Thapar Institute of Engineering & Technology
Patiala-147004

November 2022

Certificate

This is to certify that thesis entitled "**Synthesis of Metal Oxide/Sulfide Monoliths for Photocatalytic Degradation of Organic Pollutants**", being submitted by Ms. Surbhi Sharma in fulfilment of the requirement for the award of the Degree of Doctor of Philosophy in the School of Chemistry and Biochemistry, Thapar Institute of Engineering and Technology, Patiala, is a record of candidate's own independent and original research work carried out by her under my supervision and guidance. The matter presented in the thesis has not been submitted in part or full for the award of any degree in any other University or Institute.

SBasu

(Supervisor)
Prof. Soumen Basu
Professor
School of Chemistry and Biochemistry
Thapar Institute of Engineering and Technology
Patiala-147004, Punjab, India

(Head) 18/7/2022
Prof. Satnam Singh
Professor
School of Chemistry and Biochemistry
Thapar Institute of Engineering and Technology
Patiala-147004, Punjab, India

Candidate's Declaration

I, hereby declare that the present work in the thesis entitled "**Synthesis of Metal Oxide/Sulfide Monoliths for Photocatalytic Degradation of Organic Pollutants**" in the fulfilment of the requirement for the award of the Degree of Doctor of Philosophy in the School of Chemistry and Biochemistry, Thapar Institute of Engineering and Technology, Patiala, is an authentic record of my own work carried out under the supervision of Prof. Soumen Basu, Professor, School of Chemistry and Biochemistry, Thapar Institute of Engineering and Technology, Patiala, India. The matter embodied in thesis has not been submitted in part or full to any other University or Institute for the award of any degree in India or Abroad.

Surbhi Sharma

………………

Surbhi Sharma

Acknowledgements

First and foremost, I devotedly thank the Almighty for giving me strength, courage, patience, resilience and perseverance to accomplish this project.

Through this section of the thesis, I would like to acknowledge each individual who has been a part of my journey and has directly or indirectly contributed to my research work.

I want to express sincere gratitude to my supervisor **Prof. Soumen Basu** for providing me with the opportunity to work on this project and for his constant support and encouragement. The insightful discussions, continuous guidance, and priceless suggestions throughout the experimental and thesis works have been beneficial. I thank him for always keeping faith in me and inspiring me to do better in my life.

I am eternally grateful to **University Grants Commission, New Delhi, India**, for the research fellowship.

I am incredibly thankful to **Prof. Prakash Gopalan**, Director, and **Prof. Rafat Siddique**, Dean of Research & Sponsored Projects, Thapar Institute of Engineering and Technology, Patiala. My sincere gratitude to **Prof. Satnam Singh**, Professor and Head, School of Chemistry and Biochemistry, Thapar Institute of Engineering and Technology, for his ever-helping attitude and best wishes. I would also like to thank my doctoral committee members, **Prof. O. P. Pandey, Prof. Bonamali Pal,** and **Dr. Davinder Kumar**, for the scientific discussions and valuable suggestions that have always been very helpful. I also want to acknowledge all the faculty members in the School of Chemistry and Biochemistry for their cooperation and support. I express my sincere gratitude to Mr. Mayank Sharma for his constant official help and cooperation. I also want to thank Mr. Chander Thakur, Mr. Hemant Sharma, Mr. Vishwanath, Mr. Shekhar for their support. I am grateful to Mr. Shashi Grover for his official support and cooperation.

I want to thank everyone who helped with instrumental facilities; SAI Labs, TIET Patiala; ACIRD, TIET, Patiala; Sprint testing solutions, Mumbai; CIL, PU, Chandigarh; CeNS Bangalore, IIT Roorkee, and JNU, New Delhi. I also want to thank Prof. Bonamali Pal for the DRS instrument, Dr. Amit Dhir for the TOC analysis, and Dr. Mily Bhattacharya for UV-Vis spectrophotometer.

I am grateful all my lab seniors, Dr. Manisha Sharma, Dr. Akansha Mehta, Dr. Amit Mishra, Dr. Jasminder Singh, and Dr. Shagun Kainth. I am also thankful to my departmental seniors, Dr. Amanpreet Kaur, Dr. Aadil Bathla, and Dr. Rayees Ahmad; special acknowledgement for Dr. Santosh Kumar Rath for being very kind and helping me with chromatographic analysis. I would like to acknowledge my lab-mates: Dr. Aanchal, Ms. Neeraj, Dr. Divya Monga, Ms. Aayushi, Ms. Shelly, Ms. Mansi Kapoor, Ms. Aashna, Ms. Anushka Garg, Mr. Zaid, Mr. Ranjeet Jha, and Mr. Pritam. I also want to thank other people who made this journey memorable; Ms. Sakshi Mittal, Ms. Janis Goyal, Mr. Parminder Singh, Ms. Komal Sharma, Ms. Aditi Dewan, Mr. Hemant Kerwal, Ms. Aashima, Mrs. Parmandeep Kaur, Ms. Geetika, and Ms. Palak Sharma. My friendship with my colleague, Dr. Aanchal, was a source of strength for me. We commenced this journey together, witnessed numerous ups and downs, and motivated each other for the best always. I also shared a genuinely special bond with Neeraj, who was my constant supporter. We always laughed together even in the most challenging times. My juniors: Shelly, Aayushi, Sakshi, Mansi, and Janis were always really sweet and respectful towards me. I have truly found a younger sister in Shelly during this journey who sincerely cares for me. The time spent in Advanced Nanomaterials Lab would be cherished by me forever. I also want to thank all my friends, particularly Jyoti and Mahima for always believing in me. My Ph.D. journey was definitely an experience of a lifetime and indeed a huge learning process for me in every aspect, making me a much stronger person.

My final and truly the most special 'thank you' is for my parents; **Smt. Renuka Sharma** and **Sh. Mehar Chand** and my brother **Mr. Udit Sharma**. I want to acknowledge the unmatchable support extended by them. They always kept faith in me and let me do things my way and were always there for me in every high and low phase of life. I have learnt discipline from my father and diligence from my mother. My father is truly my best friend and my biggest supporter. It is absolute truth that behind every successful girl, there is a progressive and supportive father. I also want to thank my grandparents for their blessings and best wishes. My brother, Udit Sharma, deserves a special mention here. The biggest credit goes to him for everything that I have achieved today. He sacrificed many of his important things and missed many of his important moments only so that I did not have to suffer or I didn't have to waste my time on other things. I don't think I would ever be able to repay whatever these 'three pillars of my strength' have done for me.

I am eternally thankful to everyone who has been a part of my journey and has knowingly or unknowingly helped me accomplish this work.

TABLE OF CONTENTS

CHAPTER 1
Introduction and literature review

CHAPTER 2

Visible-light active hierarchical porous WO_3/SiO_2 monolith in centimeter length scale for enhanced photocatalytic degradation of toxic organic pollutants

CHAPTER 3

Centimeter-sized Sb_2S_3/SiO_2 monoliths with 'mimosa pudica' flower-like morphology for photocatalytic detoxification of hazardous organic pollutants

CHAPTER 4

Visible-light-driven efficient photocatalytic abatement of recalcitrant pollutants by centimeter-length MoO_3/SiO_2 monoliths

CHAPTER 5

Efficient and durable hierarchical porous CuO/SiO$_2$ monolith for synergistically boosting the visible-light-driven degradation of organic pollutants

List of Figures

Chapter 3

Chapter 4

Chapter 5

List of Schemes

Scheme No. **Title** **Page No.**

Chapter 2

Chapter 3

Chapter 4

Chapter 5

List of Tables

Conclusions and future perspectives

List of Abbreviations

B. E.	Binding energy
BET	Brunauer-Emmett-Teller
BJH	Barrett-Joyner-Halenda
BOD	Biochemical oxygen demand
COD	Chemical oxygen demand
CVD	Chemical vapor deposition
CTAB	Cetrimonium bromide
DRS	Diffuse reflectance spectroscopy
EDS	Energy dispersive X-ray spectroscopy
FESEM	Field emission scanning electron microscopy
GC-MS	Gas chromatography-mass spectrometry
HRTEM	High resolution transmission electron microscopy
IC	Imidacloprid
JCPDS	Joint committee on powder diffraction standards
MB	Methylene blue
min	Minute
MZ	Metronidazole
PEG	Polyethylene glycol
PL	Photoluminescence
ppm	Parts per million
pzc	Point of zero charge

Rh-B	Rhodamine B
SEM	Scanning electron microscopy
TEOS	Tetraethoxysilane
TGA	Thermogravimetric analysis
TM	Thiamethoxam
TOC	Total organic carbon
UV- Vis	Ultraviolet-visible
XPS	X-ray photoelectron spectroscopy
XRD	X-ray diffraction

List of Symbols

%	Percentage
%D	Percent degradation or degradation efficiency
Å	Angstrom
A_0	Initial absorbance of pollutant
A_t	Absorbance of pollutant at a certain time
C_0	Initial concentration of pollutant
cm^3/g	Centimeter cube per gram
C_t	Concentration of pollutant at a certain time
E_g	Band gap energy
g	Gram
g/L	Gram per litre
h	Planck constant
k	Pseudo-first order rate constant, min^{-1}
M	Molar
mg	Milligram
mL	Millilitre
mM	Millimolar
nm	Nanometer
^{o}	Degree
R^2	Regression coefficient
S_{BET}	BET surface area, m^2/g

t	Time, min
V	Total pore volume, cm^3/g
α	Absorption coefficient
θ	Theta
λ	Wavelength
ν	Light frequency

Abstracts

Chapter 1

This chapter describes the importance of monolithic photocatalysts with hierarchical morphology and high surface to volume ratio. The negative facets of modernization including water pollution by industrial sources, domestic activities, etc., have been discussed in detail. The sources of hazardous organic pollutants, their impact of on environment, as well as the techniques of wastewater treatment are comprehensively illustrated. The brief introduction about photocatalysis and the significance of metal oxide/ sulfide monoliths as photocatalysts has been discussed The literature survey on the basis of monolithic materials as well as photodegradation of organic pollutants has been presented. In this respect, the realized research gaps were mentioned along with the objectives of the present research work.

Chapter 2

This chapter deals with the synthesis of hierarchical porous WO_3/SiO_2 monoliths by wet-impregnation of sodium tungstate in silica monoliths. The XRD spectra confirmed the successful formation of monolith and FESEM images exhibiting a connected porous network structure. The oxidation-state and uniform elemental-distribution were analyzed by XPS and EDS analyses, respectively. BET analysis showed that monoliths displayed multimodal porosity with pore-diameter of 0.70–14.71 nm and high surface area (82 m^2/g). UV- Vis DRS revealed that the monolith had a narrow band gap (~2.55 eV), which is suitable for visible light photocatalysis. The photocatalytic performance of monolith was estimated by degradation of model-pollutant MB under visible-light illumination. High photocatalytic efficiency (91%) and rate constant (0.013 min^{-1}) was observed at natural pH of the dye (pH 7.5). The effect of pH and catalyst concentration was explored which revealed that best degradation occurred at pH 3 (~97.5%) and catalyst concentration 0.4 g/L (~96%). The trapping experiments suggested that the holes were governing reactive-species in the reaction. The photocatalyst was reused for 5 consecutive cycles and manifested ~80% degradation. The characterization-results of monolith after 2nd cycle of

photodegradation explicated its stability. A colorless pollutant (IC) was also degraded to distinguish between direct and indirect photocatalysis.

Chapter 3

This chapter deals with the fabrication of ‘mimosa pudica’ flower-like Sb_2S_3/SiO_2 monoliths by impregnation of antimony chloride solution in silica monoliths followed by treatment with potassium thiocyanate, refluxing and calcination. The nanoflower-like morphology of the synthesized monoliths was verified using FESEM images. The surface area analysis showed that monoliths had a high surface area of 83 m^2/g with a mesopore diameter of 13.61 nm. The purity/crystallinity and the oxidation state of the sulfide were confirmed using X-ray diffraction analysis and XPS spectroscopy whereas EDS with elemental mapping verified the homogeneous elemental distribution of the catalyst. The UV-Vis DRS and PL spectroscopy confirmed that Sb_2S_3/SiO_2 monoliths had a narrow band gap (~1.57 eV) and low recombination rate of photoinduced charge carriers. Thermal stability of the materials was also investigated by thermogravimetric analysis. The photocatalytic performance of monoliths was examined by photodegradation of model pollutants MB and TM. At optimum pH and catalyst-concentration, monoliths exhibited best efficiency (with high rate-constant) in sunlight for degradation of MB (96%; 0.018 min^{-1}) and in UV light for degradation of TM (70%; 0.0057 min^{-1}). The catalyst was reused for four cycles for degrading MB (~71% efficiency). The trapping experiments indicated that superoxide anion radicals and holes had a dominant role in the MB and TM degradation, respectively.

Chapter 4

In this chapter, MoO_3/SiO_2 monoliths were prepared by wet-impregnation route. The crystallinity of the catalyst and oxidation-state of elements were revealed by XRD and XPS analyses, while EDS and color-mapping confirmed the uniform dispersal of elements in the catalyst. FESEM and HRTEM analyses revealed the highly porous surface of monolith and small particle size whereas BET-analysis revealed its pore-size (~15.05 nm) and excellent surface-area

(~202 m^2/g). The optical properties disclosed that MoO_3/SiO_2 monoliths were visible-light-active having band-gap ~2.58 eV and a low recombination-rate. The photoactivity of the catalyst was checked through photodegradation of model dye Rh-B and antibiotic MZ. Under visible-light-irradiation, and at natural-pH, excellent efficiency was obtained for Rh-B (88.6%; 0.0129 min^{-1}) and MZ-degradation (67.4%; 0.0054 min^{-1}). Similar experiments in sunlight manifested better efficiency. High reusability of catalyst (~9%-reduction in efficiency after 4-runs) was justified by post-photocatalytic characterization-results. The trapping-experiments displayed that holes had primary involvement in the degradation. The intermediate products of MZ after photodegradation were identified by GC–MS analysis. The photocatalytic treatment of real wastewater (without physicochemical-treatment) showed ~64% COD-removal and 57% TOC-removal.

Chapter 5

In this chapter, hierarchical porous CuO/SiO_2 monoliths were constructed via the wet-impregnation method. The crystalline nature of the prepared material was confirmed through XRD while XPS analysis was carried out to find out the chemical bonding states of the elements. EDS and elemental-mapping confirmed the successful formation of the material and a homogeneous dispersion of elements. SEM images exhibited the interconnected porous network morphology of the monoliths while the surface area analysis affirmed that the monoliths were hierarchical porous along with a substantial surface-area of ~286 m^2/g. Optical properties demonstrated that the material was visible-light-driven having a small band-gap of ~1.33 eV as well as a slow e^-/h^+ recombination-rate. The maximum removal efficiency of 90.5% with a rate constant of 0.01255 min^{-1} was realized for Rh-B at optimal conditions, whereas for TM, ~55% degradation occurred with a rate constant of 0.00443 min^{-1}. The highly reusable feature of the monolith (~12%-reduction in efficacy post 5 cycles) was justified by the XRD, surface area and SEM analyses after the photocatalytic experiment. Around 60% Rh-B and 20.05% TM was mineralized after the photocatalytic reaction as estimated through TOC analyses. The scavenger experiments revealed that holes were chiefly involved in the reactions.

Chapter 1

Introduction and literature review

1.1 Introduction to nanoscience and nanotechnology

Nanoscience and nanotechnology are the latest advancements in the domain of science and engineering that are scaling quite quickly and enable evolutionary transformations in different areas. The driving force for this advancement is the desire to fabricate materials with novel and enhanced features that are probable to influence nearly all extents of the physical sciences, chemical sciences, and life sciences. Nanomaterials are commonly known as materials that have at least one external dimension ≤ 100 nm and could exist as particles, tubes, rods or fibres.[1,2]

1.2 Porous materials

Any solid substance comprising of empty spaces that are not occupied by the main skeleton of atoms that constitute the overall solid structure.[3] The interconnected pores facilitate the interaction amongst different atoms, molecules, and ions at the surface and the bulk of the material. These properties render the porous materials useful in the domain of adsorption,[4] catalysis,[5] photocatalysis,[6] ion-exchange,[7] sensing applications,[8] energy storage,[9] etc. Various examples of porous materials are clays, rocks, ceramic materials, etc. Inorganic porous materials offer more advantages than polymeric substitutes, such as higher mechanical strength, thermal stability, and chemical durability.[10]

The porous materials are classified into different categories based on pore size as per IUPAC pore classification, which includes micropores (pore diameter < 2 nm), mesopores (2 nm < pore diameter < 50 nm), and macropores (pore diameter > 50 nm).[11] Silica-based materials have garnered particular attention amongst different porous materials owing to the flexible state provided by silica which eventually permits a superior control of mesostructures.[12] Considering the source and structure of pores, they can be further classified into intraparticle pores that are structurally intrinsic pores. Another type is extrinsic pores that could as well be interparticle pores.[13] Certain porous solids are consolidated and exist as comparatively stiff, macroscopic bodies whose dimensions surpass those of the pores by many folds of magnitude and are called agglomerates. Other porous solids are unconsolidated and exist as non-rigid, more or less slackly packed groupings of discrete particles, and could be called aggregates **(Fig. 1.1(a))**. These particles could themselves be non-porous and bounded by a web of interparticle voids (for e.g., sand) and the characteristics of these void depend not only on the size and shape and packing of the constituent particles. Commonly, internal pores are smaller in size and in total volume as compared to the voids between particles but contribute chiefly toward the overall surface area of the material. Both the pore dimension as well as pore connectivity are crucial for properly understanding the physical process undergoing in a reaction and predicting the transport and reaction functioning. The pore dimension involves the shape of pore along with of pore size distribution. The pore connectivity depicts the manner in which the pores are linked with each other. Pores can also be classified as cylindrical, slit-shaped, cone-shaped and ink-bottle-like(**Fig. 1.1(b))**.[14]

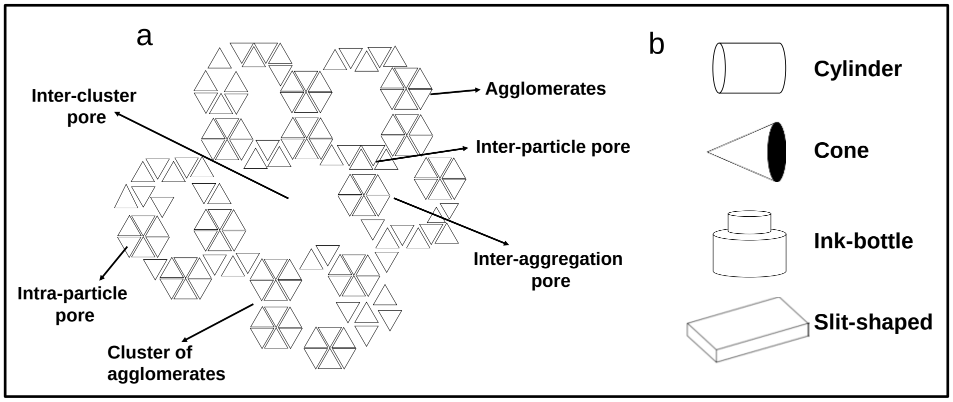

Fig. 1.1. Structural elements and types of pores.[14]

Pores usually have uneven surfaces with some of them making dead ends and moreover the pore structure evolves in the course of reaction, which notably affects the transport manner. Pore networking models have been reported to understand and analyze the transport behavior in addition for studying 2D and 3D pore networks.[15,16] In a pore networking model, the pore space is exemplified as a network of pore bodies that are connected via narrower channels. The pore bodies are corresponding to locally superior volumes while the channels relate to the throats, viz., the narrower passageways, also known as the constrictions among the pore bodies.[16]

1.3 Hierarchical porous materials

Constructing a porous hierarchy of materials across distinct lengths mimics natural set-ups and it gives rise to a range of functionalities required for a plethora of applications. The hierarchical porous materials combine different porosity scales and have multidimensional domains at different levels or multimodal pore structures.[17] The well-defined multimodal materials have importance in elucidating the central characteristics of sorption theory, namely diffusion and hysteresis.[18] The microporous or mesoporous materials face the drawback of limited mass transfer besides substandard access to the active sites.[19] Introducing micro as well as mesoporosity into a macroporous solid helps provide precise size and shape selectivities for active catalytic sites for guest molecules. However, the presence of macroporous networks can abate diffusion barriers.[20] Hierarchical porosity, thereby, facilitates the heat and mass transfer which eventually improves the availability of active sites and the selectivity of reaction in addition to restraining the incidence of secondary reactions.[21] Hierarchical porous structures enable high surface area accrediting to large pores along with minimizing the pressure drop.[22,23] These materials have been extensively explored as support materials and sorbents.

1.4 Monolithic materials

Monolith is a geological feature that comprises of a single gigantic stone for e.g., a single large piece of rock.[24] Monoliths are illustrations of structured supports and are distinguished by elongated parallel channels segregated through thin walls.[18] In view of industrial applications, monolithic materials are of paramount importance in the domain of surface-based applications like adsorption and catalysis.

1.4.1 Need of monolithic materials

Monolithic structures have gained attention mainly because most catalysts exist as powder, pellets, or granules. These catalysts have high pressure drop and there is a high chance of loss of catalyst during washing. The powder form is likely to undergo agglomeration and require sophisticated instruments and intricate operations to recycle the material.[25] The lost powders may in fact, also give rise to secondary pollution and eventually pass into living beings exhibiting toxic impact.[26] The immobilization of the powdered nanomaterials on a support material like film or ceramic foam can be done. Still, they reportedly have poor activity because of the reduced number of active sites and lesser surface area.[27] The structurally designed monolithic catalysts have emerged as an outstanding alternative to the powdered catalysts demonstrating multimodal porosity.[18,28]

1.4.2 Historical background

The discovery of mesoporous silica-based material was done by two research groups in Japan and the United States during early 90s. These groups successfully fabricated the new material through two distinct pathways but with a common silica source and surfactant as structure directing as well as agents and self-assembling agents for silica.[29] The synthesis of silica was done in alkaline media using a low concentration of surfactant and consequently, the formation of hexagonal silica mesophase occurred. Structure directing agents such as amphiphilic polymer, surfactant molecules, along with various experimental conditions, were finally established as parameters responsible for controlling pore size besides the geometry of silica monoliths.[29,30]

1.4.3 Properties of monolithic materials

Monoliths are fundamentally uniform blocks that comprise parallel channels that can be extruded into desirable shapes and sizes. It is also possible to extrude the monoliths from diverse materials like zeolites and carbon. A variety of shapes and sizes of monolithic structures can be constructed. Fabrication of different shapes like circular, rod-like, triangular or hexagonal is possible.[31] Conventionally, monolithic catalysts are usually fabricated through different methods, namely impregnation method, coating method, and spraying method. The monolithic carrier is the fundamental framework of the monolithic material that consists of a large number of channels along with the inner pores. These channels and pores are responsible for better mass and heat transfer, improved thermal as well as mechanical stability, high gas throughput and most importantly lower pressure drop.[26] The heat and mass transfer and ultimately the catalytic performance are impacted by the geometry of the monolithic channels.[31]

In contrast to materials in the form of pellets, monolithic materials have a large open frontal area, resulting in only slight resistance to flow via the monolithic channels. This attribute makes reaching high space velocities possible which is beneficial for fine tuning the selectivities of reaction and yields to products.[32] The uniform network of macropores in the monolithic structure is responsible for an equivalent and uniform admittance of the molecules to the active sites situated in the mesopores. This aspect is advantageous for upgraded adsorptive or catalytic reactions in liquid media employing monolithic microreactors. Through this type of a microreactor, it is possible to control the contact time of the reaction precisely and it further opens the paths to the enhancement of various reactions.[21] Thereby, these materials combine the nanoscale characteristics with a few centimeters total monolithic size. The penetration depth of radiation into macroscopic body of the monolith is pivotal because if the illumination of a large volume fraction of the photocatalytic material cannot be done, the performance is reduced.[33] The monolithic photoreactors comprise of considerable channels where coating of catalyst can be done along the channel walls which enhances the exposed surface area of catalysts toward light illumination. When the length of monolith increases, only a smaller portion of light can pass through the longer channels, where just the forepart of the monolith is proficiently illumined.[34]

1.4.4 Fabrication techniques

Metal-oxide/ sulfide monoliths have generally been produced via a plethora of synthesis routes and have been used for different purposes, as tabulated in **Table 1.1**. The metal-oxide/sulfide monoliths can be fabricated using the wet impregnation technique using SiO_2 monoliths as a support material. SiO_2 monoliths have an amorphous character and are generally synthesized through a sol-gel process and comprise multimodal and stratified pore structures.

Table 1.1. Literature survey showing different monolithic materials used for various applications.

Material	Synthesis method	Application	Year of research	Ref.
Nanostructure Anatase TiO_2 Monoliths	Sol-gel method with a peptization process	Photodegradation of Rhodamine B	2005	[35]
Co_3O_4, SnO_2, MnO_2 and Mn_2O_3 monoliths	Nanocasting	-	2006	[28]
Carbon monoliths	CVD	Hydrogen Storage	2007	[36]
Anatase TiO_2 monoliths	Polymer gel templating	Adsorption and photocatalysis	2009	[37]
α-Fe_2O_3, ZrO_2, Ni, Ag, and silver silicate	Nanocasting method	-	2012	[38]
N-modified TiO_2 monoliths	Polymer gel templating	Photodegradation of MB	2016	[39]

MnO_2 and TiO_2 monoliths	Nanocasting Method	Adsorption Pb(II) & Cd(II)	2017	40
Fe_2O_3 and Fe_2O_3/SiO_2 monoliths	Nanocasting Method	Adsorption of heavy metals and photodegradation	2018	41
Manganese-cobalt oxide core-shell nanoarray based monolithic catalysts	Microwave-assisted synthesis	Low temperature CO oxidation	2019	42
Bi-Metal-supported activated carbon monolith	Impregnation method	Selective hydrogenation of furfural	2020	43
Porous non-heirarchical CeO_2/SiO_2 monoliths	Sol-gel method	Photodegradation of dyes	2020	44
Carbon composite green monolith	Chemical method	Supercapacitor	2020	45
Fibrous polymer monoliths	Macromolecular synthesis	Photodegradation of dyes	2021	46
Hollow Co_3O_4 nanoparticles immobilized rGO/ carbon monolith	One-step carbonization method	Supercapacitor	2021	47

1.4.4.1 Sol-gel method

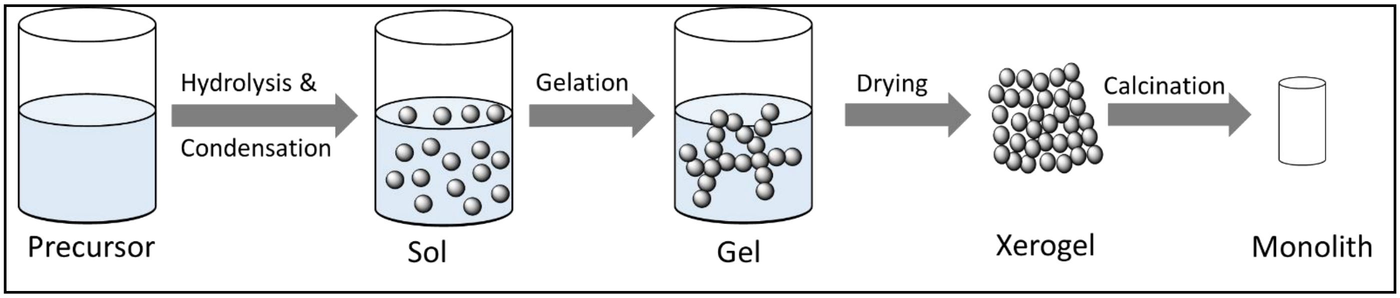

Fig. 1.2. Schematic illustration of a sol-gel method.

Sol-gel method for fabricating SiO_2 monoliths was firstly brought to notice by Nakanishi and Soga.[48] It is a wet chemical process where a 'sol' is first prepared from a precursor solution (usually a metal alkoxide) which is then kept for aging. Subsequent drying is done to form a network like 'gel' structure, as displayed in **Fig. 1.2**. Sol is a colloidal suspension, while gel is 3-D interconnecting network that is created between phases. The chemistry of the sol-gel technique includes condensation and polymerization reactions.[49,50]

1.4.4.2 Wet impregnation method

For the preparation of metal oxide/sulfide monolith using the SiO_2 monolith as template support, wet impregnation method is followed. Wet impregnation method for preparing monoliths using silica monoliths as support is depicted in **Fig. 1.3.** A template is usually a 'hard' object that doesn't change its shape substantially when the formation solid counterpart occurs.[50] The SiO_2 monolith is dipped in an excess solution of precursor metal salt and later, the solid is separated and the solvent removal is done via drying. This helps in the fabrication of composite monolithic material. This technique is advantageous as loading active matter on the surface of the material as the solution transport changes from a capillary action process to a diffusion process.[51]

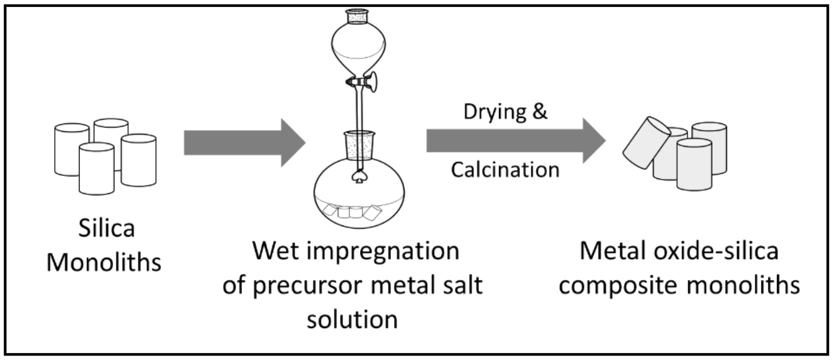

Fig. 1.3. Schematic illustration of wet impregnation method for preparing monoliths using silica monoliths as support.

1.4.4.3 Incipient wetness impregnation method

In this technique, an aqueous solution of inorganic salt in a suitable concentration is impregnated onto the support in a volume equal to or a little lesser as compared to the pore volume of the support (SiO_2). After the successful impregnation, the material is dried and calcined to achieve the final catalyst. This method is also called as dry impregnation since the impregnated material has a dry nature at a macroscopic scale.[52]

1.4.5 Impact of reaction conditions

The heating step where the exclusion of solvent occurs has a paramount importance as it determines the final structure besides the mechanical stability of the final monoliths.[28] At the end of the impregnation step, the pore volume of the monolith is occupied with the precursor solution. There is a distribution of the impregnant between the adsorbed phase on the pore wall as well as the liquid phase in the pore volume. The impregnation step is followed by drying which brings about transferal plus the evaporation of the solution, and ultimately the redistribution of the residual impregnant in the pore volume.[53] If the drying temperatures are too low then in the inner side of the pores, big crystals of the metal salt would be formed ultimately giving rise to macroscopic cracks in the monolithic framework. Contrarily, if very high drying temperatures are used then the diffusion of salt molecules from the center of the monolithic catalyst occurs many times resulting in hollow replicas. Thereby, the temperature may need to be regulated subject to the kind of metal salt used in the process for their successful decomposition. Moreover, if longer treatment time is employed then low temperatures are required for the nucleation progression as well as for the growth of the oxide phase.[28]

1.5 Water pollution

The world is progressing with a high-speed and therefore an evident change can be seen in everything in the recent years. The way man used to lead life some decades ago has been completely transformed. The industrial revolution over time has remarkably affected society. To name a few, textile, food, agrochemical, pharmaceutical and paper industries ultimately play an important role in daily life. However, over the years, the change in the world has not just been positive and constructive. The considerably negative facets are also very noticeable, such as ecological and health hazards. Consequently, the rising energy demand, as well as growing environmental pollution, are the primary challenges that the modern world is striving to deal with.[54]

Dyes are natural or man-made colored compounds having wide application as pH indicators, in textile, food, paper, leather industry, cosmetics, dye-sensitized solar cells, UV protective clothing, etc.[55] The colored waste from textile industries contains dyes that are natural or synthetic compounds. Synthetic dyes such as phthalocyanine, anthraquinone, azo dyes in addition to heterocyclic dyes are majorly utilized in industries. Around 60–70% of textile dyes are azo dyes specifically. The reactive dyes are captivated to the least extent by the cloth in the course of the dyeing process, which indicates that the residual amount of dye is lost directly into the wastewater. These bright and intensely colored dyes are water-soluble and very difficult to eradicate. Around 45,000 tons of organic dye is produced annually, while more than 11% of it is discharged into water resources.[56] The textile industry contributes to water pollution to the maximum extent globally. The textile discharge is highly colored, having high pH, BOD, and COD. The entrance of dye pollutants into natural water bodies depreciates the aquatic environment and ultimately has adverse effects on human health along with aquatic life. It is because textile dyes also act as carcinogenic and mutagenic agents and are responsible for mitotic poisoning. Exposure to dyes may lead to nausea, skin allergies, nasal burning and itching, gastrointestinal disorders, eye allergies, respiratory and renal failure and neuro as well as reproductive toxicity.[57]

Agrochemical compounds including pesticides and fertilizers find huge agricultural applications for increasing production.[58] A number of pesticides are frequently sensed in actual wastewater streams. It is reported that many pesticides are found in municipal wastewaters in a concentration range of 1-1000 ng/mL.[59] The careless and excessive use of agrochemicals in order to procure high crop besides improper management aggravates the problem.[60] Agrochemicals are also relatively slow to degrade.[58] The presence of pesticides in water bodies is hazardous for human health causing grievous problems like carcinogenicity, mutagenicity, neurotoxicity, cytotoxicity, genotoxicity, neurological disorders, endocrine disruption and reproductive problems.[61,62] Exposure to pesticides may lead to several chronic diseases viz., diabetes, aging, Parkinson, Alzheimer, cardiovascular and chronic kidney disease.[63] Almost 300,000 deaths occur every year accrediting pesticide poisoning.[64]

Pharmaceutical and personal care products are known as emerging contaminants and potential threats to the environment. Non-steroidal anti-inflammatory drugs, antibiotics, antiepileptic drugs, antidepressants are pharmaceutical drugs that could be problematic for the environment and require attention. The inapt dumping of medicines and drugs by manufacturer industries, hospitals, clinics, pharmacies, and households is the source of water contamination by pharmaceuticals.[65] The excreted traces or metabolites from pharmaceuticals get mixed with water bodies either directly or indirectly post ineffective treatment. The pharmaceuticals are found in effluents from wastewater treatment plants and surface waters in concentration range from ng L^{-1} to μg L^{-1}. The concentrations of pharmaceuticals residues in surface waters are relatively low.[66] In addition, every substance has a different mechanism of action, which makes detection, analysis, and removal quite an intricate process. Moreover, their occurrence, as well as persistence in surface waters, is harmful. The perpetual release of drug molecules and prolonged exposure poses lasting effects on aquatic biota for instance, rise in mortality rate, changes in traits, impact on reproductive health, etc.[67] Ingesting phenolic substances at lower concentrations could still cause troubles like impaired vision, irritation in eyes, skin in addition to diarrhea.[68]

Therefore, it is imperative to keep a tab on these hazardous and possibly lethal pollutants in the water bodies and properly treat industrial effluents. The severe damage that these pollutants cause to the environment and acute health issues is essentially a challenge that requires significant attention, sincere efforts, and severe action.

1.6 Techniques for wastewater treatment

Different methodologies have been used over the years to eradicate noxious pollutants from water. These include biological processes (aerobic, anoxic or anaerobic oxidation methods),[69] physical (magnetic, ultrasonic, electrochemical),[70] mechanical methods (filtration, sedimentation),[71] chemical (ozonation, oxidation, precipitation),[72] and physicochemical methods (coagulation, flocculation, adsorption, reverse osmosis, ion exchange).[69] However, these methods have certain disadvantages. Biological process is economically appealing but is slow, not easily controllable and moreover the variations in composition as well as volumes. Chemical methods are rapid and don't produce any sludge but require harsh chemicals and efficiency is dependent on the type of oxidant. Physicochemical methods are simpler and economical however physicochemical observing of the discharge (pH) is needed and moreover there is low removal of arsenic.[69] The said methods could also transform organic compounds to a new form and create secondary pollution. Moreover, their operation is pretty slow, needs control of temperature/pressure, and is uneconomical.[73] Nevertheless, photocatalytic degradation is one method that comes across as the most efficacious method as it promises complete mineralization of the pollutant and can utilize natural sunlight.[74]

1.7 Photocatalytic degradation

It is a type of advanced oxidation process for the eradication of water as well as air pollutants. As already discussed, complete mineralization of the pollutant can be attained using solar light through this technique. Moreover, it is economical, having no waste disposal issues, apart from requiring only mild temperature and pressure control.[75] The principle and mechanism of photocatalysis are elaborated in this section.

1.7.1 Principles of photocatalysis

Generally, heterogeneous photocatalysis using semiconductor materials utilizes light to generate different active species. Similar to any catalytic reaction, the photocatalytic reaction also has several steps. Firstly, the reactant molecules get transferred from the solution to the surface of the catalyst and gets adsorbed. Then, the photocatalytic reaction takes place in the adsorbed state. Subsequently, the degraded products of the target pollutant get desorbed and finally get removed from the interfacial part.[76] The photons strike on the surface of photocatalyst resulting in the generation of electron-hole pair as electrons (e^-) in valence (VB) get excited to conduction band (CB) leaving a positively photogenerated hole (h^+) **(Eq. 1.1)**. These e^- and h^+ participate in different redox reactions and facilitate pollutant degradation. However, only the photons with energies higher than the band gap energy (E_g) of the semiconductor can cause the excitation of e^- in VB. The absorption of photons having lower energy than E_g generally causes dissipation of energy in the form of heat. The attributes required by any material to be labelled as an ideal photocatalysts have been discussed in the past.[17,75]

$$\text{Photocatalyst} + h\nu \rightarrow e^- \ (\text{CB}) + h^+ \ (\text{VB}) \qquad (1.1)$$

1.7.2 Photocatalyst

Photocatalyst is a solid material that promotes the reaction rate in the presence of light and does not get used up in the reaction. The efficiency of photocatalysis depends on the electronic band structures and catalyst morphology apart from crystallinity and surface properties.[77] The reduction and oxidation potential of the desirable reaction must lie between the VB and CB potentials of the photocatalyst.[17] Highly crystalline structure with crystal defects has the probability of minimalizing the interface e^-/h^+ pair recombination, which improves the efficacy of charge separation and thus leads to efficacious reaction.[78] Moreover, the surface morphology like geometry and shape of the materials and surface properties like specific surface area, pore volume, and pore size of the photocatalysts also significantly impact photocatalytic performance because these factors influence the adsorption. Better adsorption leads to better photocatalytic activity.[79] Therefore, it can be summarized that an ideal photocatalyst must possess (a) good light harvesting properties, (b) narrow band gap, (c) competent charge separation, migration and transportation, (d) lower recombination rate of the photo-generated e^-/h^+, (e) high surface area, and (f) optimum VB and CB potentials.[17,75]

Reactive species like h^+, superoxide radicals ($O_2^{\bullet-}$), and hydroxyl radicals ($^{\bullet}OH$) are the major participants the redox reactions by e^-/h^+ pairs. The photo-oxidation of H_2O and OH^- by holes in the aqueous conditions generates $^{\bullet}OH$ radicals **(Eq. (1.2) - Eq. (1.3))**. The $O_2^{\bullet-}$ radical anions are produced by the reduction of e^- in CB **(Eq. 1.4)** and can also further react with H^+ producing $^{\bullet}OOH$ radicals **(Eq. 1.5)** decomposing to generate $^{\bullet}OH$ radicals **(Eq. (1.6))- (Eq. (1.8))**. These reactive species like $^{\bullet}OH$, $O_2^{\bullet-}$, h^+ react with the target pollutant and disintegrate it to form some degraded products **(Eq. 1.9)**. On the other hand, when the reduction of O_2 and the oxidation of pollutants don't occur concurrently, the electrons get amassed in the CB, leading to an increase in e−/h+ recombination, which decreases the photocatalytic efficiency process. Nonetheless, the presence of O_2 can avert the recombining of e^-/h^+ pair.[75,80] In the case of complete mineralization, CO_2 and H_2O are obtained as products.

$$H_2O + h^+ \rightarrow H_2O^+ \rightarrow {}^{\bullet}OH + H^+ \qquad (1.2)$$

$$^{-}OH + h^+ \rightarrow {}^{\bullet}OH \qquad (1.3)$$

$$O_2 + e^- \rightarrow {}^{-\bullet}O_2 \qquad (1.4)$$

$$^{-\bullet}O_2 + H^+ \rightarrow {}^{\bullet}OOH \qquad (1.5)$$

$$^{\bullet}O_2H + {}^{\bullet}O_2H \rightarrow H_2O_2 + 1/2O_2 \qquad (1.6)$$

$$H_2O_2 + {}^{-\bullet}O_2 \rightarrow {}^{\bullet}OH + {}^{-}OH + H_2O_2 \qquad (1.7)$$

$$H_2O_2 + h\nu \rightarrow 2{}^{\bullet}OH \qquad (1.8)$$

$$^{\bullet}OH/ {}^{-\bullet}O_2/ h^+ + \text{target pollutant} \rightarrow \text{degraded products} \qquad (1.9)$$

1.7.3 Classification of semiconductor photocatalysts

Semiconductor photocatalysts have been classified into three generations namely first, second, and third generation as elaborated in this section.

1.7.3.1 First generation photocatalyst

These photocatalysts are single component oxides/sulfides/nitrides having VB and CB pair parted by a band energy gap and are dependent on e−/h+ generation. When light is absorbed by the photocatalyst ($h\nu \geq Eg$) the e^- is excited from VB to CB and h^+ are formed in VB. The reaction of h^+ with ^-OH gives rise to $^\bullet OH$ whereas the reaction of O_2 with e^- in CB forms $O_2^{\bullet -}$. TiO_2 is a first generation photocatalyst has been examined extensively in this regard owing to its supreme photocatalytic activity in UV light illumination, inexpensive nature, non-toxicity, high stability, and accessibility. Other examples of first generation photocatalyst include ZnO, ZnS, SnO_2, MnO_2, ZrO_2, and Co_2O_3.[81] The drawback of first-generation photocatalysts is that these have a band gap >3 eV which hampers their ability to harvest solar energy for catalysis. Additionally, the solar spectrum constitutes only around 4-5% UV radiation required for exciting these materials which confines their practical applications.[81]

1.7.3.2 Second generation photocatalyst

To overcome the shortcomings of first generation photocatalyst, multi-component photocatalysts have been studied. It includes heterojunction-construction, loading a co-catalyst, and doping with metals/non-metals. Heterojunction materials are second generation multi-component photocatalysts that comprise of stacking up two first-generation photocatalysts having dissimilar bandgaps. The bandgap of resultant photocatalyst lies in the visible region and these are of two kinds: direct and indirect bandgap. For preparing the direct bandgap materials, the maximum energy level of VB aligns with lowermost energy level of CB. Thermodynamically, the driving force for a particular reaction is dependent on the difference between the thermodynamic potential of CB and VB and the reaction. In heterojunction photocatalysts, the photo-induced e^-s are restricted in the CB of one semiconductor whereas the h^+ are restrained in the VB of another semiconductor which enhances the e^-/h^+ separation thereby demonstrate boosted catalytic performance by suppressing the e^-/h^+ recombination. These materials have narrower band gaps in comparison to first-generation materials and thus absorb visible radiation ($\lambda \geq 420$ nm). However, the additional equipment and energy requisite for separation of these materials from suspension systems enhance the overall cost of treating industrial discharge besides causing the leaching of catalyst.[81,82]

1.7.3.3 Third generation photocatalyst

The third generation photocatalytic materials consist of metallic nanocrystals, metal oxides, carbon/boron nitrides, etc., deposited on various substrates. Two methodologies utilized for immobilizing are the binder-through and binder-less methods. However, the deposition by means of binders causes reduction in surface area in addition to the active sites for photooxidation of contaminants. Examples of third generation photocatalyst include steel/TiO_2-WO_3, Si/TiO_2, Glass/P-TiO_2, etc. However, the bottleneck in this case is that depositing multi-component heterojunction materials on substrates is difficult as it needs multi-step synthesis methodology.[81,82]

1.7.4 Heterojunction photocatalysts

This section carries out an elaborative discussion on heterojunction photocatalysts which are usually described as the interface between two dissimilar semiconductors having differing band structures resulting in band alignments.

1.7.4.1 Type I heterojunction photocatalyst

These heterojunctions have a straddling band gap and the VB of first semiconductor is lower than the VB of second semiconductor while the CB is higher than the CB of second semiconductor. In this case, the accumulation of e^- and h^+ occurs on one semiconductor and thus there is no effective separation of e^- and h^+ **(Fig. 1.4(a))**. Additionally, the redox capability of the overall photocatalyst is reduced since the redox reaction occurs on the material that has lower redox potential.[83]

1.7.4.2 Type II heterojunction photocatalyst

These heterojunctions have a staggered band gap and the VB ad CB of first semiconductor lie at higher level in comparison to second semiconductor. In this case, the e^- get migrated from semiconductor A to B, whereas the holes will transfer from semiconductor B to A which causes a spatial separation of e^-/h^+ pairs **(Fig. 1.4(b))**. The photoreduction reaction occurs on B having lower reduction potential while the photooxidation reaction occurs on A having higher oxidation potential.[84]

1.7.4.3 Type III heterojunction photocatalyst

These heterojunctions also have a staggered band gap just that it gets so extreme that there is overlapping of bandgaps. Consequently, the e^-/h^+ migration and segregation can’t take place in type III heterojunction making it unsuitable for achieving augmented photoactivity.[83]

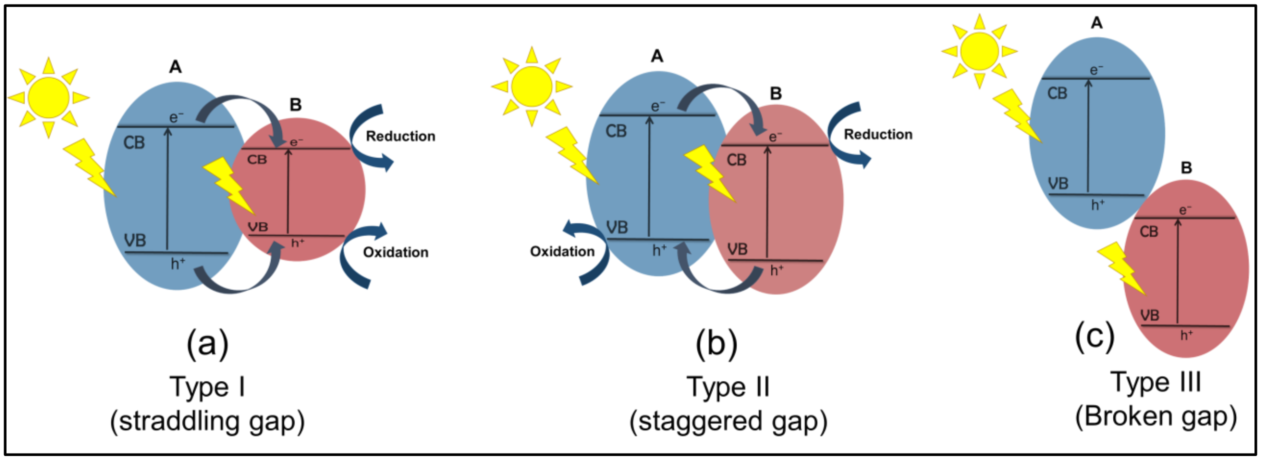

Fig. 1.4. Schematic illustration of various heterojunction systems.

1.7.4.4 Z-scheme heterojunction photocatalyst

In order to overcome the shortcoming of compromised redox capacity of the photocatalyst, Z-scheme heterojunctions are formed for maximizing the redox potential of overall heterojunction systems.[83,85]

1.7.4.4.1 First generation Z-scheme heterojunction

This system consists of two dissimilar semiconductors, I and II along with a shuttle redox mediator (acceptor/donor (A/D) pair) and as the reaction proceeds, photogenerated e^- get transferred from the CB of semiconductor II to the VB of the semiconductor I via the acceptor/donor pair as descried in redox reactions in Eq. (1.10)- Eq. (1.11) and **Fig. 1.5(a)**.

$$A + e^- \text{ (@CB of semiconductor II)} \rightarrow D \qquad (1.10)$$

$$D + h^+ \text{ (@VB of semiconductor I)} \rightarrow A \qquad (1.11)$$

In this way, the h^+ stay on semiconductor II (greater oxidation potential) whereas the e^- stay on semiconductor I (greater reduction potential), thus attaining the optimized redox potential of the overall photocatalytic system. However, the occurrence of backward reaction ascribing to the usage of reversible redox mediators is a serious bottleneck of these heterojunctions. Moreover, this system functions well only in the liquid state which led to the discovery of second generation Z-scheme heterojunction.

1.7.4.4.2 Second generation Z-scheme heterojunction

The all-solid-state or second generation Z-scheme heterojunction system comprises of two distinct semiconductors along with an e^- mediator, usually a noble-metal nanoparticle (e.g., Au, Ag, Pt) as exhibited in **Fig. 1.5(b)**. This way, the backward reaction of 1st generation Z-scheme heterojunction in restrained. But, the employment of noble metals is not cost-effective thus limiting the application of this system.

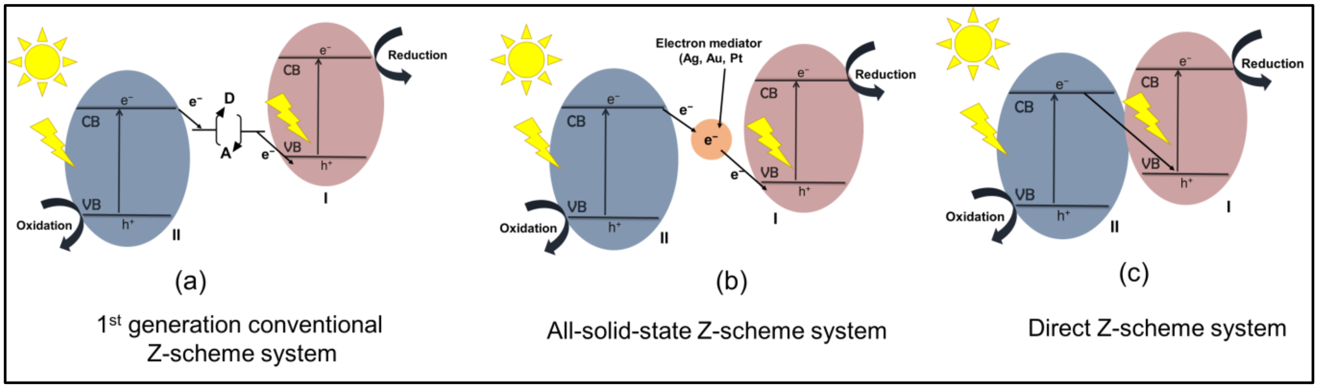

(a)
1st generation conventional
Z-scheme system

(b)
All-solid-state Z-scheme system

(c)
Direct Z-scheme system

Fig. 1.5. Schematic illustration of Z-scheme heterojunction systems.

1.7.4.4.3 Direct Z-scheme heterojunction photocatalyst

This system comprises of only two semiconductors having direct contact at their interface and doesn't require any e^- mediator (**Fig. 1.5(c)**). The light-shielding effect due to the doping of the metal-based mediator can also be dealt with by this heterojunction. In comparison to type-II heterojunction, the charge transfer on this direct Z-scheme system is favored more owing to the electrostatic attraction between e^- and h^+. However, may doubts have been posed regarding the direct Z-scheme heterojunction systems such as fermi level adjustment, concept of establishment of built-in electric field, e^- transport channel, and band bending. In case of same Fermi levels, there is disappearance of the potential difference ad consequently the built-in electric field can't be established.[86] These scientific concerns led to the development of step-scheme heterojunction photocatalytic system (S-scheme).

1.7.4.5 S-scheme heterojunction photocatalyst

This system consists of oxidation (O) and reduction (R) photocatalysts and when these come in contact, the e^-s at the interface drift from R (having higher Fermi level) to O (having lower Fermi level) as exhibited in **Fig. 1.6(a)**. Therefore, there is a loss of e^-s at R side making it positively charged while the O side becomes negatively charged on the acceptance of e^-s. In addition, the upward or downward band bending takes place at the interface of R and O photocatalyst. Simultaneously, a built-in electric field is generated pointing from R to O which directs the photogenerated e^-s CB of O to VB of R under illumination of light. Furthermore, the Coulombic attraction amongst h^+ in R and e^-s in O besides band bending also facilitates the charge transfer while the Coulombic repulsion and built-in electric field besides band bending hinders the transferring of e^- from CB of R to CB of O (the transferring of h^+ from VB of O to VB of R). Finally, the potent photogenerated e^-s are conserved in the CB of R plus h^+s are preserved in the VB of O, whereas the weak charge carriers undergo recombination. As a result, strong redox capability is present in the S-scheme heterojunction as it jointly accomplishes charge segregation and strong photo-redox capability, leading to augmented photocatalytic performance.[87,88]

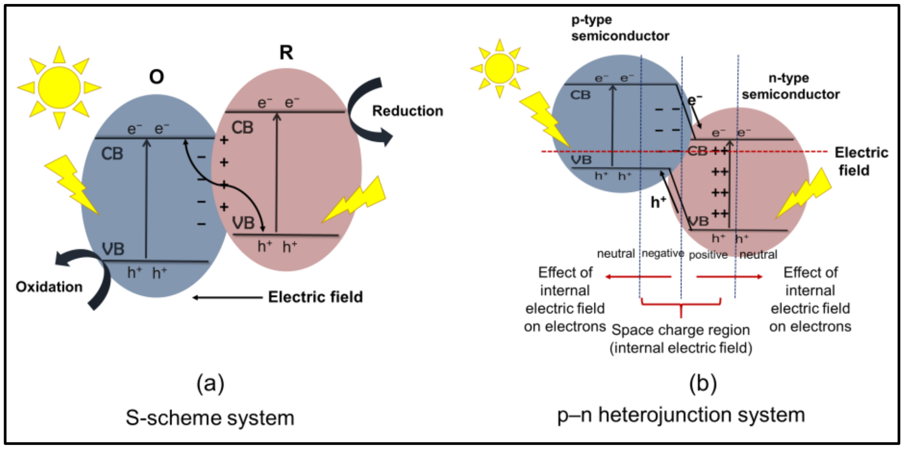

(a)
S-scheme system

(b)
p–n heterojunction system

Fig. 1.6. Schematic illustration of S-scheme and p–n heterojunction systems.

1.7.4.6 p–n heterojunction photocatalyst

The p–n heterojunction photocatalyst system is developed by the combination of n and p-type semiconductors. Prior to the light illumination, the e^{-}s on the n-type semiconductor close to the p–n interface are likely to get diffused into the p-type material, thereby leaving behind positively charged species. Whereas, the h^{+}s on the p-type semiconductor close to the interface are likely to get diffused toward the n-type semiconductor, leaving behind a negatively charged species. The e^{-}/h^{+} diffusion lasts until the establishment of Fermi level equilibrium of the system. Consequently, the area in the vicinity of p–n interface is charged, hence generating a "charged" space or internal electric field. After the light illumination, both p and n-type semiconductors can be excited, producing e^{-}/h^{+} pairs which move under the effect of internal electric field to the VB of p-type and CB of the n-type semiconductor, respectively resulting in spatial separation of the e^{-}/h^{+} pairs which is thermodynamically feasible since both the CB and VB of the p-type material are usually situated higher as compared to the n-type material in a p–n heterojunction (**Fig. 1.6(b))**. Consequently, the e^{-}/h^{+} separation efficacy in this case is quicker in comparison to type-II heterojunction ascribing to the synergy amongst band alignment and internal electric field.[83,89]

Numerous new photocatalysts are being designed lately and substantial attention is garnered by novel visible light driven photocatalysts for achieving superior photocatalytic efficiencies. **Table 1.2** summarizes various literature reports discussing the use of diverse photocatalysts for photocatalytic degradation.

Table 1.2. Various photocatalysts for photocatalytic degradation of diverse organic pollutants.

Catalyst	Pollutant	Catalyst Conc. (g/L)	Time (min)	Light source	% degradation	First order rate constant (min^{-1})	Ref.
$BiVO_4$/EDTA	MB (5 ppm)	1	300	Stimulated sunlight (500 W Xe arc lamp)	90.8	0.0078	90
TiO_2/Polyaniline	MB (10 ppm)	2.5	200	UV light	73	0.0068	91

MoS_2	MB (10 ppm)	0.3	180	Visible light (500 W Xe lamp)	73.83	0.0066	92
CuO nanoparticles	Rh-B (100 µM)	1	150	Visible light (fluorescent lamp)	83	-	93
g-C_3N_4/MoO_3	Rh-B (10 ppm)	0.3	120	Visible light (250 W Xe lamp)	71.86	-	94
ZnO/CuO composite on Cu foam	Rh-B (5 ppm)	-	120	Visible light (300 W Xe lamp)	63.8	0.0078	95
SnO_2 quantum dots	TM (50 ppm)	0.1	45	Solar light	57	-	96
Sulfate doped-Ag_3PO_4	TM (5 ppm)	0.8	60	Visible light (six 4 W fluorescent lamps)	39.94	0.0080	97
CuO powder	TM (5 ppm)	1	60	Visible light (72 W LED lamp)	48.65	0.0109	98
Phosphorus-doped g-C_3N_4 /Co_3O_4 quantum dots	MZ (10 ppm)	1	180	Visible light (250 W Xe lamp)	68.9	0.0064	99
$CuBi_2O_4$/CuO	MZ (50 ppm)	1	120	Simulated solar light (150 W Xe lamp)	36	-	100
$CoFe_2O_4$@methylcellulose	MZ (5 ppm)	0.67	120	UV light (6 W low-pressure lamp)	85.3	0.0087	101

1.8. Importance of photoreactor design

Optimizing the photoreactor configuration is a crucial factor affecting the rate of pollutant degradation and superior design of reactors is vital for large-scale application. The characterization of photoreactors is based on numerous factors: type of photocatalyst, geometrical shape, and fluid dynamics.[106] The optimization of photocatalytic reactors can be done by tackling technical and chemical characteristics. The main factors include the model simplicity, the capacity to function under a broad collection of liquid flow rates, and efficacious irradiation system (uniform photon distribution on the surface of photocatalyst). The mass transfer as well as reaction kinetic data coming from experimentations can be jointly utilized with computational fluid dynamic methods for optimizing photoreactors set-up parameters such as the reactor room geometry, flow rate, duration of illumination, etc.). The scaling up of a photoreactor entails developing a mathematical model which is the enclosure of various sub-models such as the kinetic model, radiation emission model, fluid-dynamic model, and radiation absorption-scattering model.[106]

The geometry of the photoreactor relies on the dimensions as well as the shape of the light source and it should be picked in a way for maximizing the light harvesting. Photoirradiation can be done externally (lamp outside the reactor) or internally (lamps immersed in the liquid). The external illumination is carried out by using one or added lamps. Various photocatalytic reactor configurations include annular packed bed photoreactor, falling film reactor, flat-plate photocatalytic reactor, parallel plate disk photoreactor, continuous flow fixed bed reactor.[107] An unsuitable photoreactor design might lead to a substantial surge of the energy intake, non- uniform photon distribution, inapt flow rate, or catalyst deactivation directly affecting on the photocatalytic performance.[106]

The studies describing the influence of distance of the reactor from the light sources and intensities on the kinetic rates are limited. As the effectiveness of UV-LEDs is lesser as compared to mercury lamps, their pairing with a more effective reactor is imperative. The most convincing characteristics of LEDs include the ability of variation of pattern the LED radiation with respect to packaging material. The determination of the emitted light is done by intrinsic parameters viz., wavelength of light source, optical features of the reflecting cup, and LED chip face roughness, apart from the radius of the encapsulating lens. The gap between the lamp and the photocatalyst surface impacts the intensity of the incident radiation along with the catalyst area dissemination. Smaller distances not only enhance the radiation intensity but also reduce the homogeneousness.[108]

1.9 Quantum efficiency

Quantum efficiency is of paramount importance for quantitatively evaluating the functional properties of photocatalytic materials. It undertakes the information of the number of photons of a certain wavelength absorbed by the photocatalytic system. As per IUPAC, evaluating the quantum efficiency necessitates: (a) measurement of the reaction rate in differential and transfer free settings (b) radiation source reaching steady-state establishment; and (iii) adequately ascertained incident radiation flux.[102] The apparent quantum efficiency is usually calculated using Eq. (1.12).[103]

$$\text{Quantum efficiency (\%)} = \frac{\text{Mols of reacted electrons per unit time (mol/s)}}{\text{Mols of incident photons per unit time (Eins/s)}} \times 100 \qquad (1.12)$$

1.10 Loopholes in photocatalytic degradation

1.10.1 Direct photo-oxidation of dyes

The photocatalytic degradation of dyes can proceed via two pathways: (a) direct mechanism and (b) indirect mechanism. In the direct mechanism for photodegradation, dye molecules absorb visible light and get excited from the ground state to an excited state (dye^*). The excited dye molecule can then inject electron to the conduction band of photocatalyst after which the excited state dye species is converted to a radical cation ($\text{dye}^{\bullet+}$). The reaction between electrons and O_2 lead to the formation of superoxide anion radicals ($O_2^{\bullet-}$) which on reaction with H^+ (present in the aqueous solution) generates $^{\bullet}OOH$ and ultimately converts to H_2O_2 which in turn forms $^{\bullet}OH$ radicals. These free radicals are accountable for the photodegradation of dyes. However, this mechanism is reported to be very slow, less common and overshadowed by indirect mechanism.[104]

1.10.2 Other problems

Excessive amounts of money is required in the macroscale production of many photocatalytic materials for wastewater treatment owing to the involvement of disproportionate cost and detailed stages. Thus, developing low-cost semiconductor photocatalysts through simple steps is crucial. Additionally, the photoreactor design has paramount importance for effective photocatalytic degradation. The spreading of the light energy properly also has an impact on the rate of degradation.

However, the complete mineralization of organic pollutants to CO_2 and water is rarely demonstrated. There is a likelihood for the production of small molecules additionally viz. acetic acid, formic acid, etc. These are usually relatively less noxious than target pollutant which rules out the chances of direct threat. However, in some cases the degraded products could be more toxic than the parent molecule.[105] Also, there are only a few studies reporting the analysis of the liquid/gas phase degraded products Moreover, the comparison of a photocatalytic system for a particular pollutant degradation is difficult because of difference in light intensities, light penetration, different sampling methods, and varied catalyst: pollutant ratios.

1.11 Research Gaps

As already discussed in section 1.4.1, most of the photocatalysts reported in the literature exist in powdered form, having drawbacks like the generation of a miscible suspension with water which makes the reuse of the photocatalyst quite a tedious task. Moreover, sophisticated instruments and filters are required for the separation of powdered catalysts after the reaction. Monolithic catalysts come to the rescue in such situations as they can be easily separated after the photocatalytic reaction.[25,109] Moreover, these hierarchical photocatalysts have higher surface area and increased number of active sites which speed up the reaction kinetics on surface along with greater light uptake and transport kinetics.

Therefore, based on a comprehensive literature review, we observed the following research gaps which have been bridged and achieved in the present research study.

- Not much attention been paid on the synthesis of visible light active metal oxide monoliths for e.g., WO_3/SiO_2, Sb_2S_3/SiO_2 by simple wet impregnation method.

- The monoliths have mostly been used for adsorption purposes only. However, adsorption does not promise complete elimination of the pollutant from the environment.

- There is not much significant work done regarding employment of metal oxide/sulfide monolithic photocatalysts for the purpose of photocatalysis.

- The rare literature that is available on photocatalysis through monolithic materials discusses only the removal of dye pollutants, and no emphasis has been put on colorless recalcitrant contaminants like pesticides and pharmaceutical pollutants.

1.12 Objectives

The main motive of the present research work is to synthesize diverse monolithic photocatalysts for the effective removal of hazardous organic pollutants like dyes/pesticides/pharmaceutical compounds from their aqueous solution in light. The specific objectives are as follows:

1. Synthesis of visible light active, porous metal oxide/sulfide monoliths using silica monolith as a porous template.
2. Use of synthesized monoliths in photocatalytic degradation of organic pollutants (e.g., dyes/pesticides/VOCs) in visible/UV/sun light.

References

(1) Grieneisen, M. L.; Zhang, M. Nanoscience and Nanotechnology: Evolving Definitions and Growing Footprint on the Scientific Landscape. *Small* **2011**, *7* (20), 2836–2839. https://doi.org/10.1002/smll.201100387.

(2) Balzani, V. Nanoscience and Nanotechnology: A Personal View of a Chemist. *Small* **2005**, *1* (3), 278–283. https://doi.org/10.1002/smll.200400010.

(3) Culp, J. T. Flexible Solid Sorbents for CO_2 Capture and Separation. In *Novel Materials for Carbon Dioxide Mitigation Technology*; Elsevier, 2015; pp 149–176. https://doi.org/10.1016/B978-0-444-63259-3.00005-7.

(4) Gould, N. S.; Li, S.; Cho, H. J.; Landfield, H.; Caratzoulas, S.; Vlachos, D.; Bai, P.; Xu, B. Understanding Solvent Effects on Adsorption and Protonation in Porous Catalysts. *Nat. Commun.* **2020**, *11* (1), 1060. https://doi.org/10.1038/s41467-020-14860-6.

(5) Cui, W.; Hu, T. Incorporation of Active Metal Species in Crystalline Porous Materials for Highly Efficient Synergetic Catalysis. *Small* **2021**, *17* (22), 2003971. https://doi.org/10.1002/smll.202003971.

(6) Lin, X.; Wang, S.; Tu, W.; Wang, H.; Hou, Y.; Dai, W.; Xu, R. Magnetic Hollow Spheres Assembled from Graphene-Encapsulated Nickel Nanoparticles for Efficient Photocatalytic CO_2 Reduction. *ACS Appl. Energy Mater.* **2019**, *2* (10), 7670–7678. https://doi.org/10.1021/acsaem.9b01673.

(7) Noori, Y.; Akhbari, K. Post-Synthetic Ion-Exchange Process in Nanoporous Metal–Organic Frameworks; an Effective Way for Modulating Their Structures and Properties. *RSC Adv.* **2017**, *7* (4), 1782–1808. https://doi.org/10.1039/C6RA24958B.

(8) Rapti, S.; Sarma, D.; Diamantis, S. A.; Skliri, E.; Armatas, G. S.; Tsipis, A. C.; Hassan, Y. S.; Alkordi, M.; Malliakas, C. D.; Kanatzidis, M. G.; et al. All in One Porous Material: Exceptional Sorption and Selective Sensing of Hexavalent Chromium by Using a Zr^{4+} MOF. *J. Mater. Chem. A* **2017**, *5* (28), 14707–14719. https://doi.org/10.1039/C7TA04496H.

(9) Kang, W.; Zhang, Y.; Fan, L.; Zhang, L.; Dai, F.; Wang, R.; Sun, D. Metal–Organic Framework Derived Porous Hollow Co_3O_4 /N–C Polyhedron Composite with Excellent Energy Storage Capability. *ACS Appl. Mater. Interfaces* **2017**, *9* (12), 10602–10609. https://doi.org/10.1021/acsami.6b15000.

(10) Nakanishi, K. Pore Structure Control of Silica Gels Based on Phase Separation. *J. Porous Mater.* **1997**, *4* (2), 67–112. https://doi.org/10.1023/A:1009627216939.

(11) Savina, I. N.; Gun’ko, V. M.; Turov, V. V.; Dainiak, M.; Phillips, G. J.; Galaev, I. Y.; Mikhalovsky, S. V. Porous Structure and Water State in Cross-Linked Polymer and Protein Cryo-Hydrogels. *Soft Matter* **2011**, *7* (9), 4276. https://doi.org/10.1039/c0sm01304h.

(12) Huang, H.; Wang, L.; Cai, Y.; Zhou, C.; Yuan, Y.; Zhang, X.; Wan, H.; Guan, G. Facile Fabrication of Urchin-like Hollow Boehmite and Alumina Microspheres with a Hierarchical Structure via Triton X-100 Assisted Hydrothermal Synthesis. *CrystEngComm* **2015**, *17* (6), 1318–1325. https://doi.org/10.1039/C4CE02133A.

(13) Kaneko, K. Determination of Pore Size and Pore Size Distribution. *J. Memb. Sci.* **1994**, *96* (1–2), 59–89. https://doi.org/10.1016/0376-7388(94)00126-X.

(14) Zdravkov, B.; Čermák, J.; Šefara, M.; Janků, J. Pore Classification in the Characterization

of Porous Materials: A Perspective. *Open Chem.* **2007**, *5* (2), 385–395. https://doi.org/10.2478/s11532-007-0017-9.

(15) Xiong, Q.; Baychev, T. G.; Jivkov, A. P. Review of Pore Network Modelling of Porous Media: Experimental Characterisations, Network Constructions and Applications to Reactive Transport. *J. Contam. Hydrol.* **2016**, *192*, 101–117. https://doi.org/10.1016/j.jconhyd.2016.07.002.

(16) Maalal, O.; Prat, M.; Peinador, R.; Lasseux, D. Determination of the Throat Size Distribution of a Porous Medium as an Inverse Optimization Problem Combining Pore Network Modeling and Genetic and Hill Climbing Algorithms. *Phys. Rev. E* **2021**, *103* (2), 023303. https://doi.org/10.1103/PhysRevE.103.023303.

(17) Li, X.; Yu, J.; Jaroniec, M. Hierarchical Photocatalysts. *Chem. Soc. Rev.* **2016**, *45*, 2603–2636. https://doi.org/10.1039/c5cs00838g.

(18) Kuang, D.; Brezesinski, T.; Smarsly, B. Hierarchical Porous Silica Materials with a Trimodal Pore System Using Surfactant Templates. *J. Am. Chem. Soc.* **2004**, *126* (34), 10534–10535. https://doi.org/10.1021/ja0470618.

(19) Ren, Y.; Ma, Z.; Morris, R. E.; Liu, Z.; Jiao, F.; Dai, S.; Bruce, P. G. A Solid with a Hierarchical Tetramodal Micro-Meso-Macro Pore Size Distribution. *Nat. Commun.* **2013**, *4* (1), 2015. https://doi.org/10.1038/ncomms3015.

(20) Yang, X. Y.; Chen, L. H.; Li, Y.; Rooke, J. C.; Sanchez, C.; Su, B. L. Hierarchically Porous Materials: Synthesis Strategies and Structure Design. *Chem. Soc. Rev.* **2017**, *46* (2), 481–558. https://doi.org/10.1039/c6cs00829a.

(21) Galarneau, A.; Sachse, A.; Said, B.; Pelisson, C.-H.; Boscaro, P.; Brun, N.; Courtheoux, L.; Olivi-Tran, N.; Coasne, B.; Fajula, F. Hierarchical Porous Silica Monoliths: A Novel Class of Microreactors for Process Intensification in Catalysis and Adsorption. *Comptes Rendus Chim.* **2016**, *19* (1–2), 231–247. https://doi.org/10.1016/j.crci.2015.05.017.

(22) Smått, J. H.; Schunk, S.; Lindén, M. Versatile Double-Templating Synthesis Route to Silica Monoliths Exhibiting a Multimodal Hierarchical Porosity. *Chem. Mater.* **2003**, *15* (12), 2354–2361. https://doi.org/10.1021/cm0213422.

(23) Parlett, C. M. A.; Wilson, K.; Lee, A. F. Hierarchical Porous Materials: Catalytic Applications. *Chem. Soc. Rev.* **2013**, *42* (9), 3876–3893. https://doi.org/10.1039/C2CS35378D.

(24) Shenashen, M. A.; El-Safty, S. A.; Khairy, M. Trapping of Biological Macromolecules in the Three-Dimensional Mesocage Pore Cavities of Monolith Adsorbents. *J. Porous Mater.* **2013**, *20* (4), 679–692. https://doi.org/10.1007/s10934-012-9642-6.

(25) Zhou, C.; Lai, C.; Xu, P.; Zeng, G.; Huang, D.; Li, Z.; Zhang, C.; Cheng, M.; Hu, L.; Wan, J.; et al. Rational Design of Carbon-Doped Carbon Nitride/$Bi_{12}O_{17}Cl_2$ Composites: A Promising Candidate Photocatalyst for Boosting Visible-Light-Driven Photocatalytic Degradation of Tetracycline. *ACS Sustain. Chem. Eng.* **2018**, *6* (5), 6941–6949. https://doi.org/10.1021/acssuschemeng.8b00782.

(26) Wang, Z.; Zhao, K.; Xiao, B.; Gao, P.; He, D.; Cai, T.; Yuan, J. Fabrication of Monolithic Catalysts: Comparison of the Traditional and the Novel Green Methods. *Catalysts* **2019**, *9* (12), 1–14. https://doi.org/10.3390/catal9120981.

(27) Wan, W.; Zhang, R.; Ma, M.; Zhou, Y. Monolithic Aerogel Photocatalysts: A Review. *J. Mater. Chem. A* **2018**, *6* (3), 754–775. https://doi.org/10.1039/c7ta09227j.

(28) Smått, J. H.; Weidenthaler, C.; Rosenholm, J. B.; Lindén, M. Hierarchically Porous Metal Oxide Monoliths Prepared by the Nanocasting Route. *Chem. Mater.* **2006**, *18* (6), 1443–1450. https://doi.org/10.1021/cm051880p.

(29) Yanagisawa, T.; Shimizu, T.; Kuroda, K.; Kato, C. The Preparation of Alkyltrimethylammonium–Kanemite Complexes and Their Conversion to Microporous Materials. *Bull. Chem. Soc. Jpn.* **1990**, *63* (4), 988–992. https://doi.org/10.1246/bcsj.63.988.

(30) Nakanishi, K.; Takahashi, R.; Nagakane, T.; Kitayama, K.; Koheiya, N.; Shikata, H.; Soga, N. Formation of Hierarchical Pore Structure in Silica Gel. *J. Sol-Gel Sci. Technol.* **2000**, *17* (3), 191–210. https://doi.org/10.1023/A:1008707804908.

(31) Govender, S.; Friedrich, H. Monoliths: A Review of the Basics, Preparation Methods and Their Relevance to Oxidation. *Catalysts* **2017**, *7* (12), 62. https://doi.org/10.3390/catal7020062.

(32) Boger, T.; Heibel, A. K.; Sorensen, C. M. Monolithic Catalysts for the Chemical Industry. *Ind. Eng. Chem. Res.* **2004**, *43* (16), 4602–4611. https://doi.org/10.1021/ie030730q.

(33) Matter, F.; Niederberger, M. The Importance of the Macroscopic Geometry in Gas-Phase Photocatalysis. *Adv. Sci.* **2022**, *9* (13), 2105363. https://doi.org/10.1002/advs.202105363.

(34) Tahir, M.; Amin, N. S. Photocatalytic CO2 Reduction and Kinetic Study over In/TiO_2 Nanoparticles Supported Microchannel Monolith Photoreactor. *Appl. Catal. A Gen.* **2013**, *467*, 483–496. https://doi.org/10.1016/j.apcata.2013.07.056.

(35) Liu, Y.; Li, J.; Wang, M.; Li, Z.; Liu, H.; He, P.; Yang, X.; Li, J. Preparation and Properties of Nanostructure Anatase TiO_2 Monoliths Using 1-Butyl-3-Methylimidazolium Tetrafluoroborate Room-Temperature Ionic Liquids as Template Solvents. *Cryst. Growth Des.* **2005**, *5* (4), 1643–1649. https://doi.org/10.1021/cg050017z.

(36) Xia, Y.; Mokaya, R. Ordered Mesoporous Carbon Monoliths: CVD Nanocasting and Hydrogen Storage Properties. *J. Phys. Chem. C* **2007**, *111* (27), 10035–10039. https://doi.org/10.1021/jp071936y.

(37) Fan, X.; Fei, H.; Demaree, D. H.; Brennan, D. P.; St. John, J. M.; Oliver, S. R. J. Polymer Gel Templating of Free-Standing Inorganic Monoliths for Photocatalysis. *Langmuir* **2009**, *25* (10), 5835–5839. https://doi.org/10.1021/la8029837.

(38) Smått, J.-H.; Sayler, F. M.; Grano, A. J.; Bakker, M. G. Formation of Hierarchically Porous Metal Oxide and Metal Monoliths by Nanocasting into Silica Monoliths. *Adv. Eng. Mater.* **2012**, *14* (12), 1059–1073. https://doi.org/10.1002/adem.201100355.

(39) Nursam, N. M.; Wang, X.; Tan, J. Z. Y.; Caruso, R. A. Probing the Effects of Templating on the UV and Visible Light Photocatalytic Activity of Porous Nitrogen-Modified Titania Monoliths for Dye Removal. *ACS Appl. Mater. Interfaces* **2016**, *8* (27), 17194–17204. https://doi.org/10.1021/acsami.6b03158.

(40) Sharma, M.; Choudhury, D.; Hazra, S.; Basu, S. Effective Removal of Metal Ions from Aqueous Solution by Mesoporous MnO_2 and TiO_2 Monoliths: Kinetic and Equilibrium Modelling. *J. Alloys Compd.* **2017**, *720*, 221–229. https://doi.org/10.1016/j.jallcom.2017.05.260.

(41) Singh, J.; Sharma, M.; Basu, S. Heavy Metal Ions Adsorption and Photodegradation of Remazol Black XP by Iron Oxide/Silica Monoliths: Kinetic and Equilibrium Modelling. *Adv. Powder Technol.* **2018**, *29* (9), 2268–2279. https://doi.org/10.1016/j.apt.2018.06.011.

(42) He, J.; Chen, S.-Y.; Tang, W.; Dang, Y.; Kerns, P.; Miao, R.; Dutta, B.; Gao, P.-X.; Suib, S. L. Microwave-Assisted Integration of Transition Metal Oxide Nanocoatings on Manganese Oxide Nanoarray Monoliths for Low Temperature CO Oxidation. *Appl. Catal. B Environ.* **2019**, *255*, 117766. https://doi.org/10.1016/j.apcatb.2019.117766.

(43) Pirmoradi, M.; Janulaitis, N.; Gulotty, R. J.; Kastner, J. R. Bi-Metal-Supported Activated Carbon Monolith Catalysts for Selective Hydrogenation of Furfural. *Ind. Eng. Chem. Res.* **2020**, *59* (40), 17748–17761. https://doi.org/10.1021/acs.iecr.0c02866.

(44) Christy, E. J. S.; Alagar, R.; M, D.; Pius, A. Porous Nonhierarchical CeO_2/SiO_2 Monolith for Effective Degradation of Organic Pollutants. *Environ. Nanotechnology, Monit. Manag.* **2020**, *14*, 100365. https://doi.org/10.1016/j.enmm.2020.100365.

(45) Nabil, K.; Abdelmonem, N.; Nogami, M.; Ismail, I. Preparation of Composite Monolith Supercapacitor Electrode Made from Textile-Grade Polyacrylonitrile Fibers and Phenolic Resin. *Materials (Basel).* **2020**, *13* (3), 655. https://doi.org/10.3390/ma13030655.

(46) Chae, J. A.; Jeong, S.; Kim, H. J.; Tojo, T.; Oh, Y.; Chi, W. S.; Yoon, H.; Kim, H. Fibrous Mesoporous Polymer Monoliths: Macromolecular Design and Enhanced Photocatalytic Degradation of Aromatic Dyes. *Polym. Chem.* **2021**, *12* (16), 2464–2470. https://doi.org/10.1039/D1PY00049G.

(47) Yan, Y.; Zang, L.; Dou, T.; Li, H.; Sun, L.; Zhang, Y. Hollow Co_3O_4 Nanoparticles Immobilized RGO/Carbon Monolith as an Electrode Material for High-Performance Supercapacitors. *Ceram. Int.* **2021**, *47* (14), 20310–20316. https://doi.org/10.1016/j.ceramint.2021.04.039.

(48) Nakanishi, K.; Soga, N. Phase Separation in Gelling Silica-Organic Polymer Solution: Systems Containing Poly(Sodium Styrenesulfonate). *J. Am. Ceram. Soc.* **1991**, *74* (10), 2518–2530. https://doi.org/10.1111/j.1151-2916.1991.tb06794.x.

(49) Kallawar, G. A.; Bhanvase, B. A. Nanomaterial-Based Photocatalytic Membrane for

Organic Pollutants Removal. In *Handbook of Nanomaterials for Wastewater Treatment*; Elsevier, 2021; pp 699–737. https://doi.org/10.1016/B978-0-12-821496-1.00007-6.

(50) Feinle, A.; Elsaesser, M. S.; Hüsing, N. Sol–Gel Synthesis of Monolithic Materials with Hierarchical Porosity. *Chem. Soc. Rev.* **2016**, *45* (12), 3377–3399. https://doi.org/10.1039/C5CS00710K.

(51) Bueno; Mayer; Weber; Bechelany; Klotz; Farrusseng. Impregnation Protocols on Alumina Beads for Controlling the Preparation of Supported Metal Catalysts. *Catalysts* **2019**, *9* (7), 577. https://doi.org/10.3390/catal9070577.

(52) Munnik, P.; de Jongh, P. E.; de Jong, K. P. Recent Developments in the Synthesis of Supported Catalysts. *Chem. Rev.* **2015**, *115* (14), 6687–6718. https://doi.org/10.1021/cr500486u.

(53) Komiyama, M. Design and Preparation of Impregnated Catalysts. *Catal. Rev.* **1985**, *27* (2), 341–372. https://doi.org/10.1080/01614948508064738.

(54) Mishra, A.; Mehta, A.; Basu, S.; Shetti, N. P.; Reddy, K. R.; Aminabhavi, T. M. Graphitic Carbon Nitride (g–C_3N_4)–Based Metal-Free Photocatalysts for Water Splitting: A Review. *Carbon N. Y.* **2019**, *149*, 693–721. https://doi.org/10.1016/j.carbon.2019.04.104.

(55) Grover, A.; Mohiuddin, I.; Malik, A. K.; Aulakh, J. S.; Kim, K.-H. Zn-Al Layered Double Hydroxides Intercalated with Surfactant: Synthesis and Applications for Efficient Removal of Organic Dyes. *J. Clean. Prod.* **2019**, *240*, 118090. https://doi.org/10.1016/j.jclepro.2019.118090.

(56) Monga, D.; Basu, S. Enhanced Photocatalytic Degradation of Industrial Dye by G-C_3N_4/TiO_2 Nanocomposite: Role of Shape of TiO_2. *Adv. Powder Technol.* **2019**, *30* (5), 1089–1098. https://doi.org/10.1016/j.apt.2019.03.004.

(57) Lellis, B.; Fávaro-Polonio, C. Z.; Pamphile, J. A.; Polonio, J. C. Effects of Textile Dyes on Health and the Environment and Bioremediation Potential of Living Organisms. *Biotechnol. Res. Innov.* **2019**, *3* (2), 275–290. https://doi.org/10.1016/j.biori.2019.09.001.

(58) Díez, A. M.; Sanromán, M. A.; Pazos, M. New Approaches on the Agrochemicals

Degradation by UV Oxidation Processes. *Chem. Eng. J.* **2019**, *376*, 120026. https://doi.org/10.1016/j.cej.2018.09.187.

(59) Jones, L.; Kinsella, B.; Forde, K.; Furey, A.; Regan, F. A Robust Analytical Method for the Determination of Pesticide Residues in Wastewater. *Anal. Methods* **2017**, *9* (28), 4167–4174. https://doi.org/10.1039/C7AY00704C.

(60) Peiter, A.; Fiuza, T. E. R.; de Matos, R.; Antunes, A. C.; Antunes, S. R. M.; Lindino, C. A. System Development for Concomitant Degradation of Pesticides and Power Generation. *Water, Air, Soil Pollut.* **2017**, *228* (3), 114. https://doi.org/10.1007/s11270-017-3298-4.

(61) Pipi, A. R. F.; De Andrade, A. R.; Brillas, E.; Sirés, I. Total Removal of Alachlor from Water by Electrochemical Processes. *Sep. Purif. Technol.* **2014**, *132*, 674–683. https://doi.org/10.1016/j.seppur.2014.06.022.

(62) Mehta, T.; Rathi, A.; Verma, A.; Barman, S.; Halder, G. Elimination of Fipronil Insecticide by Adsorption Technique from Aqueous Solution by Cu-13X Zeolite Composite: Isotherms, Kinetic and Thermodynamic Studies. *Int. J. Environ. Anal. Chem.* **2020**, 1–17. https://doi.org/10.1080/03067319.2020.1790545.

(63) Mostafalou, S.; Abdollahi, M. Pesticides and Human Chronic Diseases: Evidences, Mechanisms, and Perspectives. *Toxicol. Appl. Pharmacol.* **2013**, *268* (2), 157–177. https://doi.org/10.1016/j.taap.2013.01.025.

(64) Sabarwal, A.; Kumar, K.; Singh, R. P. Hazardous Effects of Chemical Pesticides on Human Health–Cancer and Other Associated Disorders. *Environ. Toxicol. Pharmacol.* **2018**, *63*, 103–114. https://doi.org/10.1016/j.etap.2018.08.018.

(65) Kanakaraju, D.; Glass, B. D.; Oelgemöller, M. Advanced Oxidation Process-Mediated Removal of Pharmaceuticals from Water: A Review. *J. Environ. Manage.* **2018**, *219*, 189–207. https://doi.org/10.1016/j.jenvman.2018.04.103.

(66) Mohiuddin, I.; Grover, A.; Aulakh, J. S.; Lee, S.-S.; Malik, A. K.; Kim, K.-H. Porous Molecularly-Imprinted Polymer for Detecting Diclofenac in Aqueous Pharmaceutical Compounds. *Chem. Eng. J.* **2020**, *382*, 123002. https://doi.org/10.1016/j.cej.2019.123002.

(67) Tiwari, B.; Sellamuthu, B.; Ouarda, Y.; Drogui, P.; Tyagi, R. D.; Buelna, G. Review on Fate and Mechanism of Removal of Pharmaceutical Pollutants from Wastewater Using Biological Approach. *Bioresour. Technol.* **2017**, *224*, 1–12. https://doi.org/10.1016/j.biortech.2016.11.042.

(68) Samsudin, M. F. R.; Bacho, N.; Sufian, S.; Ng, Y. H. Photocatalytic Degradation of Phenol Wastewater over Z-Scheme g-C_3N_4/CNT/$BiVO_4$ Heterostructure Photocatalyst under Solar Light Irradiation. *J. Mol. Liq.* **2019**, *277*, 977–988. https://doi.org/10.1016/j.molliq.2018.10.160.

(69) Changotra, R.; Rajput, H.; Paul Guin, J.; Varshney, L.; Dhir, A. Hybrid Coagulation, Gamma Irradiation and Biological Treatment of Real Pharmaceutical Wastewater. *Chem. Eng. J.* **2019**, *370*, 595–605. https://doi.org/10.1016/j.cej.2019.03.256.

(70) Brillas, E.; Martínez-Huitle, C. A. Decontamination of Wastewaters Containing Synthetic Organic Dyes by Electrochemical Methods. An Updated Review. *Appl. Catal. B Environ.* **2015**, *166–167*, 603–643. https://doi.org/10.1016/j.apcatb.2014.11.016.

(71) Lepland, A.; Andersen, T. J.; Lepland, A.; Arp, H. P. H.; Alve, E.; Breedveld, G. D.; Rindby, A. Sedimentation and Chronology of Heavy Metal Pollution in Oslo Harbor, Norway. *Mar. Pollut. Bull.* **2010**, *60* (9), 1512–1522. https://doi.org/10.1016/j.marpolbul.2010.04.017.

(72) Lee, C. O.; Howe, K. J.; Thomson, B. M. Ozone and Biofiltration as an Alternative to Reverse Osmosis for Removing PPCPs and Micropollutants from Treated Wastewater. *Water Res.* **2012**, *46* (4), 1005–1014. https://doi.org/10.1016/j.watres.2011.11.069.

(73) Akpan, U. G.; Hameed, B. H. Parameters Affecting the Photocatalytic Degradation of Dyes Using TiO_2-Based Photocatalysts: A Review. *Journal of Hazardous Materials*. 2009, pp 520–529. https://doi.org/10.1016/j.jhazmat.2009.05.039.

(74) Liu, Y.; Yang, B.; He, H.; Yang, S.; Duan, X.; Wang, S. Bismuth-Based Complex Oxides for Photocatalytic Applications in Environmental Remediation and Water Splitting: A Review. *Sci. Total Environ.* **2022**, *804*, 150215. https://doi.org/10.1016/j.scitotenv.2021.150215.

(75) Dong, S.; Feng, J.; Fan, M.; Pi, Y.; Hu, L.; Han, X.; Liu, M.; Sun, J.; Sun, J. Recent Developments in Heterogeneous Photocatalytic Water Treatment Using Visible Light-Responsive Photocatalysts: A Review. *RSC Adv.* **2015**, *5* (19), 14610–14630. https://doi.org/10.1039/c4ra13734e.

(76) Herrmann, J.-M. Heterogeneous Photocatalysis: Fundamentals and Applications to the Removal of Various Types of Aqueous Pollutants. *Catal. Today* **1999**, *53* (1), 115–129. https://doi.org/10.1016/S0920-5861(99)00107-8.

(77) Qu, X.; Alvarez, P. J. J.; Li, Q. Applications of Nanotechnology in Water and Wastewater Treatment. *Water Res.* **2013**, *47* (12), 3931–3946. https://doi.org/10.1016/j.watres.2012.09.058.

(78) Gu, L.; Wang, J.; Zou, Z.; Han, X. Graphitic-C_3N_4-Hybridized TiO_2 Nanosheets with Reactive {001} Facets to Enhance the UV- and Visible-Light Photocatalytic Activity. *J. Hazard. Mater.* **2014**, *268*, 216–223. https://doi.org/10.1016/j.jhazmat.2014.01.021.

(79) Zhu, X.; Zhang, J.; Chen, F. Hydrothermal Synthesis of Nanostructures $Bi_{12}TiO_{20}$ and Their Photocatalytic Activity on Acid Orange 7 under Visible Light. *Chemosphere* **2010**, *78* (11), 1350–1355. https://doi.org/10.1016/j.chemosphere.2010.01.002.

(80) Ahmed, S.; Rasul, M. G.; Martens, W. N.; Brown, R.; Hashib, M. A. Advances in Heterogeneous Photocatalytic Degradation of Phenols and Dyes in Wastewater: A Review. *Water, Air, Soil Pollut.* **2011**, *215* (1–4), 3–29. https://doi.org/10.1007/s11270-010-0456-3.

(81) Saeed, M.; Muneer, M.; Haq, A. ul; Akram, N. Photocatalysis: An Effective Tool for Photodegradation of Dyes—a Review. *Environ. Sci. Pollut. Res.* **2022**, *29* (1), 293–311. https://doi.org/10.1007/s11356-021-16389-7.

(82) Anwer, H.; Mahmood, A.; Lee, J.; Kim, K. H.; Park, J. W.; Yip, A. C. K. Photocatalysts for Degradation of Dyes in Industrial Effluents: Opportunities and Challenges. *Nano Res.* **2019**, *12* (5), 955–972. https://doi.org/10.1007/s12274-019-2287-0.

(83) Low, J.; Yu, J.; Jaroniec, M.; Wageh, S.; Al-Ghamdi, A. A. Heterojunction Photocatalysts. *Adv. Mater.* **2017**, *29* (20), 1601694. https://doi.org/10.1002/adma.201601694.

(84) Wang, Z.; Lin, Z.; Shen, S.; Zhong, W.; Cao, S. Advances in Designing Heterojunction Photocatalytic Materials. *Chinese J. Catal.* **2021**, *42* (5), 710–730. https://doi.org/10.1016/S1872-2067(20)63698-1.

(85) Lai, Y.-J.; Lee, D.-J. Pollutant Degradation with Mediator Z-Scheme Heterojunction Photocatalyst in Water: A Review. *Chemosphere* **2021**, *282*, 131059. https://doi.org/10.1016/j.chemosphere.2021.131059.

(86) Xu, Q.; Zhang, L.; Yu, J.; Wageh, S.; Al-Ghamdi, A. A.; Jaroniec, M. Direct Z-Scheme Photocatalysts: Principles, Synthesis, and Applications. *Mater. Today* **2018**, *21* (10), 1042–1063. https://doi.org/10.1016/j.mattod.2018.04.008.

(87) Xu, Q.; Zhang, L.; Cheng, B.; Fan, J.; Yu, J. S-Scheme Heterojunction Photocatalyst. *Chem* **2020**, *6* (7), 1543–1559. https://doi.org/10.1016/j.chempr.2020.06.010.

(88) Zhang, L.; Zhang, J.; Yu, H.; Yu, J. Emerging S-Scheme Photocatalyst. *Adv. Mater.* **2022**, *34* (11), 2107668. https://doi.org/10.1002/adma.202107668.

(89) Yu, C.; Zhou, W.; Yu, J. C.; Liu, H.; Wei, L. Design and Fabrication of Heterojunction Photocatalysts for Energy Conversion and Pollutant Degradation. *Chinese J. Catal.* **2014**, *35* (10), 1609–1618. https://doi.org/10.1016/S1872-2067(14)60170-4.

(90) Ma, W.; Li, Z.; Liu, W. Hydrothermal Preparation of $BiVO_4$ Photocatalyst with Perforated Hollow Morphology and Its Performance on Methylene Blue Degradation. *Ceram. Int.* **2015**, *41* (3), 4340–4347. https://doi.org/10.1016/j.ceramint.2014.11.123.

(91) Reddy, K. R.; Karthik, K. V; Prasad, S. B. B.; Soni, S. K.; Jeong, H. M.; Raghu, A. V. Enhanced Photocatalytic Activity of Nanostructured Titanium Dioxide/Polyaniline Hybrid Photocatalysts. *Polyhedron* **2016**, *120*, 169–174. https://doi.org/10.1016/j.poly.2016.08.029.

(92) Pei, Z.-Z.; Liu, Y.-B.; Jia, H.; Zhou, J.-X.; Li, F.; Wang, X.; He, X.-H. Controllable Synthesis of Flower-Like MoS_2 and Its Quick Photodegradation of Methylene Blue Under Visible Irradiation . *J. Nanosci. Nanotechnol.* **2019**, *20* (5), 3013–3018. https://doi.org/10.1166/jnn.2020.17464.

(93) Shayegan Mehr, E.; Sorbiun, M.; Ramazani, A.; Taghavi Fardood, S. Plant-Mediated Synthesis of Zinc Oxide and Copper Oxide Nanoparticles by Using Ferulago Angulata (Schlecht) Boiss Extract and Comparison of Their Photocatalytic Degradation of Rhodamine B (RhB) under Visible Light Irradiation. *J. Mater. Sci. Mater. Electron.* **2018**, *29* (2), 1333–1340. https://doi.org/10.1007/s10854-017-8039-3.

(94) Zhang, X.; Yi, J.; Chen, H.; Mao, M.; Liu, L.; She, X.; Ji, H.; Wu, X.; Yuan, S.; Xu, H.; et al. Construction of a Few-Layer g-C_3N_4/α-MoO_3 Nanoneedles All-Solid-State Z-Scheme Photocatalytic System for Photocatalytic Degradation. *J. Energy Chem.* **2019**, *29*, 65–71. https://doi.org/10.1016/j.jechem.2018.01.014.

(95) Cao, F.; Wang, T.; Ji, X. Enhanced Visible Photocatalytic Activity of Tree-like ZnO/CuO Nanostructure on Cu Foam. *Appl. Surf. Sci.* **2019**, *471*, 417–424. https://doi.org/10.1016/j.apsusc.2018.12.034.

(96) Das, J.; Dhar, S. S. Synthesis of SnO_2 Quantum Dots Mediated by Camellia Sinensis Shoots for Degradation of Thiamethoxam. *Toxicol. Environ. Chem.* **2020**, *102* (1–4), 186–196. https://doi.org/10.1080/02772248.2020.1776285.

(97) Lee, Y.-J.; Kang, J.-K.; Park, S.-J.; Lee, C.-G.; Moon, J.-K.; Alvarez, P. J. J. Photocatalytic Degradation of Neonicotinoid Insecticides Using Sulfate-Doped Ag_3PO_4 with Enhanced Visible Light Activity. *Chem. Eng. J.* **2020**, *402*, 126183. https://doi.org/10.1016/j.cej.2020.126183.

(98) Jansanthea, P.; Saovakon, C.; Chomkitichai, W.; Ketwaraporn, J.; Maneepong, S.; Chaiwong, N.; Jaisee, K.; Wansao, C.; Wanaek, A.; Pookmanee, P. Thiamethoxam Insecticide Degradation with a Leaf-Like Cupric Oxide Monoclinic Structure Synthesized via the Microwave Method. *Russ. J. Inorg. Chem.* **2021**, *66* (5), 667–678. https://doi.org/10.1134/S0036023621050089.

(99) Zhao, Z.; Fan, J.; Deng, X.; Liu, J. One-Step Synthesis of Phosphorus-Doped g-C_3N_4/Co_3O_4 Quantum Dots from Vitamin B12 with Enhanced Visible-Light Photocatalytic Activity for Metronidazole Degradation. *Chem. Eng. J.* **2019**, *360*, 1517–1529. https://doi.org/10.1016/j.cej.2018.10.239.

(100) Nogueira, A. C.; Gomes, L. E.; Ferencz, J. A. P.; Rodrigues, J. E. F. S.; Goncąlves, R. V.; Wender, H. Improved Visible Light Photoactivity of $CuBi_2O_4$/CuO Heterojunctions for Photodegradataaion of Methylene Blue and Metronidazole. *J. Phys. Chem. C* **2019**, *123* (42), 25680–25690. https://doi.org/10.1021/acs.jpcc.9b06907.

(101) Nasiri, A.; Tamaddon, F.; Mosslemin, M. H.; Gharaghani, M. A.; Asadipour, A. New Magnetic Nanobiocomposite $CoFe_2O_4$@methycellulose: Facile Synthesis, Characterization, and Photocatalytic Degradation of Metronidazole. *J. Mater. Sci. Mater. Electron.* **2019**, *30* (9), 8595–8610. https://doi.org/10.1007/s10854-019-01182-7.

(102) Braslavsky, S. E.; Braun, A. M.; Cassano, A. E.; Emeline, A. V.; Litter, M. I.; Palmisano, L.; Parmon, V. N.; Serpone, N. Glossary of Terms Used in Photocatalysis and Radiation Catalysis (IUPAC Recommendations 2011). *Pure Appl. Chem.* **2011**, *83* (4), 931–1014. https://doi.org/10.1351/PAC-REC-09-09-36.

(103) Karthikeyan, S.; Chuaicham, C.; Pawar, R. R.; Sasaki, K.; Li, W.; Lee, A. F.; Wilson, K. Template Free Mild Hydrothermal Synthesis of Core–Shell Cu_2O(Cu)@CuO Visible Light Photocatalysts for N -Acetyl- Para -Aminophenol Degradation. *J. Mater. Chem. A* **2019**, *7* (36), 20767–20777. https://doi.org/10.1039/C9TA07009E.

(104) Ajmal, A.; Majeed, I.; Malik, R. N.; Idriss, H.; Nadeem, M. A. Principles and Mechanisms of Photocatalytic Dye Degradation on TiO_2 Based Photocatalysts: A Comparative Overview. *RSC Adv.* **2014**, *4* (70), 37003–37026. https://doi.org/10.1039/c4ra06658h.

(105) UshaVipinachandran, V.; Rajendran, S.; Badagoppam Haroon, K. H.; Ashokan, I.; Mondal, A.; Bhunia, S. K. Detoxification of Endocrine Disruptors in Water Using Visible-Light-Active Nanostructures: A Review. *ACS Appl. Nano Mater.* **2020**, *3* (12), 11659–11687. https://doi.org/10.1021/acsanm.0c02974.

(106) Enesca, A. The Influence of Photocatalytic Reactors Design and Operating Parameters on the Wastewater Organic Pollutants Removal—A Mini-Review. *Catalysts* **2021**, *11* (5), 556. https://doi.org/10.3390/catal11050556.

(107) McCullagh, C.; Skillen, N.; Adams, M.; Robertson, P. K. J. Photocatalytic Reactors for Environmental Remediation: A Review. *J. Chem. Technol. Biotechnol.* **2011**, *86* (8), 1002–

1017. https://doi.org/10.1002/jctb.2650.

(108) Bertagna Silva, D.; Buttiglieri, G.; Babić, S. State-of-the-Art and Current Challenges for TiO_2/UV-LED Photocatalytic Degradation of Emerging Organic Micropollutants. *Environ. Sci. Pollut. Res.* **2021**, *28* (1), 103–120. https://doi.org/10.1007/s11356-020-11125-z.

(109) Anjugam Vandarkuzhali, S. A.; Pugazhenthiran, N.; Mangalaraja, R. V; Sathishkumar, P.; Viswanathan, B.; Anandan, S. Ultrasmall Plasmonic Nanoparticles Decorated Hierarchical Mesoporous TiO_2 as an Efficient Photocatalyst for Photocatalytic Degradation of Textile Dyes. *ACS Omega* **2018**, *3* (8), 9834–9845. https://doi.org/10.1021/acsomega.8b01322.

Chapter 2

Visible-light active hierarchical porous WO_3/SiO_2 monolith in centimeter length scale for photocatalytic degradation of toxic organic pollutants

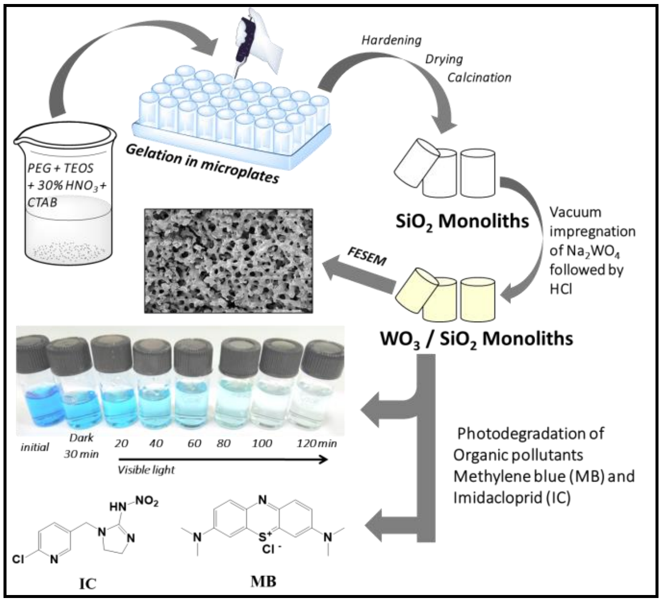

Highlights

- Visible light-active WO_3/SiO_2 monoliths with a high surface area and hierarchical morphology were synthesized by wet impregnation method.
- The monoliths effectively degraded toxic dye methylene blue and insecticide imidacloprid.
- The solid rock-like structure of monolith is easily recoverable from reaction mixture after the photocatalytic reaction.
- High reusability of monolith (~80% after 5 successive runs) is helpful for its use at large scale for wastewater treatment.

2.1 Introduction

Dyes are natural or man-made colored compounds that find various applications not only in textile industry but also in food industry, cosmetics, dye sensitized solar cells, UV protective clothing, as pH indicator, paper, leather etc.[1] Dye pollutants enter the natural water bodies and impact environment and eventually human health really adversely. The textile industry is one of the key role players in water pollution globally. As reported in 2015, above 20% of the recorded levels of water pollution in some countries like Turkey, Indonesia and China are caused by textile industry.[2] This extremely harmful and colored waste not only depreciates the water quality but also elevates the toxicity. The improper dumping of textile effluents is also related with carcinogenicity and mutagenicity.[3] Apart from dyes, colorless pollutants like pesticides and other phenolic compounds are a fatal threat to environment.[4] This is why; it is essentially need of the hour to remove these harmful and potentially lethal moieties before they get discharged into aqueous media.

Several methods have been tried to eradicate the unremitting pollutants discharged into aquatic domain such as adsorption, chemical precipitation, solvent extraction, biological process, sedimentation and electrochemical processes.[4,5] However, these methods proceed rather slowly, require temperature/pressure control and are not cost friendly. Additionally, these methods don't completely eliminate the major pollutant but may lead to its transformation into minor pollutants that require further removal.[6] However, photocatalysis is considered a comparatively better option and has come across as a very appealing choice for the degradation of dyes and waste water treatment. It attributes to the simplicity, cost-friendliness, high efficiency of photocatalysis and the tendency to make use of sunlight for the exclusion of organic pollutants with the help of a solid photocatalyst. Further, through photocatalysis, toxic pollutants can be completely eradicated as the dye can be transformed to CO_2 and H_2O.[6]

Conventionally, metal oxides like TiO_2 synthesized from different methods have been explored extensively in this respect.[7] However, TiO_2 exhibits unsatisfactory photoactivity in visible light owing to its large band-gap (~ 3.2 eV). In addition, the UV radiation needed for the excitation of TiO_2 constitutes only about 4-5% in the solar spectrum which restrains the practical applications.[8] Many interesting nanostructures are being designed nowadays for photocatalysis. Recently, tungsten trioxide (WO_3) has emerged as a noteworthy photocatalyst. WO_3 is an n-type semiconductor having a relatively small energy band gap (2.4-2.8 eV) and high oxidation power of valence band (VB) holes (+3.1-3.2 V_{NHE}). Therefore, it can prove to be effective in visible region. The CB potential of WO_3 (~ +0.74V) is more positive than the potential for the single-electron reduction of oxygen (~ −0.28V), and thus superoxide anion radicals can't be formed. However, the VB potential of WO_3 (~ +3.44V) is suitable for the formation of hydroxyl radicals by the oxidation of water (~ +1.23V) by the photogenerated holes. Moreover, the multielectron O_2 reduction can proficiently facilitate the generation of H_2O_2 over WO_3.[9,10] Moreover, it is harmless, inexpensive, corrosion-free and stable in oxidative conditions and aqueous media over a wide pH range.[11,12] The WO_3-based photocatalysts have found applications not only in photodegradation but various domains like air purification, CO_2 photoreduction, treatment of heavy metal ions, disinfection of bacteria, hydrogen evolution from water splitting, etc. But, a low surface area and moderate solubility discourages it from being a naturally efficient photocatalyst.[13] Nevertheless, morphological modifications can help in rectifying this shortcoming. Enhancement in the surface area could help to improve the photocatalytic activity and efficiency because photodegradation is typically a surface-based process. In this respect, different morphologies of WO_3 have been investigated to date such as, one-dimensional nanostructures like nanorods, nanotubes, nanofibres, two- dimensional nanosheets, three-dimensional porous structures and quantum-confined WO_3 nanoparticles. Innumerable methods have been reported for WO_3 nanostructure synthesis like hydrothermal reactions,[14] template-mediated synthesis,[15] electrochemical techniques,[16] sol-gel process[17], etc.

However, these methods are not very efficient and also it can be seen from the literature that most of these synthesized metal oxides are in a powder or liquid form. The repercussion of this fact is that these catalysts make a miscible suspension with water that further requires filters of superior grade and sophisticated instruments for its separation from the solution. One way out of this problem is to use metal oxide monoliths having rock like structure in centimeter scale which have drawn huge interest recently owing to the multimodal porosity offered by them.[18,19] Firstly the silica monoliths are prepared which are later used to synthesize hierarchically porous metal oxide monoliths. It is reported that silica monoliths of nearly any shape can be designed having both interconnected macropores along with textural mesoporosity.[20] Hierarchical photocatalysts have high surface area and increased number of active sites which speeds up the reaction kinetics on surface along with greater light uptake and transport kinetics.[10] This method is easy to use, economical and gives a highly porous catalyst having very high surface area. Further, the surface of WO_3 acquires highly negative surface charges due to low isoelectric point (IEP = 0.2−1) making it suitable for adsorption particularly for cationic dyes like Rh-B and MB etc.[21]

MB is a cationic thiazine dye having an intense color and finds application in dyeing and printing.[22] It is reported to have a detrimental neurotoxic effect on the central nervous system,[23] and a prolonged contact to it could cause several ailments like nausea, anemia and hypertension.[24] Therefore, it is vital to study the efficient ways to remove it from waste water.[25] Azimirad *et al.*[26] reported 85% photodegradation in 140 minutes using 3D graphene foam-WO_3, whereas Dinari *et al.*[27] reported 75% photodegradation in 150 minutes using WO_3/NWCNT. Prabhu *et al.*[28] also reported 65% photodegradation in 60 minutes using rGO-WO_3. However, the monolithic WO_3/SiO_2 nanostructures have not been used for the photocatalytic degradation of MB before and not much has been reported in the literature about them. Further, imidacloprid is an insecticide which belongs to the ‘neonicotinoids’. It is profoundly used in the pest control in agricultural fields. However, it is quite hazardous for non-target soil organisms like earthworms and bees which led to its ban in France. Its toxic effect on agrosystems, organisms and human health requires attention.[29]

This chapter deals with the synthesis of porous WO_3/SiO_2 monolith by simple wet impregnation method and examination of its photocatalytic application thereafter. Here, first SiO_2 monoliths were synthesized by sol-gel method that act as a catalyst support and then further impregnation of WO_3 precursor (sodium tungstate) was carried out to obtain desired product. This photocatalyst was then used for the photodegradation of model dye MB. Different parameters like effects of pH of pollutant and concentration of catalyst were studied along with trapping experiments to examine the governing reactive species in the mechanism of degradation and the reusability of photocatalyst was also investigated. The catalyst was also characterized after 2 cycles of photodegradation to justify its high reusability efficiency. Photodegradation of colorless insecticide, IC was also carried out to differentiate between direct and indirect photocatalysis. The originality of this investigation lies in the fact that WO_3/SiO_2 monoliths prepared by wet impregnation method have not been used for the photocatalysis purpose before with an extensive study of various factors affecting photodegradation.

2.2 Experimental section

This section comprises of the chemicals, materials and the methodologies used for the synthesis of catalysts.

2.2.1 Chemicals and materials

Tetraethoxysilane (TEOS) was acquired from Alfa Aesar. Polyethylene glycol (PEG) (MW 35,000 g/mol), cetyltrimethyl bromide (CTAB) and imidacloprid were obtained from Sigma-Aldrich. Ammonia (28-30%), hydrochloric acid (37%), nitric acid (69%), sodium tungstate dihydrate and methylene blue were bought from Merck. All the reagents were of analytical grade and were employed with no more purification.

2.2.2 Syntheses

This section includes the synthesis methodologies of SiO_2 monoliths and WO_3/SiO_2 monoliths.

2.2.2.1 Synthesis of SiO_2 monoliths

Silica monoliths (SiO_2) were synthesized using the sol-gel process.[30] A clear solution of 1.38 mL nitric acid (HNO_3) (30%) and PEG (9.54×10^{-4} M) was prepared in 8.25 mL distilled water. To this solution, TEOS (8.1 mL) was mixed by consistently stirring at room temperature for about 15-20 min until a translucent sol was attained. Subsequently, 1.3 g CTAB was added to this solution with constant mixing till it got wholly dissolved. The CTAB acts as the surfactant template and helps in forming the mesoporous structures in monoliths. The solution so obtained was further shifted to microplates and it can be molded into any desired shape. It was placed in an oven at 40°C for minimum 72 h for firstly the conversion of sol to gel and finally its aging. Then for the hardening process, treatment of the monoliths with (1M) (ammonium hydroxide) NH_4OH solution was done at 90°C for 9 h followed by the treatment with (0.1 M) HNO_3 solution which does the neutralization. Washing of the monoliths with de-ionized water was done subsequently for 5 to 7 times and then placed in oven for drying at 40°C for 4-5 days. Finally, SiO_2 monoliths were calcined for 5 h at 550°C at a heating rate of 1°C/min.

2.2.2.2 Synthesis of WO_3/SiO_2 monoliths

The as prepared SiO_2 monoliths were taken in a round-bottom flask and degassed for 3-5 h using a vacuum pump to remove the unwanted impurities and trapped gases from the surface of the monoliths. A clear aqueous solution of 1 M sodium tungstate dihydrate solution was prepared and the monoliths were impregnated with this solution. The monoliths were properly dipped in the solution and degassing was continued for another 5-6 h. It was followed by the treatment with 1 M HCl solution and then drying at 40°C. These steps were repeated for five times for achieving best impregnation. Finally, calcination of WO_3/SiO_2 monoliths was done at 500°C with 1°C/min heating ramp for 5 h. The synthesized monoliths were 0.7 cm long and 0.5 cm in diameter. To study the variation in photocatalytic activity due to SiO_2 to WO_3 molar ratio, fixed amount of SiO_2 monoliths were impregnated with same volume of 0.5 M and 1.5 M WO_3 precursor (Sodium tungstate dihydrate) respectively. **Scheme 2.1** represents the real time images for the synthesis procedure for parent SiO_2 monoliths along with WO_3/SiO_2 monoliths.

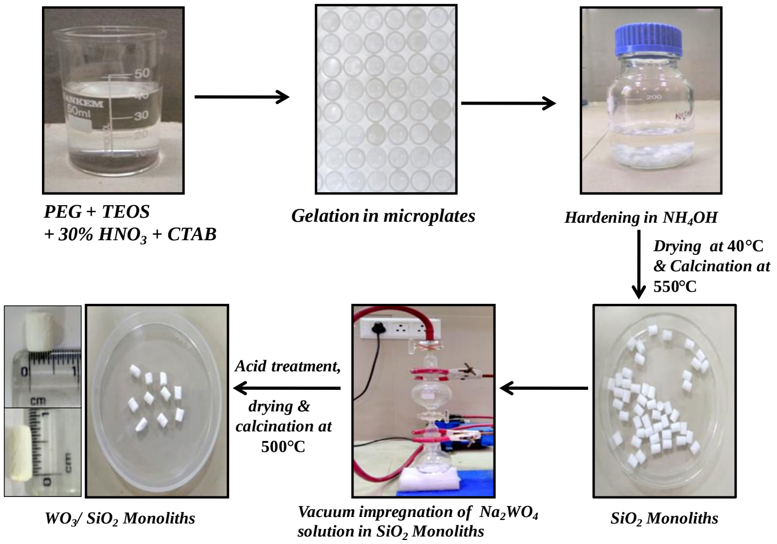

Scheme 2.1. Illustrative description for the synthesis of porous SiO_2 and WO_3/SiO_2 monoliths.

2.2.3 Characterization methods

Nitrogen sorption analysis was done by Microtrac Belsorp Mini-II (Bel, Japan, Inc) surface area analyzer. The surface area was obtained by Brunner-Emmet-Teller (BET) method. The samples were pre-treated under nitrogen atmosphere at 120°C for 6 h before carrying out the analysis. The pore size distribution curves were attained using Barrett-Joyner-Halenda (BJH) method. The X-ray diffraction analysis (XRD) of the WO_3/SiO_2 monolith was carried out by making use of PANalytical X-ray diffractometer using Cu Kα radiation (λ= 1.54 Å), operating at 45 kV with the scan range of 10–90°. Morphological studies of the monoliths were executed by means of SU8180, Hitachi FESEM operating at 15 kV, attached with Oxford INCA energy dispersive spectrometer (EDS). The oxidation states of metal oxide in the synthesized monoliths were ascertained from PHI-5200 X-ray photoelectron spectroscopy (XPS) system having a monochromatic Al Kα X-ray source (1486.7 eV). UV–Vis diffuse reflectance spectroscopy (DRS) was carried out in diffuse absorbance mode through Hitachi-3900H spectrophotometer. The pH was adjusted and measured by making use of pH meter, model cyber scan pH 1100 (Eutech, Singapore). The kinetic analysis for the photodegradation of MB and IC was done by UV–Vis spectrophotometer (Specord 205, Analytik Jena).

2.2.4 Photocatalytic activity

The photocatalytic efficacy of WO_3/SiO_2 was examined for the degradation of MB and colorless insecticide IC. About 1 mg of the photocatalyst was added to 10 mL solution of 5 ppm MB in a quartz beaker. The solution was mixed for 30 min in dark until adsorption-desorption equilibrium between the surface of catalyst and dye was attained. Then the solution was illuminated with visible radiation for 2 h until complete degradation was achieved. Similarly, 5 mg photocatalyst was added to 10 mL solution of 10 ppm IC and was stirred in dark for 20 min to establish adsorption-desorption equilibrium and then irradiated under visible light for 60 min. A 65 W CFL lamp (Phillips, k > 400 nm) with intensity of 125 W/m^2 was made to use for supplying visible light for the photocatalytic reaction. The gap between the lamp and the beaker was around 10 cm. The absorbance spectra of MB and IC was examined using a UV–visible spectrophotometer at λ_{max} = 665 nm and 270 nm respectively at regular intervals after separation of photocatalyst. Further, as according to Beer-Lambert's law, concentration is directly proportional to absorbance, therefore the degradation efficiency or percent degradation was simply evaluated using **Eq. (2.1)**, where, A_0, A_t, and C_0, C denote the absorbance and concentration of pollutant at time ‘0’ and ‘t’, respectively.

$$\% D = \{(A_0 - A_t)/A_0\} \times 100 = \{(C_0 - C)/C_0\} \times 100 \qquad (2.1)$$

For the analysis of degradation products, GC-MS analysis was done. Samples for GC-MS were prepared as follows: The aqueous reaction mixture was collected after the photocatalytic reaction and catalyst was separated. The solvent was removed by drying at 40°C and the residue was dissolved in dichloromethane. Shimadzu QP-2010 Plus with Thermal Desorption System TD 20. Conditions - split mode injector, helium carrier gas (flow rate=1 mL/min), injection volume= 1.21 µL, injector temperature= 260°C, ion source temperature =220°C. The initial oven temperature was 100°C for 2 min hold time and increased to 280 °C at a ramp of 10 °C min^{-1} with a 20 min hold time. MS spectra were attained at a range m/z =40-650, scan speed=3333.

2.3 Results and discussion

2.3.1 Nitrogen adsorption-desorption analysis

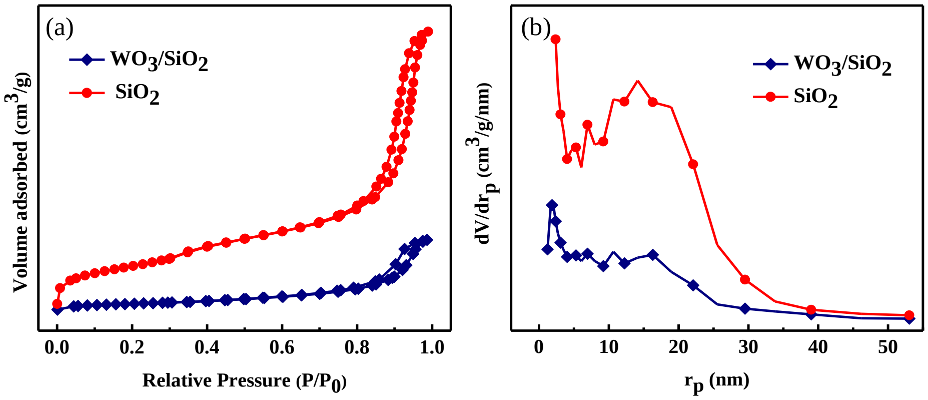

Fig. 2.1. (a) N_2 adsorption-desorption isotherms and **(b)** BJH plot for pore size distribution in SiO_2 and WO_3/SiO_2 monolith.

Table 2.1. Surface area, pore volume and pore size of SiO_2 and WO_3/SiO_2 monoliths.

Sample	Surface area (m^2/g)	Total pore volume (cm^3/g)	Mesopore size (nm)	Micropore size (nm)
SiO_2 monolith	451	1.167	10.34	1.10
WO_3/SiO_2 monolith	82	0.301	14.71	0.70

From N_2 adsorption-desorption isotherms studies **(Fig. 2.1(a))**, type IV isotherm was obtained for the synthesized monolith which shows the presence of mesopores. The H1 hysteresis loop with sharp adsorption and desorption branches verifies the regularity of pore size and shape of the monoliths. The pore size distribution was deduced using the BJH method which confirmed the mesoporous nature of the monoliths **(Fig. 2.1(b))**. The BET method was followed to analyze surface area, mean pore diameter and mean pore volume. The calculated surface area for SiO_2 and WO_3/SiO_2 monolith was 451 and 82 m^2/g, respectively. It was observed that, the surface area and pore volume was reduced after transformation of SiO_2 monoliths into WO_3/SiO_2 monoliths whereas the mesopore size increased and micropore size decreased (**Table 2.1**).

2.3.2 XPS analysis

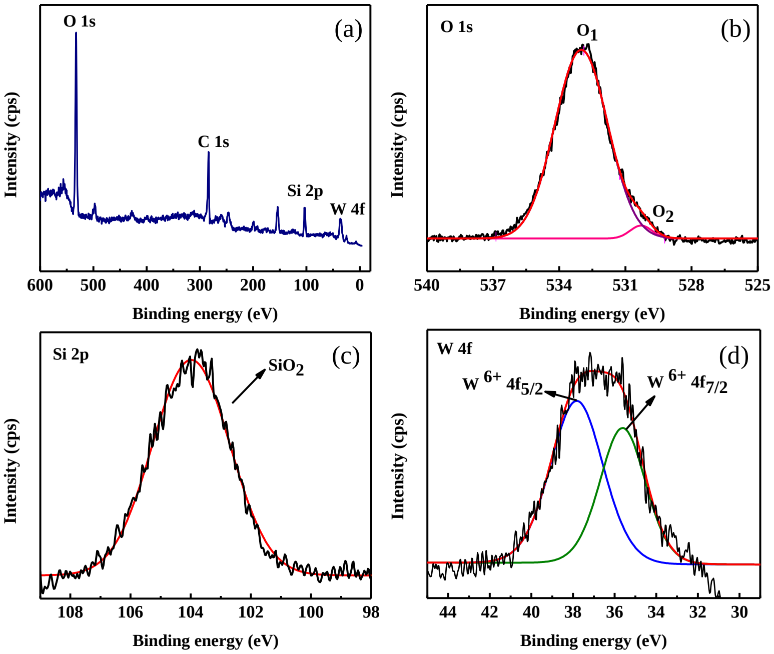

Fig. 2.2. XPS spectra of WO_3/SiO_2 monolith: **(a)** a typical survey spectrum, **(b)** O 1s, **(c)** Si 2p and **(d)** W 4f.

To investigate the oxidation states of the respective elements, the prepared catalyst was examined by XPS analysis. **Fig. 2.2(a)** depicts the survey XPS spectrum of WO_3/SiO_2 monoliths.

The peaks in the spectra reveal the presence of oxygen, silicon and tungsten. The C 1s peak appears because of the adventitious carbon from XPS instrument. The binding energies for constituent elements in the XPS analysis were obtained by referencing the C 1s signal at 284.5 eV. For fitting process of the peaks, de-convolution using least-squares Gaussian fit program for the peaks was followed. **Fig. 2.2(b)** shows the de-convoluted asymmetric peaks for O 1s having binding energies 532.9 eV (O_1) and 530.2 eV (O_2) corresponding to Si-O-Si and O^{2-} anions in WO_3, respectively.[31,32] The single de-convoluted peak for Si 2p with the binding energy 103.9 eV is shown in **Fig. 2.2(c)**, which demonstrates the existence of SiO_2.[33] **Fig. 2.2(d)** describes the de-convoluted asymmetric peaks for W 4f. The peaks corresponding to binding energies 37.8 eV and 35.5 eV are characteristic of W^{6+} $4f_{5/2}$ and $4f_{7/2}$.[34] These observations confirm the formation of WO_3/SiO_2.

2.3.3 X-ray diffraction studies

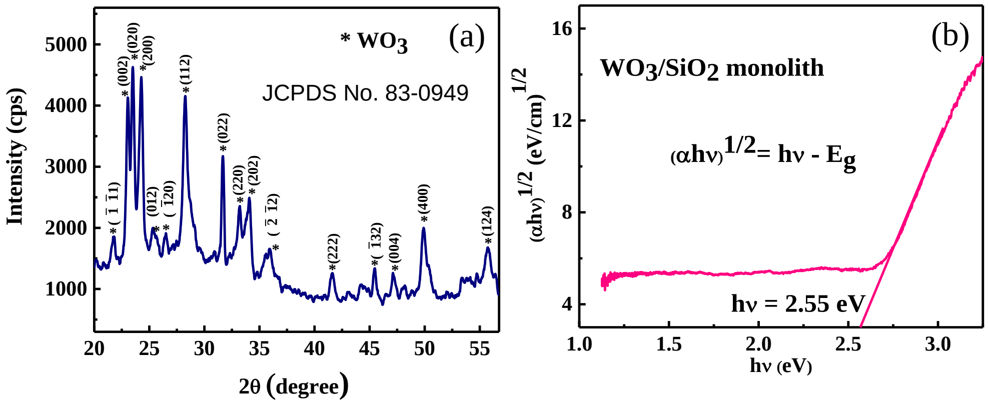

Fig. 2.3. (a) XRD pattern and **(b)** UV-Visible diffuse reflectance spectra of WO_3/SiO_2 monolith.

Fig. 2.3(a) shows the XRD pattern of WO_3/SiO_2 monolith. The diffraction peaks acquired at 23.07° (002), 23.49° (020), 24.31° (200), 28.28° (112), 31.93° (022), 33.18° (220), 34.08° (202), 49.92° (400) and 55.68° (124) can be attributed to crystalline WO_3 (JCPDS card No. 83-0949). The broadening centered at 22° can be ascribed to amorphous SiO_2, which verifies the formation of WO_3/SiO_2 monolith.

2.3.4 UV-visible diffuse reflectance spectroscopy

The UV-Visible diffuse reflectance spectroscopy (DRS) of WO_3/SiO_2 monolith was used to determine the band gap of the as-prepared catalyst. The band gap energy was obtained by the Tauc's plot obtained by following **Eq. (2.2)**.

$$(\alpha h\nu)^{1/2} = h\nu - E_g \tag{2.2}$$

where α, h, ν, and E_g are absorption coefficient, Planck constant, light frequency and band gap energy respectively. By the extrapolation of a tangent line intersecting with the X-axis, band gap value was determined **(Fig. 2.3b)**. The band gap energy of WO_3/SiO_2 monolith was 2.55 eV which makes it visible light active.

2.3.5 FESEM-EDS analysis

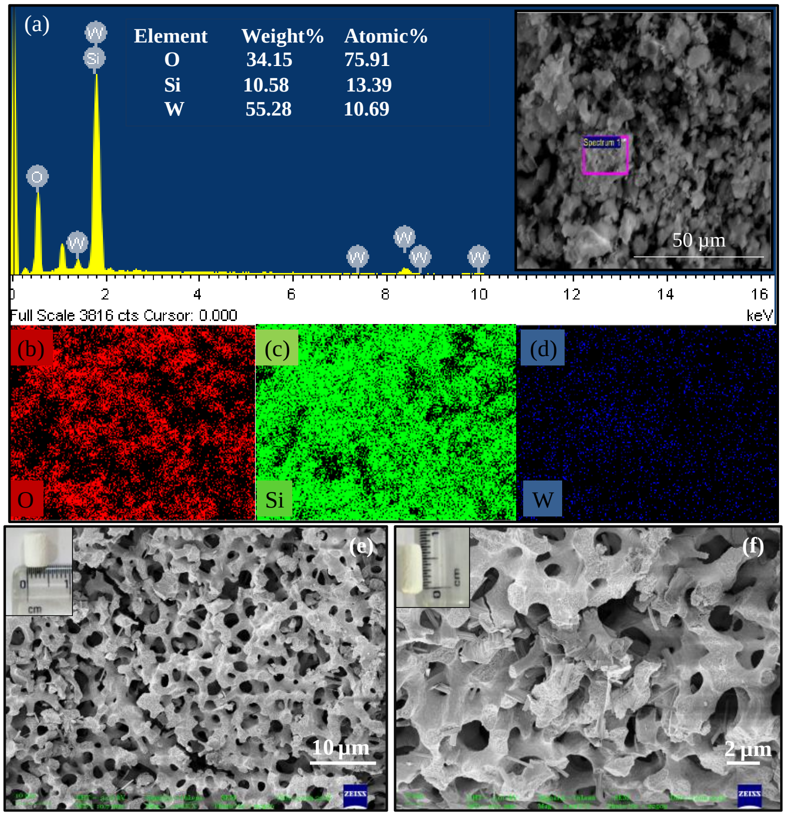

Element	Weight%	Atomic%
O	34.15	75.91
Si	10.58	13.39
W	55.28	10.69

Fig. 2.4. (a) EDS spectra with SEM micrograph, **(b-d)** elemental mapping and **(e-f)** FESEM images of WO_3/SiO_2 monolith at different magnification with the digital images in inset showing the length and diameter of monolith.

The EDS analysis was used to study the elemental composition of the as-prepared monolith which is shown in **Fig. 2.4(a)**. It can be seen that the elements are homogeneously distributed **(Fig. 2.4(b-d))** and a uniform dispersal of the precursor metal salt solution could be responsible for that. The surface morphology of the monoliths was analyzed by FESEM images. The FESEM images of WO_3/SiO_2 monolith are shown in **Fig. 2.4(e-f)** and the porous network structure can be seen clearly (fine mesopore/micropore structure are present within the walls of the macropores).

2.3.6 Photocatalytic degradation of MB

To investigate the photocatalytic performance of WO_3/SiO_2 monolith, two experiments were performed; (a) photolysis of cationic thiazine dye MB (without catalyst) and (b) photocatalytic degradation of MB (with catalyst). In photolysis experiment, about 5 ppm of MB solution was illuminated under visible light (without catalyst) for 120 min and in the photodegradation experiment, about 5 ppm MB solution with 0.1 g/L WO_3/SiO_2 monolith was stirred in dark for 30 min till adsorption-desorption equilibrium was attained and then it was exposed to visible light for 2 h until complete degradation was achieved.

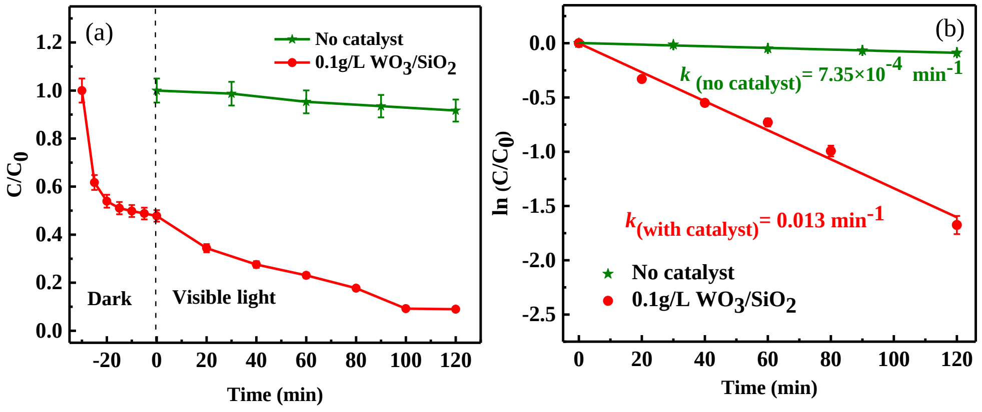

Fig. 2.5. (a-b) Kinetic analysis for the photodegradation of MB with and without catalyst.

To calculate the rate constant, **Eq. (2.3)** was followed, where, k is the rate constant, C_0 is the initial concentration i.e., concentration at time t = 0 and C is the concentration at any time t.

$$\ln (C/C_0) = -kt \qquad (2.3)$$

Fig. 2.5(a-b) shows the kinetic analysis for photolysis of MB with and without catalyst. It was observed that when no catalyst was used, the absorbance of the dye did not decrease to a great extent and only 10% photodegradation was there with a rate constant of 7.35×10^{-4} min^{-1}. The kinetic analysis for the photodegradation of MB using 0.1 g/L WO_3/ SiO_2 monolith revealed that MB was degraded with a rate constant of 0.013 min^{-1} and degradation efficiency ~91% at ambient temperature and natural pH (7.5) of MB. The results so obtained imply that the as-prepared catalyst has good photocatalytic efficiency in visible light.

Fig. 2.6 shows the effect of WO_3-precursor concentration on the photocatalytic activity of WO_3/SiO_2 monolith. It is evident from the plot that there is no significant change in degradation efficiency and it is almost constant when fixed amount of WO_3/SiO_2 monolith prepared by using 0.5 M, 1 M and 1.5 M WO_3-precursor is used.

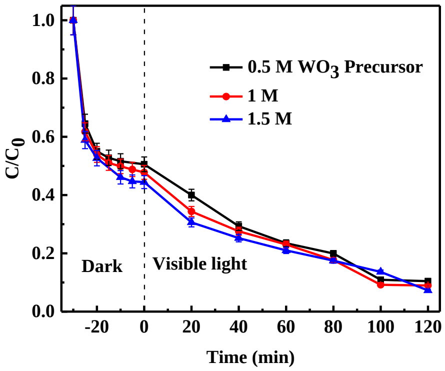

Fig. 2.6. Kinetic analysis for the photodegradation of MB using 0.1 g/L WO_3/SiO_2 prepared by using varying concentration of WO_3 precursor.

2.3.6.1 Effect of pH

The photodegradation of 5 ppm MB using 0.1 g/L WO_3/SiO_2 was carried out at different pH conditions (pH=1, 3, 5, 7.5, 9, 10 and 11). The pH values for the dye solution were maintained by adding either NaOH or HCl accordingly. The reported isoelectric point (IEP) for WO_3 is 0.2−1 and that for SiO_2 is 2.0.[21] Mixed oxides usually show IEP values that are intermediate to those of the corresponding pure monometallic oxides. As shown in **Fig. 2.7(a)**, in highly acidic condition (pH~1), the degradation efficiency was lowest. This could be as a consequence of excessive H^+ ions present on the catalyst surface leading to surface saturation. Further, at this pH the predominant surface species is M-OH_2^+ (M = metal) which repels the cationic dye and thus minimum interaction between the catalyst and dye occurs. The pH values higher than the intermediate IEP (0.2-2) are favorable for adsorption of cationic adsorbate MB, as in this situation the predominant surface species is M-O^-.[35]

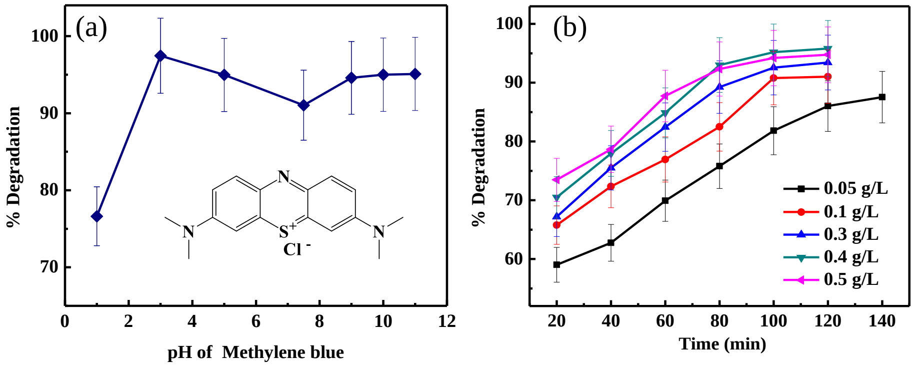

Fig. 2.7. (a) Effect of pH and **(b)** effect of concentration of monolith on photodegradation of MB.

It was observed that the best degradation (97.5%) occurs at pH~3. Further, at neutral pH range, the efficiency falls considerably possibly because; the formation of reactive species is not facilitated.[36] However, as we move to basic conditions there is a little rise in the efficiency as the surface of catalyst is negatively charged and it favors the adsorption ultimately degradation of cationic dye. But at higher alkaline pH, the metal oxide begins to dissolute which leads to destroy the monolithic structure and block the active sites[35] and as a result, degradation efficiency increases in a negligible amount. Nevertheless, the degradation efficiency was still above 90% at natural pH (7.5) of MB and the kinetic study was carried out at this pH to avoid any harsh acidic/basic condition.

2.3.6.2 Effect of concentration of catalyst

Various tests were performed to study the effect of concentration of the catalyst (0.05-0.5 g/L) on photocatalytic degradation of MB. **Fig. 2.7(b)** shows the graph regarding the concentration study from which it was inferred that with an increase in the photocatalyst concentration from 0.05 g/L to 0.4 g/L, the degradation efficiency increases (~96% at 0.4 g/L) but on further increase in the concentration to 0.5 g/L almost saturation occurs. This happens due to rise in the opaqueness of the solution and scattering of light. Complete adsorption of dye occurs on the catalyst surface and further incorporation of catalyst has no effect on the degradation as the active sites get deactivated.

2.3.6.3 Reusability

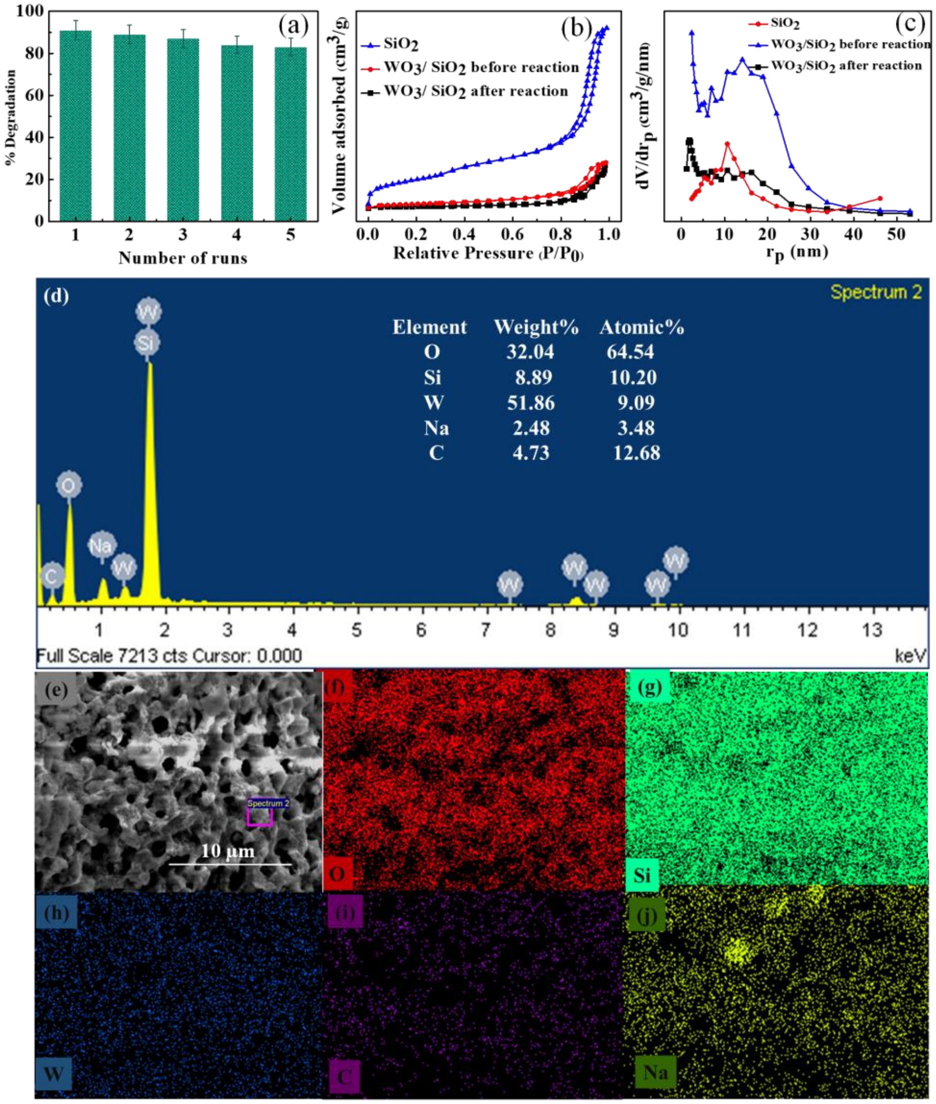

Element	Weight%	Atomic%
O	32.04	64.54
Si	8.89	10.20
W	51.86	9.09
Na	2.48	3.48
C	4.73	12.68

Fig. 2.8. (a) Reusability experiments, **(b-j)** characterization after photocatalytic experiment; **(b)** N_2 sorption isotherm, **(c)** BJH plot, **(d)** EDS spectra, **(e)** SEM micrograph, and **(f-j)** elemental mapping images.

Due to the hard rock like structure and large size (0.7 cm long and 0.5 cm in diameter), the monolithic catalyst is easily separable from the solution and it was regenerated by washing with dilute NaOH followed by drying at 40ºC. The reusability of the synthesized monoliths was tested for 5 cycles in the degradation of MB for 120-min by irradiation in visible light. It was noted that the degradation efficiency decreases but was still about 80% even after 5 consecutive runs. The photocatalytic efficiency decreases by ~11% as shown in **Fig. 2.8(a)**. This is justified by characterization results after the photocatalytic reaction **(Fig. 2.8(b-j))**. The surface morphology and surface area of WO_3/SiO_2 monolith is intact and not much disrupted after the photocatalytic reaction, which was confirmed from BET N_2 adsorption/desorption studies **Fig. 2.8(b-c)** and EDS with elemental mapping images **Fig. 2.8(e-j)**. The surface area for WO_3/SiO_2 monolith was 82 and 67 m^2/g while the pore volume was 0.301 and 0.270 before and after the reaction, respectively. The composition of major elements is not disturbed much after the reaction although minor peaks corresponding to Na and C are observed. The peak for Na observed may be due to the washing of the catalyst with NaOH and that of C may be either due to the remaining dye traces or the carbon tape used in sample holder in EDS analysis.

2.3.6.4 Plausible mechanism

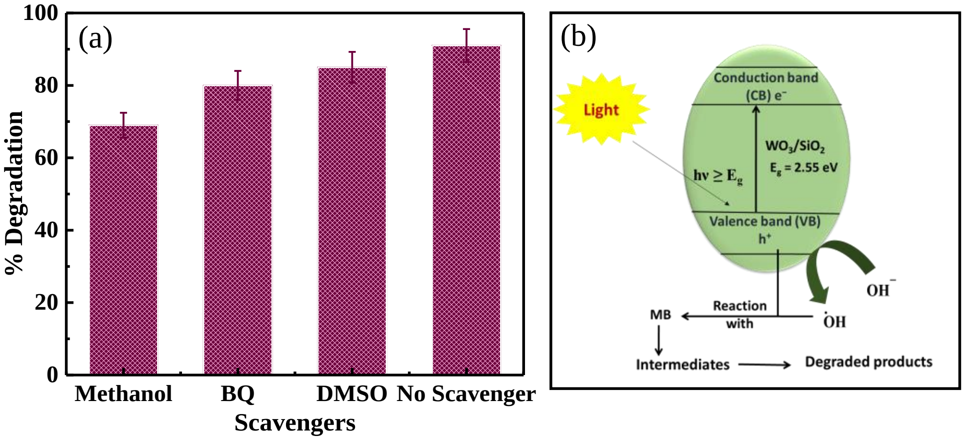

Fig. 2.9. (a) Effect of scavengers on the photocatalytic degradation of MB and **(b)** schematic representation for the mechanism of photodegradation of MB by WO_3/SiO_2 monolith.

To know the role of photogenerated radical species in degradation process and photocatalytic mechanism of MB by as-prepared monolith under visible light illumination, trapping experiment was conducted by adding different scavengers like methanol, benzoquinone (BQ) and DMSO for quenching holes (h^+), superoxide radicals ($O_2^{\bullet-}$) and hydroxyl radicals ($^{\bullet}OH$), respectively **(Fig. 2.9a)**. It is evident from this experiment that the photocatalytic degradation of MB by WO_3/SiO_2 monolith was affected significantly by the addition of methanol, suggesting that h^+ could be the major species in the degradation reaction.

WO_3/SiO_2 monolith absorbs visible light photon to excite valence band electron (e^-) to conduction band and generate hole (h^+) in valence band. The CB potential of WO_3 (~ +0.74V) is more positive than the potential for the single-electron reduction of oxygen (~ −0.28V), and thus superoxide anion radicals can't be formed. However, the VB potential of WO_3 (~ +3.44V) is suitable for the formation of hydroxyl radicals by the oxidation of water (~ +1.23V) by the photogenerated holes.[9] The photodegradation process is caused by these reactive species **(Fig. 2.9b).** The chemical reaction involved in the mechanism are displayed in **Eq. (2.4)** to **Eq. (2.8).**

$$WO_3 + h\nu \rightarrow e^- + h^+ \quad (2.4)$$

$$H_2O + h^+ \rightarrow H_2O^+ \rightarrow {}^{\bullet}OH + H^+ \quad (2.5)$$

$$H_2O \rightarrow {}^{-}OH + H^+ \quad (2.6)$$

$${}^{-}OH + h^+ \rightarrow {}^{\bullet}OH \quad (2.7)$$

$${}^{\bullet}OH/\, h^+ \rightarrow \text{intermediates} \rightarrow \text{degraded products} \quad (2.8)$$

2.3.6.5 Comparison with literature

A comparative study of photodegradation of MB with different photocatalysts accounted in the literature is presented in **Table 2.2.** From the comparison table, it can be derived that even a very small amount of WO_3/SiO_2 monolith can degrade hazardous pollutants under visible light irradiation very effectively even at natural pH of dye and ambient temperature and pressure conditions and can therefore be employed as an alternative photocatalyst for the purpose of wastewater treatment.

Table 2.2. Comparison of different photocatalysts for degradation of MB.

Catalyst	MB conc. (ppm)	Catalyst conc. (g/L)	Time	Light source	Light intensity	Degradation efficiency (%)	Rate constant *k* (min^{-1})	Ref.
(1:4) ZnS:CdS	10	0.1	6 h	Visible light (500 W halogen lamp)	-	73	0.0036	[37]
Hematite (α-Fe_2O_3)	20	2.5	8.3 h	Sunlight	-	97	0.0046	[38]
WO_3/ TiO_2	10	0.5	120 min	Visible light (Philips PL-S 9W/865/2P	-	27	0.00197	[39]
WO_3/ TiO_2	10	0.5	120 min	UV light (Philips PL-S 9W/10/2P)	-	90	0.0180	[39]
$BiVO_4$/EDTA	5	1	5 h	Sunlight (500 Xe arc lamp)	-	91	0.0078	[40]
(Yb, N)- TiO_2	10	3	5 h	Visible light (30W fluorescent lamp)	-	94	0.0091	[41]
TiO_2/ Polyaniline	10	2.5	200 min	UV light	-	73	0.0068	[42]
WO_3/SiO_2	5	0.1	120 min	Visible light	125 W/m^2	91	0.013	This study

2.3.6.6 GC-MS analysis of MB-degradation

For the identification of intermediates and products in the photodegradation reaction of MB, GC-MS analysis was carried out. The GC chromatogram and mass spectrum of MB after treatment are shown in **Fig. 2.10 (a)** and **(b)**, respectively. The proposed degradation pathway has been displayed in **Scheme 2.2.**

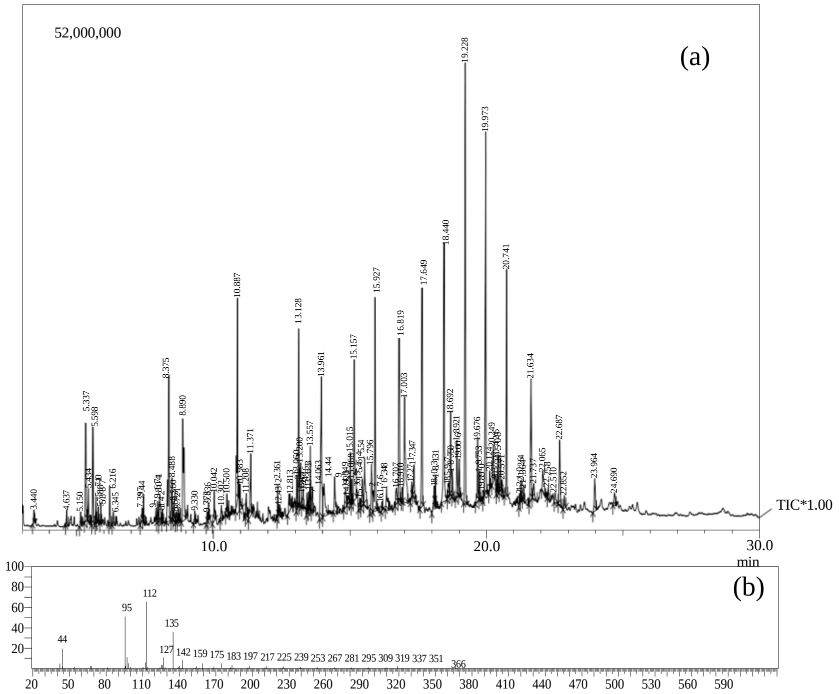

Fig. 2.10. (a) GC chromatogram of MB after photocatalytic degradation and **(b)** MS spectra of MB after photodegradation at retention time of 19.228 min.

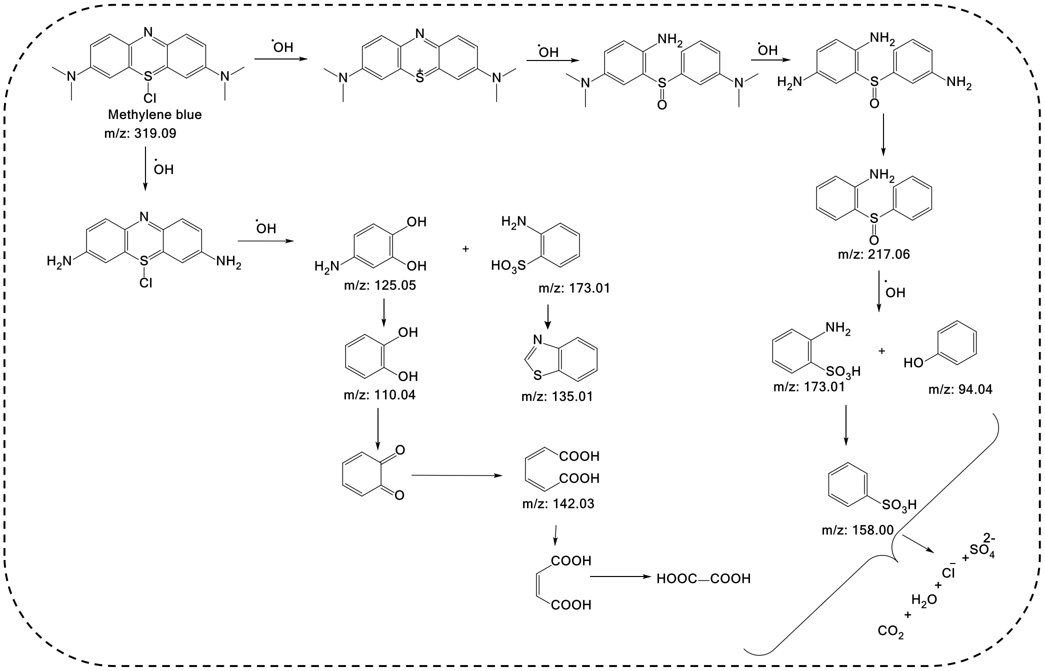

Scheme 2.2. Possible degradation pathway of MB by WO_3/SiO_2 monoliths.

MB is decomposed by the attack of hydroxyl radical and the breakage of N-CH_3 to form 2-(phenylsulfinyl)aniline (m/z=217) [M+]+ which is further oxidized to form aniline-2-sulfonic acid (m/z=173) [M+2]+ and phenol (m/z=94) [M+H]+. The former further may undergo N-C bond cleavage to form benzenesulfonic acid (m/z=158) [M+H]+. On the other hand, the ring formation leads to benzothiazole (m/z=135.01) [M+]+. The oxidation of MB to 4-aminobenzene-1,2-diol (m/z=110.04) [M+]+ and further N-C bond cleavage and ring destruction could produce nontoxic organic acid viz., hexa-2,4-dienedioic acid (m/z=142) [M+]+. These organic intermediates were oxidized until finally transformed into CO_2, H_2O, Cl^-, SO_4^{2-}, and NO_3^-. The findings were in accordance with the literature reports.[43]

2.3.7 Photocatalytic degradation of Imidacloprid (IC)

Direct and indirect photocatalysis were distinguished by performing the photodegradation of colorless pollutant IC using WO_3/SiO_2 monolith. About 10 mL aqueous solution of IC with 0.5 g/L photocatalyst was stirred in dark for 20 min to establish adsorption-desorption equilibrium and subsequently illuminated under visible light for 60 min. A degradation efficiency of 59% was achieved with a rate constant of 0.011 min^{-1} as shown in **Fig. 2.11(a-b)**. It clearly shows that WO_3/SiO_2 monolith can also efficiently degrade colorless pollutants

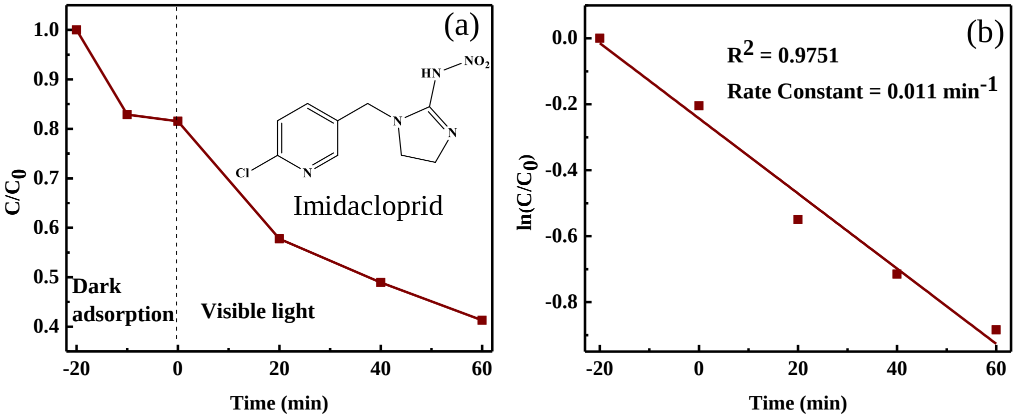

Fig. 2.11. (a-b) Kinetic analysis for the photodegradation of transparent insecticide IC using WO_3/SiO_2 monolith under visible light irradiation.

2.3.7.1 GC-MS analysis of IC-degradation

The GC chromatogram and mass spectrum of IC after treatment are shown in **Fig. 2.12 (a)** and **Fig. 2.12 (b)**, respectively. The proposed degradation pathway has been displayed in **Scheme 2.3**.

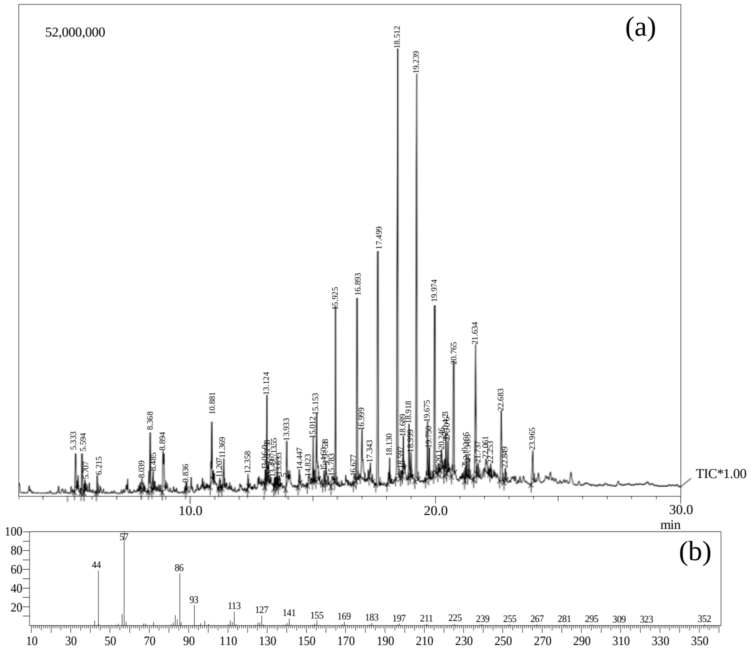

Fig. 2.12. (a) GC chromatogram of IC after photocatalytic degradation and **(b)** MS spectra of IC after photodegradation at retention time of 18.512 min.

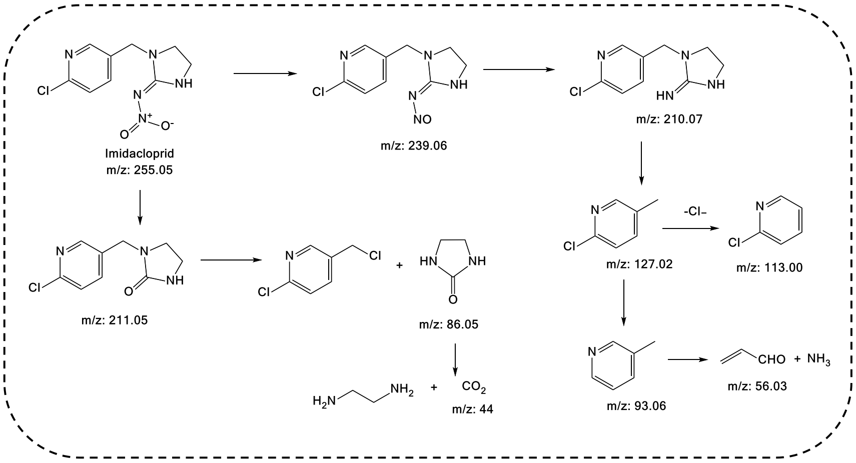

Scheme 2.3. Possible degradation pathway of IC by WO_3/SiO_2 monoliths.

In the first pathway, IC may be degraded to N-(1-((6-chloropyridin-3-yl)methyl)imidazolidin-2-ylidene)nitrous amide (m/z=239.06) [M+]+ and further into 1-((6-chloropyridin-3-yl)methyl)imidazolidin-2-imine (m/z=210.07) [M+H]+. Then, the N-C bond cleavage could form 2-chloro-5-methylpyridine (m/z=127.02) [M+]+ and it could either undergo demethylation to produce 2-chloropyridine (m/z=113.02) [M+]+ or it could undergo dechlorination to form 3-methylpyridine (m/z=93.02) [M+]+ which on dehydration yields acrolein (m/z=56.03) [M+H]+ and ammonia. In the second pathway, IC could degrade into 1-((6-chloropyridin-3-yl)methyl)imidazolidin-2-one (m/z=211.05) [M+]+ which could be further degraded via the cleavage of C-N bond to yield imidazolidin-2-one (m/z=86.05) [M+]+ and then might degrade to CO_2 (m/z=44) [M+]+. The findings were in accordance with the literature reports.[44]

2.4 Conclusions

Hierarchical porous silica supported metal-oxide (WO_3/SiO_2) monoliths were fabricated by wet impregnation method. The characterization of the sample was done using BET N_2 adsorption-desorption studies, FESEM, EDS, DRS, XRD and XPS analyses. The results of these analyses revealed that WO_3 is well formed and uniformly dispersed on SiO_2 surface and the formation of a highly porous and connected network structure was confirmed. The photodegradation of MB was observed by UV–visible spectrophotometer and the results obtained showed good photocatalytic activity for degradation of MB under visible light illumination. The supreme photocatalytic efficiency of the photocatalyst could be accredited to its high surface area. Different studies were performed to explore the effect of pH and concentration as well as reusability of the catalyst. The supreme reusability efficiency was validated from the characterization results of the monolith after 2 cycles of photodegradation. To know the role of reactive species in the mechanism, trapping experiments were conducted revealing that holes were majorly accountable for the degradation. The results obtained for photodegradation of IC proved that the synthesized photocatalyst is suitable for the degradation of both colored as well as colorless pollutants. The degraded products have also been analyzed through GC-MS studies. The future direction of this work is that WO_3/SiO_2 monoliths can be used at an industrial scale for the waste water treatment as expensive separation techniques are not required. This advocated that the monoliths are an excellent choice for photodegradation of toxic moieties owing to their easy-separation from the post photocatalytic reaction mixture along with cost-friendliness and simple nature.

References

(1) Varjani, S.; Rakholiya, P.; Ng, H. Y.; You, S.; Teixeira, J. A. Microbial Degradation of Dyes: An Overview. *Bioresour. Technol.* **2020**, *314,* 123728. https://doi.org/10.1016/j.biortech.2020.123728.

(2) Paraschiv, D.; Tudor, C.; Petrariu, R. The Textile Industry and Sustainable Development: A Holt-Winters Forecasting Investigation for the Eastern European Area. *Sustain.* **2015**, *7* (2), 1280–1291. https://doi.org/10.3390/su7021280.

(3) Akhtar, M. F.; Ashraf, M.; Javeed, A.; Anjum, A. A.; Sharif, A.; Saleem, M.; Mustafa, G.; Ashraf, M.; Saleem, A.; Akhtar, B. Association of Textile Industry Effluent with Mutagenicity and Its Toxic Health Implications upon Acute and Sub-Chronic Exposure. *Environ. Monit. Assess.* **2018**, *190* (3), 179. https://doi.org/10.1007/s10661-018-6569-7.

(4) Jiang, J.; Wang, H.; Chen, X.; Li, S.; Xie, T.; Wang, D.; Lin, Y. Enhanced Photocatalytic Degradation of Phenol and Photogenerated Charges Transfer Property over BiOI-Loaded ZnO Composites. *J. Colloid Interface Sci.* **2017**, *494*, 130–138. https://doi.org/10.1016/j.jcis.2017.01.064.

(5) Zhao, J.; Lu, Z.; He, X.; Zhang, X.; Li, Q.; Xia, T.; Zhang, W.; Lu, C. Fabrication and Characterization of Highly Porous $Fe(OH)_3$ @Cellulose Hybrid Fibers for Effective Removal of Congo Red from Contaminated Water. *ACS Sustain. Chem. Eng.* **2017**, *5* (9), 7723–7732. https://doi.org/10.1021/acssuschemeng.7b01175.

(6) Dong, S.; Feng, J.; Fan, M.; Pi, Y.; Hu, L.; Han, X.; Liu, M.; Sun, J.; Sun, J. Recent Developments in Heterogeneous Photocatalytic Water Treatment Using Visible Light-Responsive Photocatalysts: A Review. *RSC Adv.* **2015**, *5* (19), 14610–14630. https://doi.org/10.1039/c4ra13734e.

(7) Kim, Y.; Joo, H.; Her, N.; Yoon, Y.; Sohn, J.; Kim, S.; Yoon, J. Simultaneously

Photocatalytic Treatment of Hexavalent Chromium (Cr(VI)) and Endocrine Disrupting Compounds (EDCs) Using Rotating Reactor under Solar Irradiation. *J. Hazard. Mater.* **2015**, *288*, 124–133. https://doi.org/10.1016/j.jhazmat.2015.02.021.

(8) Kumar, S.; Karthikeyan, S.; Lee, A. G-C_3N_4-Based Nanomaterials for Visible Light-Driven Photocatalysis. *Catalysts* **2018**, *8* (2), 74. https://doi.org/10.3390/catal8020074.

(9) Aslam, M.; Ismail, I. M. I.; Chandrasekaran, S.; Hameed, A. Morphology Controlled Bulk Synthesis of Disc-Shaped WO_3 Powder and Evaluation of Its Photocatalytic Activity for the Degradation of Phenols. *J. Hazard. Mater.* **2014**, *276*, 120–128. https://doi.org/10.1016/j.jhazmat.2014.05.022.

(10) Li, X.; Yu, J.; Jaroniec, M. Hierarchical Photocatalysts. *Chem. Soc. Rev.* **2016**, *45*, 2603–2636. https://doi.org/10.1039/c5cs00838g.

(11) Song, H.; Li, Y.; Lou, Z.; Xiao, M.; Hu, L.; Ye, Z.; Zhu, L. Synthesis of Fe-Doped WO_3 Nanostructures with High Visible-Light-Driven Photocatalytic Activities. *Appl. Catal. B Environ.* **2015**, *166–167*, 112–120. https://doi.org/10.1016/j.apcatb.2014.11.020.

(12) Dong, P.; Yang, B.; Liu, C.; Xu, F.; Xi, X.; Hou, G.; Shao, R. Highly Enhanced Photocatalytic Activity of WO_3 Thin Films Loaded with Pt-Ag Bimetallic Alloy Nanoparticles. *RSC Adv.* **2017**, *7* (2), 947–956. https://doi.org/10.1039/c6ra25272a.

(13) Dong, P.; Hou, G.; Xi, X.; Shao, R.; Dong, F. WO_3-Based Photocatalysts: Morphology Control, Activity Enhancement and Multifunctional Applications. *Environ. Sci. Nano* **2017**, *4* (3), 539–557. https://doi.org/10.1039/c6en00478d.

(14) Song, X. C.; Zheng, Y. F.; Yang, E.; Wang, Y. Large-Scale Hydrothermal Synthesis of WO3 Nanowires in the Presence of K_2SO_4. *Mater. Lett.* **2007**, *61* (18), 3904–3908. https://doi.org/10.1016/j.matlet.2006.12.055.

(15) Satishkumar, B. C.; Govindaraj, A.; Nath, M.; Rao, C. N. R. Synthesis of Metal Oxide Nanorods Using Carbon Nanotubes as Templates. *J. Mater. Chem.* **2000**, *10* (9), 2115–2119. https://doi.org/10.1039/b002868l.

(16) Baeck, S. H.; Choi, K. S.; Jaramillo, T. F.; Stucky, G. D.; McFarland, E. W. Enhancement of Photocatalytic and Electrochromic Properties of Electrochemically Fabricated

Mesoporous WO_3 Thin Films. *Adv. Mater.* **2003**, *15* (15), 1269–1273. https://doi.org/10.1002/adma.200304669.

(17) Badilescu, S.; Ashrit, P. V. Study of Sol-Gel Prepared Nanostructured WO_3 Thin Films and Composites for Electrochromic Applications. *Solid State Ionics* **2003**, *158* (1–2), 187–197. https://doi.org/10.1016/S0167-2738(02)00764-6.

(18) Smått, J. H.; Weidenthaler, C.; Rosenholm, J. B.; Lindén, M. Hierarchically Porous Metal Oxide Monoliths Prepared by the Nanocasting Route. *Chem. Mater.* **2006**, *18* (6), 1443–1450. https://doi.org/10.1021/cm051880p.

(19) Sharma, M.; Hazra, S.; Basu, S. Kinetic and Isotherm Studies on Adsorption of Toxic Pollutants Using Porous $ZnO@SiO_2$ Monolith. *J. Colloid Interface Sci.* **2017**, *504*, 669–679. https://doi.org/10.1016/j.jcis.2017.06.020.

(20) Smått, J. H.; Schunk, S.; Lindén, M. Versatile Double-Templating Synthesis Route to Silica Monoliths Exhibiting a Multimodal Hierarchical Porosity. *Chem. Mater.* **2003**, *15* (12), 2354–2361. https://doi.org/10.1021/cm0213422.

(21) Depuccio, D. P.; Botella, P.; O’Rourke, B.; Landry, C. C. Degradation of Methylene Blue Using Porous WO_3, SiO_2-WO_3, and Their Au-Loaded Analogs: Adsorption and Photocatalytic Studies. *ACS Appl. Mater. Interfaces* **2015**, *7* (3), 1987–1996. https://doi.org/10.1021/am507806a.

(22) Sharma, K.; Vyas, R. K.; Dalai, A. K. Thermodynamic and Kinetic Studies of Methylene Blue Degradation Using Reactive Adsorption and Its Comparison with Adsorption. *J. Chem. Eng. Data* **2017**, *62* (11), 3651–3662. https://doi.org/10.1021/acs.jced.7b00379.

(23) Vutskits, L.; Briner, A.; Klauser, P.; Gascon, E.; Dayer, A. G.; Kiss, J. Z.; Muller, D.; Licker, M. J.; Morel, D. R. Adverse Effects of Methylene Blue on the Central Nervous System. *Anesthesiology* **2008**, *108* (4), 684–692. https://doi.org/10.1097/ALN.0b013e3181684be4.

(24) Pathania, D.; Sharma, S.; Singh, P. Removal of Methylene Blue by Adsorption onto Activated Carbon Developed from Ficus Carica Bast. *Arab. J. Chem.* **2017**, *10*, S1445–S1451. https://doi.org/10.1016/j.arabjc.2013.04.021.

(25) Mishra, A.; Mehta, A.; Sharma, M.; Basu, S. Enhanced Heterogeneous Photodegradation of VOC and Dye Using Microwave Synthesized TiO_2/Clay Nanocomposites: A Comparison Study of Different Type of Clays. *J. Alloys Compd.* **2017**, *694*, 574–580. https://doi.org/10.1016/j.jallcom.2016.10.036.

(26) Azimirad, R.; Safa, S. Preparation of Three Dimensional Graphene Foam-WO_3 Nanocomposite with Enhanced Visible Light Photocatalytic Activity. *Mater. Chem. Phys.* **2015**, *162*, 686–691. https://doi.org/10.1016/j.matchemphys.2015.06.043.

(27) Dinari, M.; Momeni, M. M.; Ahangarpour, M. Efficient Degradation of Methylene Blue Dye over Tungsten Trioxide/Multi-Walled Carbon Nanotube System as a Novel Photocatalyst. *Appl. Phys. A Mater. Sci. Process.* **2016**, *122* (10), 1–9. https://doi.org/10.1007/s00339-016-0403-2.

(28) Prabhu, S.; Manikumar, S.; Cindrella, L.; Kwon, O. J. Charge Transfer and Intrinsic Electronic Properties of RGO-WO_3 Nanostructures for Efficient Photoelectrochemical and Photocatalytic Applications. *Mater. Sci. Semicond. Process.* **2018**, *74* (October 2017), 136–146. https://doi.org/10.1016/j.mssp.2017.10.041.

(29) Liu, X.; Wu, X.; Long, Z.; Zhang, C.; Ma, Y.; Hao, X.; Zhang, H.; Pan, C. Photodegradation of Imidacloprid in Aqueous Solution by the Metal-Free Catalyst Graphitic Carbon Nitride Using an Energy-Saving Lamp. *J. Agric. Food Chem.* **2015**. https://doi.org/10.1021/acs.jafc.5b01105.

(30) Sharma, M.; Choudhury, D.; Hazra, S.; Basu, S. Effective Removal of Metal Ions from Aqueous Solution by Mesoporous MnO_2 and TiO_2 Monoliths: Kinetic and Equilibrium Modelling. *J. Alloys Compd.* **2017**, *720*, 221–229. https://doi.org/10.1016/j.jallcom.2017.05.260.

(31) Liu, Y.; Feng, P.; Wang, Z.; Jiao, X.; Akhtar, F. Novel Fabrication and Enhanced Photocatalytic MB Degradation of Hierarchical Porous Monoliths of MoO_3 Nanoplates. *Sci. Rep.* **2017**, *7* (1), 1845. https://doi.org/10.1038/s41598-017-02025-3.

(32) Thummavichai, K.; Wang, N.; Xu, F.; Rance, G.; Xia, Y.; Zhu, Y. In Situ Investigations of the Phase Change Behaviour of Tungsten Oxide Nanostructures. *R. Soc. Open Sci.*

2018, *5* (4), 171932. https://doi.org/10.1098/rsos.171932.

(33) Sri Devi Kumari, T.; Jeyakumar, D.; Prem Kumar, T. Nano Silicon Carbide: A New Lithium-Insertion Anode Material on the Horizon. *RSC Adv.* **2013**, *3* (35), 15028–15034. https://doi.org/10.1039/c3ra40798e.

(34) Mohamed, M. M.; Ahmed, S. A.; Khairou, K. S. Unprecedented High Photocatalytic Activity of Nanocrystalline WO_3/$NiWO_4$ Hetero-Junction towards Dye Degradation: Effect of Template and Synthesis Conditions. *Appl. Catal. B Environ.* **2014**, *150–151*, 63–73. https://doi.org/10.1016/j.apcatb.2013.12.001.

(35) Sharma, M.; Singh, J.; Basu, S. Efficient Metal Ion Adsorption and Photodegradation of Rhodamine-B by Hierarchical Porous Fe-Ni@SiO_2 Monolith. *Microchem. J.* **2019**, *145* (November 2018), 708–717. https://doi.org/10.1016/j.microc.2018.11.042.

(36) Gajbhiye, S. B. Photocatalytic Degradation Study of Methylene Blue Solutions and Its Application to Dye Industry Effluent. *Int. J. Mod. Eng. Res.* **2012**, *2* (3), 1204–1208.

(37) Soltani, N.; Saion, E.; Hussein, M. Z.; Erfani, M.; Abedini, A. Visible Light-Induced Degradation of Methylene Blue in the Presence of Photocatalytic ZnS and CdS Nanoparticles. *Int. J. Mol. Sci.* **2012**, *4*, 12242–12258. https://doi.org/10.3390/ijms131012242.

(38) Tan, W. F.; Yu, Y. T.; Wang, M. X.; Liu, F.; Koopal, L. K. Shape Evolution Synthesis of Monodisperse Spherical, Ellipsoidal, and Elongated Hematite (α-Fe_2O_3) Nanoparticles Using Ascorbic Acid. *Cryst. Growth Des.* **2014**, *14* (1), 157–164. https://doi.org/10.1021/cg401334d.

(39) Yang, L.; Si, Z.; Weng, D.; Yao, Y. Synthesis, Characterization and Photocatalytic Activity of Porous WO_3/TiO_2 Hollow Microspheres. *Appl. Surf. Sci.* **2014**, *313*, 470–478. https://doi.org/10.1016/j.apsusc.2014.05.230.

(40) Ma, W.; Li, Z.; Liu, W. Hydrothermal Preparation of $BiVO_4$ Photocatalyst with Perforated Hollow Morphology and Its Performance on Methylene Blue Degradation. *Ceram. Int.* **2015**, *41* (3), 4340–4347. https://doi.org/10.1016/j.ceramint.2014.11.123.

(41) Zhang, J.; Xu, L. J.; Zhu, Z. Q.; Liu, Q. J. Synthesis and Properties of (Yb, N)-TiO_2

Photocatalyst for Degradation of Methylene Blue (MB) under Visible Light Irradiation. *Mater. Res. Bull.* **2015**, *70*, 358–364. https://doi.org/10.1016/j.materresbull.2015.04.060.

(42) Reddy, K. R.; Karthik, K. V; Prasad, S. B. B.; Soni, S. K.; Jeong, H. M.; Raghu, A. V. Enhanced Photocatalytic Activity of Nanostructured Titanium Dioxide/Polyaniline Hybrid Photocatalysts. *Polyhedron* **2016**, *120*, 169–174. https://doi.org/10.1016/j.poly.2016.08.029.

(43) Wang, Q.; Tian, S.; Ning, P. Degradation Mechanism of Methylene Blue in a Heterogeneous Fenton-like Reaction Catalyzed by Ferrocene. *Ind. Eng. Chem. Res.* **2014**, *53* (2), 643–649. https://doi.org/10.1021/ie403402q.

(44) Garg, R.; Gupta, R.; Bansal, A. Photocatalytic Degradation of Imidacloprid Using Semiconductor Hybrid Nano-Catalyst: Kinetics, Surface Reactions and Degradation Pathways. *Int. J. Environ. Sci. Technol.* **2021**, *18* (6), 1425–1442. https://doi.org/10.1007/s13762-020-02866-y.

Chapter 3

Centimeter-sized Sb_2S_3/SiO_2 monoliths with 'mimosa pudica' flower-like morphology for photocatalytic detoxification of hazardous organic pollutants

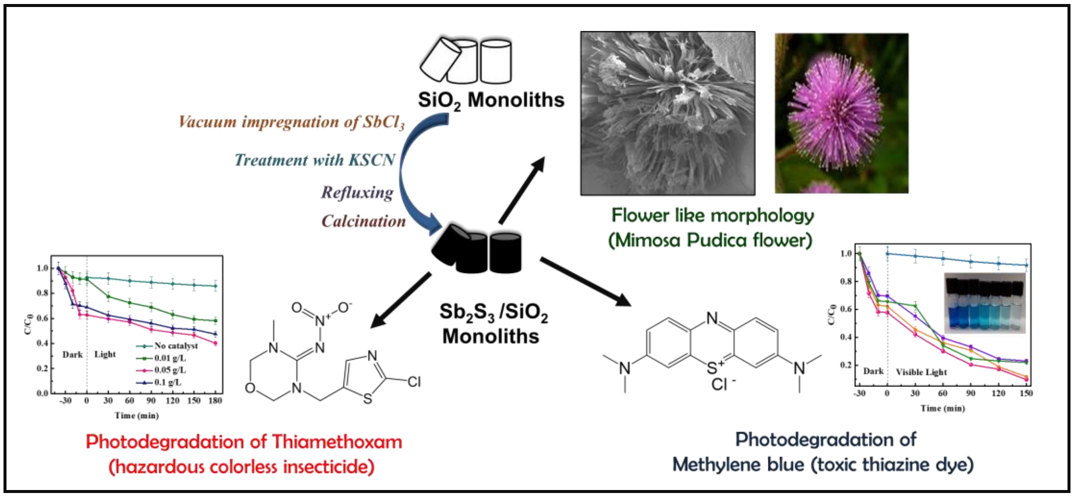

Highlights

- Sb_2S_3/SiO_2 monoliths with a 'mimosa pudica' flower-like morphology were fabricated which was active in almost entire visible range.
- The photocatalytic performance was tested for the degradation of MB dye and insecticide TM.
- Effects of various parameters on the degradation efficiency were investigated like pH, catalyst concentration, light source and illumination area.
- The monolithic material exhibited effective removal efficacy for MB (~96% and rate constant of 0.018 min^{-1}) and TM (~70% and rate constant of 0.0057 min^{-1}) at optimal conditions.

3.1. Introduction

As discussed in **Chapter 2**, photocatalytic degradation has the potential to make use of natural sunlight and tendency to completely eradicate toxic pollutants by converting them to CO_2 and H_2O after complete degradation.[1] In addition to MB, photocatalytic degradation of colorless insecticide thiamethoxam (TM) was carried out in this chapter. TM is the primary representative of 2nd generation neonicotinoids belonging to thia-nicotinyl sub-class.[2,3] It exhibits brilliant control of some significant pests in many crops. But it acts as a water pollutant due to some of its features like low soil sorption as well as high leaching capacity.[2] Therefore, it is very important to work on the fabrication of effective photocatalysts for the removal of these fatal pollutants to protect flora and fauna.

One such category of emerging visible-light active photocatalysts is chalcogenide-based compounds like Bi_2S_3, Sb_2S_3, etc.[4] Sb_2S_3 is an appropriate choice for photocatalysis because of its small gap covering the maximum span of the solar spectrum ranging from the visible region to near IR region.[5] It is a V–VI semiconductor and exhibits outstanding light absorbing capability accrediting to high optical absorption coefficient ($\alpha \sim 10^5$ cm^{-1}). The valence band and conduction band positions of Sb_2S_3 are ~1.3 and −0.44 eV.[6,7] Furthermore, Sb^{3+} and S^{2-} are borderline acid and soft base, respectively (elemental S is a borderline base). This fact increases the likelihood of anchoring as well as interaction with organic pollutants.[7] Sb_2S_3 has a chain-like layered morphology, high thermoelectric power, and exceptional photosensitive character. Accrediting these unique features, Sb_2S_3 has also found wide application in rechargeable Li/Na-ion batteries, microwave devices, solar cells and various thermoelectric and optoelectronic devices.[8] Combining Sb_2S_3 with SiO_2 can augment the overall photocatalytic activity of the material by forming heterojunction. The utilization of insulator oxide SiO_2 (having a large surface area) as a template increases the overall surface area of the composite and provides more number of active sites for better adsorption of the pollutants. The electrons at the surface states of SiO_2 have a likelihood to get excited from the VB under visible light illumination. This encourages the separation as well as the transfer of photogenerated charge carriers eventually lowering the recombination rate.[9] A high number of charge carriers on the surface of the catalyst enhances the likelihood of their reaction with pollutant leading to an escalation in the photocatalytic performance.[10]

However, it is evident from the literature that monolithic Sb_2S_3 has not been studied yet. The major benefit of hierarchical monoliths is that the large macropores in combination with the mesopore arrangement give them large transport channels.[11] The monolithic photocatalysts have increased light-harvesting ability due to more number of active sites leading to greater interaction time, better adsorption and eventually efficient degradation.[12]

Monolithic catalysts have been explored by many research groups for various applications. Almarzooqi et al.[13] proposed a novel way for the preparation of continuous, centimeter-sized, open-cell molybdenum disulfide hybrid monolith that was tested for the liquid adsorption of dibenzothiophene has been reported. Korala et al.[14] utilized CdS aerogels for degrading MB and methyl orange. Fleischmann et al.[15] synthesized mesoporous niobium disulfide/carbon monolithic hybrid having a gyroidal microstructure that was later utilized for electrochemical energy storage purpose.

This chapter recounts the synthesis of nanoflower-like Sb_2S_3/SiO_2 monoliths by the wet impregnation method, which were eventually utilized for the photocatalytic degradation of pollutants MB and TM. Various factors like effects of pH of MB and TM solutions, catalyst concentrations were investigated in conjunction with reusability studies and trapping experiments. The influence of the illumination area was also examined for MB degradation.

3.2 Experimental section

This section comprises of the chemicals, materials and the methodologies used for the synthesis of catalysts.

3.2.1 Chemicals and materials

Antimony trichloride ($SbCl_3$), potassium thiocyanate (KSCN), Thioacetamide, and tartaric acid were acquired from Loba Chemie, India. TiO_2 P25 was procured from Evonik Industries (Hanau, Germany). TM was purchased from Indogulf Cropsciences Ltd., India.

3.2.2 Syntheses

This section includes the synthesis methodologies of Sb_2S_3/SiO_2 monoliths and bulk Sb_2S_3 powder.

3.2.2.1 Synthesis of Sb_2S_3/SiO_2 monoliths

Firstly, the silica monoliths were synthesized as per the procedure described in **Chapter 2 (section 2.2.1)**. The as-synthesized SiO_2 monoliths were degassed for 6 h using a vacuum pump. A clear solution of antimony chloride was prepared by mixing 8.5 g of it in 4 M tartaric acid (used as a complexing agent). This solution was impregnated into the SiO_2 monoliths in vacuum followed by drying at 40 °C. The above-mentioned steps were performed thrice for best impregnation. Then, 1M KSCN was added to the monoliths and the mixture was refluxed for 24 h at 110 °C and dried at 40 °C. Finally, calcination at 250 °C for 2 h at 2 °C/min produced Sb_2S_3/SiO_2 monoliths. The synthesized monoliths were about 1 cm in length and 0.5 cm in diameter. **Scheme 3.1** depicts the actual images for the fabrication of prepared monoliths.

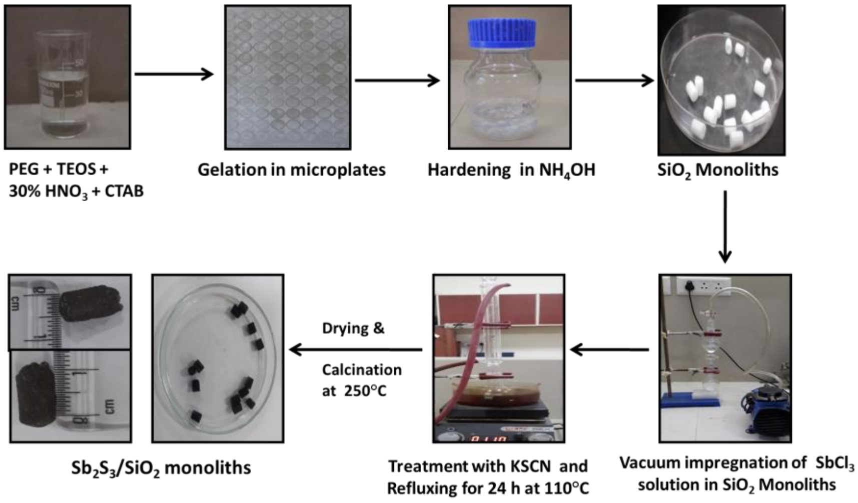

Scheme 3.1. Demonstrative depiction for the preparation of SiO_2 monoliths and nanoflower-like Sb_2S_3/SiO_2 monoliths.

3.2.2.2 Synthesis of bulk Sb_2S_3 powder

Bulk Sb_2S_3 powder was also synthesized by the following method as reported in the literature to compare its photoactivity with Sb_2S_3/SiO_2 monolith.[16] $SbCl_3$ (0.03 mol) was added to the solution of 0.05 mol of tartaric acid. Later, a solution of 2 mmol thioacetamide was added to the prepared blend. This solution was subsequently shifted to a sealed Teflon line stainless-steel autoclave and maintained the temperature at 160 °C for 12 h. The solution attained was cooled, centrifuged and finally washed with distilled water and ethanol several times and dried at 60 °C.

3.2.3 Characterization methods

X-ray diffraction analysis (XRD) was carried out by means of PANALYTICAL X'Pert PRO X-ray diffractometer with Cu Kα (λ=1.540 Å) radiation operated at 45 kV with the diffraction angle of 10-90 ^{o} and step size 0.026^{o}. The chemical bonding states of the as-prepared catalyst were investigated using PHI-5200 X-ray photon spectroscopy (XPS) system, using monochromatic source Al kα radiation at 1486.7 eV. The surface morphology of the monoliths was analyzed using ZEISS field emission scanning electron microscope (FESEM) operating at 5 kV accelerating voltage. Oxford INCTA energy dispersive spectrometer (EDS) was used to obtain EDS spectra and color mapping images. The surface area was determined using Microtrac Belsorp Mini-II (Bel, Japan, Inc) Brunauer–Emmett–Teller (BET) surface area analyzer. The sample pretreatment was done in N_2 atmosphere at 150 °C for 5 h prior to N_2 adsorption-desorption studies to prevent the undesirable impurities and trapped gases. Barrett-Joyner-Halenda (BJH) method was used to attain the pore size distribution. Diffuse reflectance spectroscopy (DRS) was conducted in diffuse absorbance mode through Hitachi-3900H spectrophotometer. Photoluminescence (PL) spectroscopic studies were performed using Perkin Elmer LS-55, USA PL spectrometer at an excitation wavelength of 348 nm. The thermogravimetric analysis (TGA) of the as-prepared catalysts was performed with a TA Q500, USA thermal analyzer in N_2 flow (50 mL/min). About 10 mg of the catalyst was heated in a platinum pan and from ambient temperature to 800 °C at 5 °C min^{-1} ramp. The photocatalytic degradation of the organic pollutants was monitored using Champion UV-500 spectrophotometer.

3.2.4 Photocatalytic activity

The photocatalytic performance of Sb_2S_3/SiO_2 was investigated by degrading toxic dye MB along with a colorless insecticide TM. For the photodegradation of MB, about 5 mg of Sb_2S_3/SiO_2 monolith was added to an aqueous solution of 6 ppm MB (10 mL) in a quartz beaker. The above solution was stirred in dark for about 30 min to achieve the adsorption-desorption equilibrium. After that, the solution was illumined with different sources of light for comparison purposes. For visible light, the solution was kept under a 45 W CFL lamp (Philips) having intensity ~100 W/m^2 for 150 min till MB was completely degraded. For UV light, the solution was kept under a 100 W Hg lamp (365 nm) having flux density in the range of 46–48 W/m^2. A distance of about 10 cm was maintained between the lamp and the upper layer of the reaction mixture. The sunlight reaction was carried out from 11.00 am to 3:00 pm during October 2018 (24-26 October) and 9 March 2019. The vessel was placed horizontally to sunlight and stirred until degradation was complete. The solar radiation (flux) was measured by using Pyranometer (LICOR), USA under the direct sunlight exposure and the average solar radiation was ~610 to 660 W/m^2 during this period. For the degradation of TM, 1 mg of the monolith was mixed with 20 mL solution of 55 ppm TM in a quartz beaker and stirred in dark for 40 min and then illuminated under UV light for 180 min. The samples were analyzed at periodic intervals after separating the catalyst from the solution. All the experiments were performed in triplicates and error bars have been displayed in graphs (source of error ~5 % of the data).

A UV–visible spectrophotometer was employed to investigate the absorbance spectra of MB and TM at λ_{max}= 665 nm and 248 nm respectively after separating the photocatalyst from solution. Degradation efficiency (%D) was evaluated by using **Eq. (2.1)** as discussed in **chapter 2 (section 2.2.4)**. For the analysis of degradation products, GC-MS analysis was done. Samples for GC-MS were prepared as follows: The aqueous reaction mixture was collected after the photocatalytic reaction and catalyst was separated. The solvent was removed by drying at 40^{o}C and the residue was dissolved in dichloromethane. Shimadzu QP-2010 Plus with Thermal Desorption System TD 20. Conditions - split mode injector, helium carrier gas (flow rate=1 mL/min), injection volume= 1.21 µL, injector temperature= 260^{o}C, ion source temperature =220^{o}C. The initial oven temperature was 100^{o}C for 2 min hold time and increased to 280 ^{o}C at a ramp of 10 ^{o}C min^{-1} with a 20 min hold time. MS spectra were attained at a range m/z =40-650, scan speed=3333.

3.3 Results and discussion

3.3.1 Nitrogen adsorption-desorption analysis

To analyze the surface area of the as-prepared Sb_2S_3/SiO_2 monoliths, N_2 adsorption-desorption analysis was carried out. **Fig. 3.1(a)** represents the type IV isotherm for SiO_2 and

Sb_2S_3/SiO_2 monoliths and the H1 hysteresis loop with sharp sorption branches verify the characteristics of the mesoporous nature. The isotherm for pure bulk Sb_2S_3 was also of type IV. The BJH method was followed to deduce the pore size distribution **(Fig. 3.1b)** and it verified that the SiO_2 and Sb_2S_3/SiO_2 monoliths are of mesoporous nature. The BJH plot for bulk Sb_2S_3 powder indicates slight mesoporous nature. **Table 3.1** tabularizes the surface area, total pore volume and mean pore diameter of the prepared materials. The BET surface area for SiO_2 and Sb_2S_3/SiO_2 monolith was high enough for better adsorption while pure Sb_2S_3 powder has a very low surface area which is not favorable for efficient adsorption and ultimately degradation. This implies that SiO_2 plays a key role in enhancing the surface area by acting as a support.

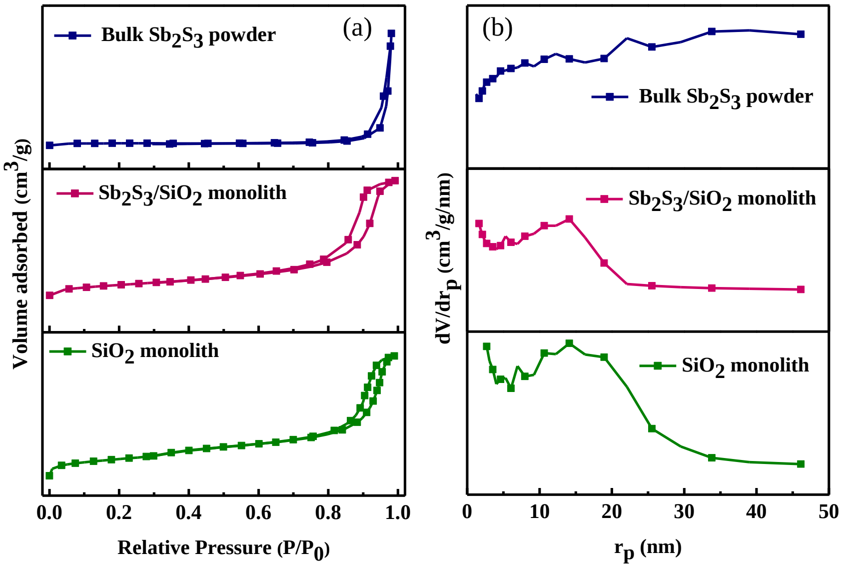

Fig. 3.1. (a) N_2 sorption curve and **(b)** BJH plot for as-prepared catalysts.

Table 3.1. Specific surface area, total pore volume and pore size of as-prepared catalysts.

Sample	Specific surface area (m^2/g)	Total pore volume (cm^3/g)	Mean pore diameter (nm)
SiO_2 monolith	469	1.130	9.70
Sb_2S_3/SiO_2 monolith	83	0.280	13.61
Bulk Sb_2S_3 powder	2	0.037	79.35

3.3.2 XRD analysis

Fig. 3.2 (a) displays the XRD patterns of Sb_2S_3/SiO_2 monolith. The broad peak centered at around 22° is due to the presence of SiO_2. The diffraction peaks obtained at 27.89° (021), 28.58° (320), 31.05° (040), 32.34° (221), 40.71° (141), 46.21° (431), 50.45° (202), 54.67° (312), 57.34° (621), and 58.82° (412) can be designated to Sb_2S_3 (JCPDS card No. 74-1046).[17]

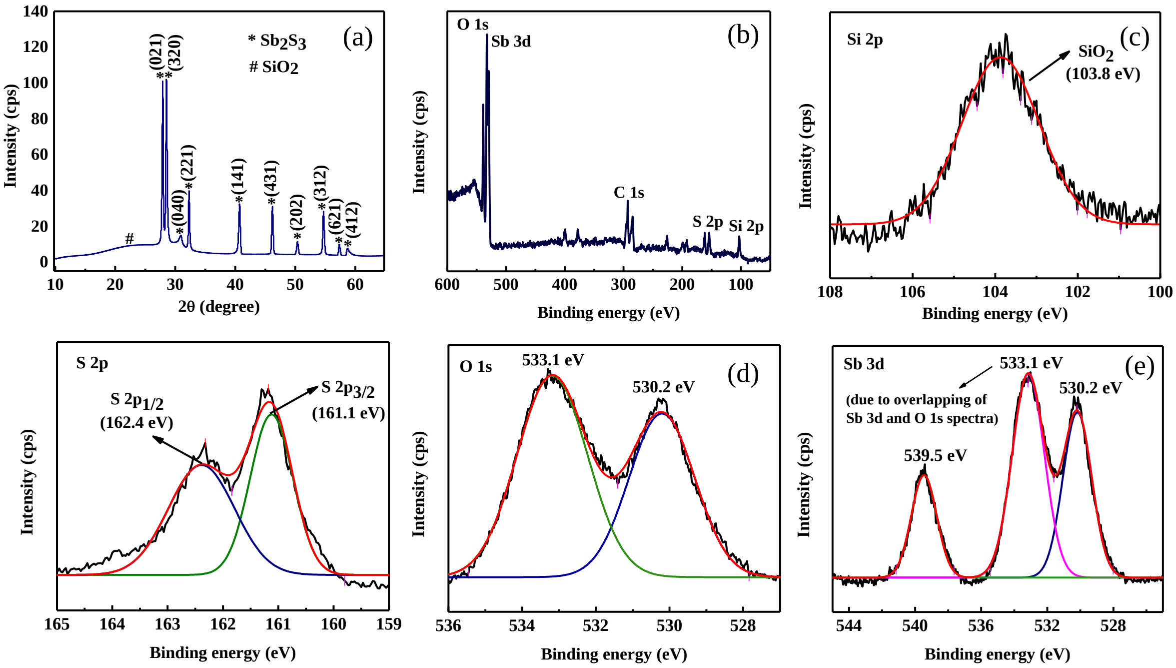

Fig. 3.2. (a) XRD plot for Sb_2S_3/SiO_2 monoliths, **(b-f)** XPS spectra of Sb_2S_3/SiO_2 monolith; **(b)** survey spectrum, **(c)** Si 2p, **(d)** S 2p, **(e)** O 1s, and **(f)** Sb 3d deconvoluted spectrum.

3.3.2 XPS analysis

Fig. 3.2(b) displays the XPS survey spectra of the as-prepared catalyst. The peaks in the survey spectra indicate that oxygen, silicon, antimony, and sulfur are the constituent elements in the Sb_2S_3/SiO_2 monolith. The C 1s peak arises owing to the adventitious carbon from XPS instrument as C 1s signal is taken as the reference at 284.5 eV to obtain binding energies for the constituent elements. De-convolution by least-squares Gaussian fit program was employed to fit the peaks. **Fig. 3.2(c)** shows the photoemission peaks for Si on the surface of Sb_2S_3/SiO_2 monolith. The presence of SiO_2 is confirmed by the single peak for Si 2p at 103.8 eV.[18] The characteristic peaks of S 2p at 161.1 and 162.4 eV are in agreement with S $2p_{3/2}$ and S $2p_{1/2}$ as displayed in **(Fig. 3.2(d))**.[19] Additionally, as shown in **Fig. 3.2(e)** the presence of O 1s peak at 530. 2 eV is due to O^{2-} anions,[20] whereas the peak at 533.1 eV is due to SiO_2.[21] The XPS spectra of Sb 3d is depicted in **Fig. 3.2(f)** revealing the presence of three peaks. The peaks at 530.2 and 539.5 eV match with Sb $3d_{5/2}$ and Sb $3d_{3/2}$ respectively due to the spin-orbit coupling. These peaks are characteristics of the Sb^{3+} verifying that Sb is not in the +5 state.[22] The peak at 533.1 eV may be due to the overlapping of O 1s spectra with that of Sb 3d.

3.3.4 EDS and Elemental mapping

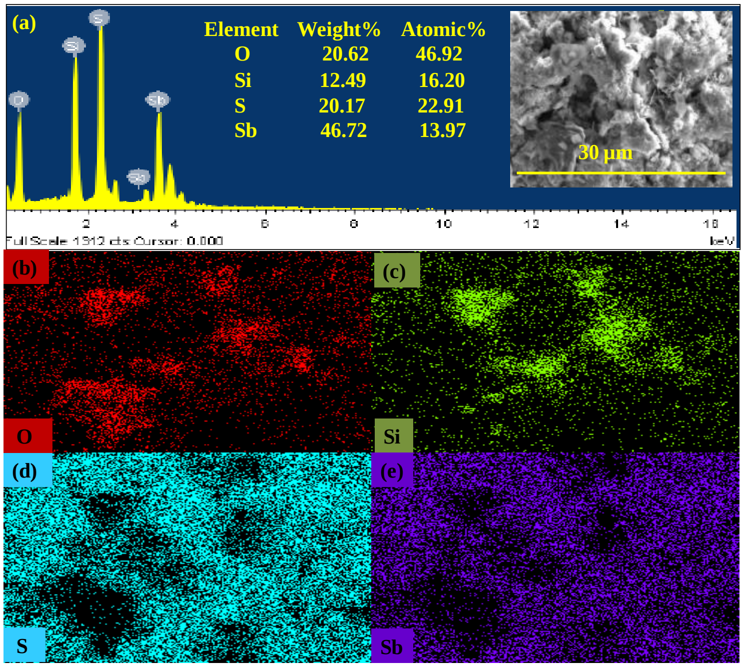

Element	Weight%	Atomic%
O	20.62	46.92
Si	12.49	16.20
S	20.17	22.91
Sb	46.72	13.97

Fig. 3.3. (a) EDS spectra, and **(b-e)** elemental color mapping of Sb_2S_3/SiO_2 monoliths.

The elemental composition and purity of Sb_2S_3/SiO_2 monoliths were investigated by means of EDS analysis. **Fig. 3.3(a)** displays the EDS spectra of the prepared monolith and **Fig. 3.3(b-e)** represents the elemental X-ray mapping and a homogeneous distribution of the elements was observed in the monolith. Uniform dispersal of the precursor salt all through the template of SiO_2 monoliths could possibly be responsible for this.

3.3.5 FESEM analysis

To evaluate the surface morphology of the monoliths, FESEM technique was used. The highly porous connected network structure of pure SiO_2 monoliths is evident from FESEM images **(Fig. 3.4(a-b))**. In the FESEM images of Sb_2S_3/SiO_2 monoliths exhibited in **Fig. 3.4(c-d)**, the Sb_2S_3 nanoflowers resembling 'mimosa pudica' flowers can be seen inside the mesoporous walls of SiO_2 monoliths.

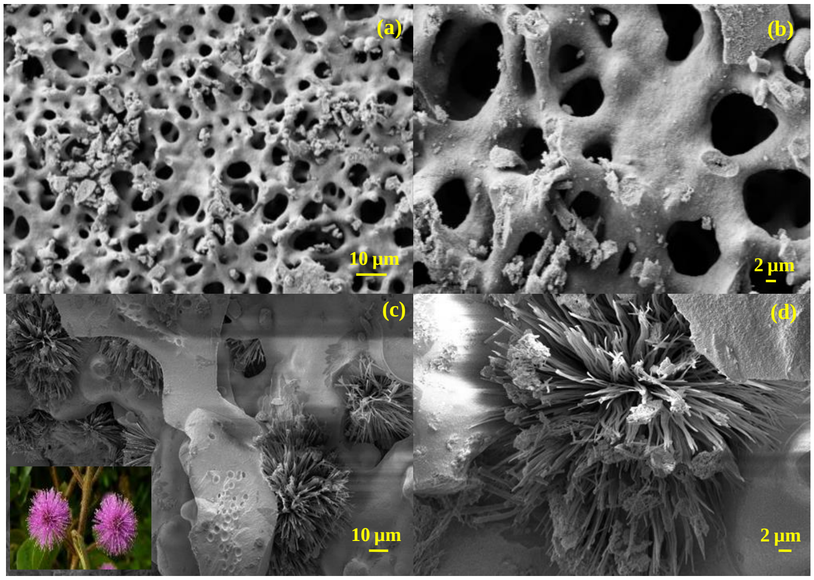

Fig. 3.4. FESEM images of **(a-b)** SiO_2 monoliths and **(c-d)** Sb_2S_3/SiO_2 monoliths (inset of (c) showing the image of mimosa pudica flower).

3.3.6 UV-visible DRS studies

The UV-visible DRS spectra of Sb_2S_3/SiO_2 monolith and bulk Sb_2S_3 powder are presented in **Fig. 3.5(a)**. The absorption range of both the materials is up to 800 nm which makes them visible-active. The band gap energies were evaluated from Tauc's relation (**Eq. (2.2), chapter 2).** The band gap value was obtained by extrapolating a tangent line **(Fig. 3.5b)** meeting X-axis.[23]. The band gap energies of Sb_2S_3/SiO_2 monolith and bulk Sb_2S_3 powder were found to be almost similar; 1.57 and 1.54 eV, respectively. The narrow band gap and capability to respond in the entire visible region makes prepared-monoliths a good choice of photocatalyst.[24]

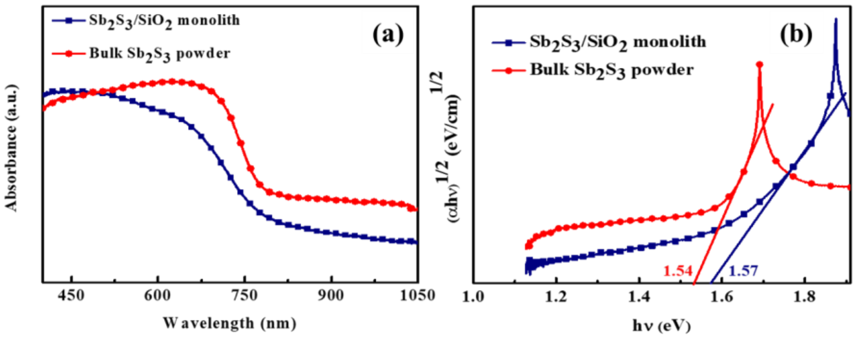

Fig. 3.5. (a) UV-vis DRS plot and **(b)** Tauc plot of Sb_2S_3/SiO_2 monolith and bulk Sb_2S_3 powder.

3.3.7 PL analysis

The recombination rate of charges in a photoactive material has a key role in the photocatalytic reaction. A low PL intensity indicates effectual charge separation efficacy and low recombination rate of electrons and holes.[25] The PL spectra of as-prepared materials were measured at an excitation wavelength of 348 nm **(Fig. 3.6a)**. The PL intensity of Sb_2S_3/SiO_2 monolith was lower than that of bulk Sb_2S_3 powder which implies that the photocatalytic efficiency of the former should be higher than the latter. This is because according to the results, the separation efficiency of photoinduced carriers in Sb_2S_3/SiO_2 monolith is greater than that of Sb_2S_3 powder. This could be due to the heterojunction established between Sb_2S_3 and SiO_2 and electron transport helps to reduce the recombination of charges.[9,26]

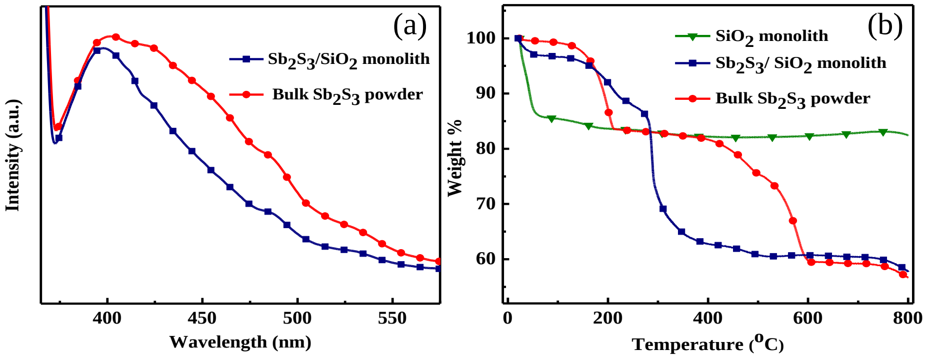

Fig. 3.6. (a) PL spectra and **(b)** TGA plot of as prepared materials.

3.3.8 TGA analysis

TGA analysis was performed in the N_2-atmosphere to examine the thermal stability of the catalysts as displayed in **Fig. 3.6(b)**. SiO_2 showed ~15 % weight loss starting at around 60 ^oC and no change thereafter that could be because of water loss. Bulk Sb_2S_3 powder showed first weight loss of ~15 % starting at 90-210^{o}C due to loss of adsorbed water from the surface. The second weight loss of ~22 % from 400-600^{o}C indicate the sulfide oxidation of Sb_2S_3 to Sb_2O_3.[27] Similarly, Sb_2S_3/SiO_2 monolith shows first weight loss at around 60-270 ^{o}C due to dehydration. The weight loss around 280-400°C could be accredited to the exothermic reactions because of the sulfide oxidation and formation Sb_2O_3.[28]

3.3.9 Photocatalytic degradation of MB

First of all, the photolysis experiment was conducted by irradiating 6 ppm of MB (without catalyst) with visible-light for 150 min and only ~10% photodegradation of MB was achieved **(Fig. 3.7)**.

3.3.9.1 Effect of catalyst concentration

An optimum concentration of Sb_2S_3/SiO_2 monolith was determined by varying the catalyst concentration from 0.1-0.7 g/L under visible light **(Fig. 3.7)**. It was noticed that the degradation efficiency improved with an increase in the concentration of catalyst from 0.1 to 0.5 g/L, then decreased at 0.7 g/L. This saturation occurred due to the rise in the opacity of dye solution which blocks the active sites.[29]

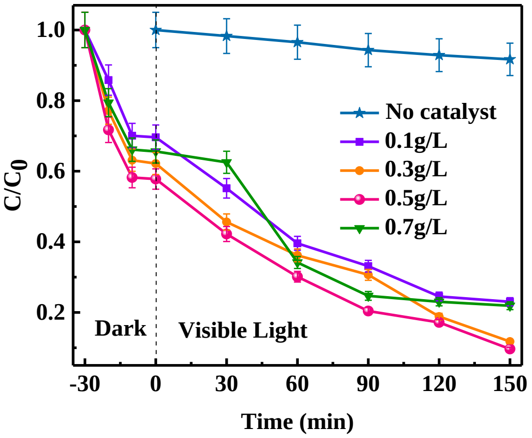

Fig. 3.7. Effect of catalyst concentration for photodegradation of MB by Sb_2S_3/SiO_2 monolith.

3.3.9.2 Effect of pH

The measurement of point of zero charge (pzc) on the surface of Sb_2S_3/SiO_2 monolith was carried out which helps to determine the influence of pH on the efficacy of degradation. The pzc measurement was done by the method reported by Mittal et al.[30] It is evident from **Fig. 3.8(a)** that pzc for Sb_2S_3/SiO_2 is around pH 3.8. **Fig. 3.8(b)** shows the effect of pH on the photodegradation of MB which confirms that at acidic pH there is no significant degradation taking place whereas at pH>3.8, degradation efficiency increases (best at pH 9). The adsorption of cationic adsorbents is favored when pH > pzc where major surface species on the catalyst surface is $M{-}O^-$ (M = metal); while the adsorption of anionic adsorbents is favored when pH < pzc when predominant species on the surface is $M{-}OH_2^+$. MB is a cationic dye, so at pH > 3.8 (pzc), the efficiency is much higher than at lower pH. In alkaline pH, the catalyst surface has a negative charge which is suitable for the adsorption and eventually degradation of MB (having positive surface). However, at higher basic pH (~ pH 10), the degradation efficiency decreases as metal hydroxide precipitates on the surface of the monolith which deactivates the whole of the active sites.

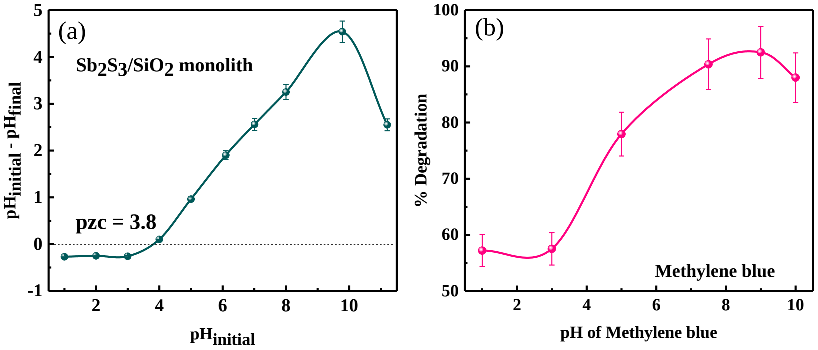

Fig. 3.8. Plot showing **(a)** pzc studies and **(b)** effect of initial pH on the photocatalytic degradation of MB by Sb_2S_3/SiO_2 monolith.

3.3.9.3 Effect of illumination area

The role of total effective illumination area was also investigated. In a typical experiment, the same volume of dye solution was taken in different reaction vessels with varying diameters of the vessels, so that the surface area of solution exposed to the light was different (~2.5, 5, 10, and 15 cm^2). The solutions were treated with 0.5 g/L of the catalyst under visible light illumination for 150 min as displayed in **Fig. 3.9.** In each case, a distance of about 10 cm was maintained between the lamp and the upper layer of the reaction mixture. Enhancement in degradation efficiency was noted as the illumination area (area of reaction mixture exposed to the irradiation source) of the reactor increased.[31]

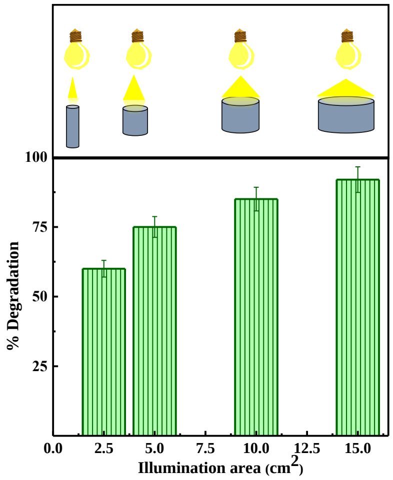

Fig. 3.9. Effect of illumination area on photodegradation of MB using Sb_2S_3/SiO_2 monolith.

3.3.9.4 Comparison of catalysts and light sources

The estimation of the rate constant was done by following **Eq. (2.3)** mentioned in **Chapter 2**. The photodegradation efficiency of Sb_2S_3/SiO_2 monoliths was compared to pure SiO_2 monolith, bulk Sb_2S_3 powder and commercial TiO_2 P25 **(Fig. 3.10(a))**. Bulk Sb_2S_3 powder and TiO_2 P25 have less degradation efficiency and rate constants (75 %; 0.0076 and 64 %; 0.0060 min^{-1}, respectively) as compared to Sb_2S_3/SiO_2 monolith (92.5 %; 0.014 min^{-1}) under visible light. MB gets completely adsorbed in the dark by pure SiO_2 monolith due to its high surface area. But it is well known that photodegradation is always better than adsorption for complete removal of toxic dyes. Therefore, Sb_2S_3/SiO_2 monolith is evidently a better choice than others.

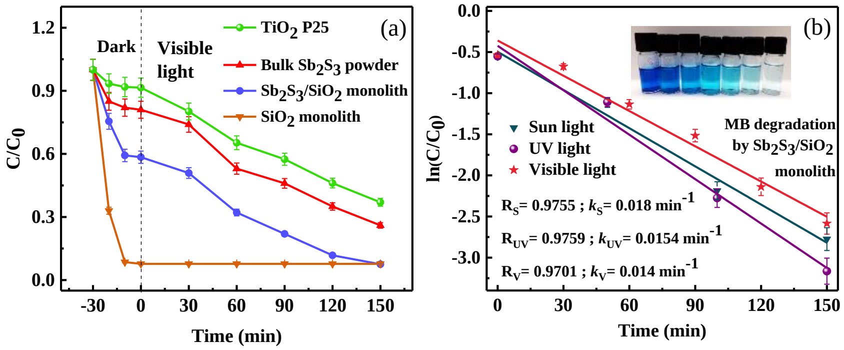

Fig. 3.10. Kinetic analysis for photodegradation of MB **(a)** by using various catalysts and **(b)** different light sources.

To draw a comparison among various light sources, the same experiment was conducted in UV light and natural sunlight. **Fig. 3.10(b)** depicts the kinetic analysis of MB solution under different light sources at optimum conditions of Sb_2S_3/SiO_2 monolith. The reaction follows a pseudo-first order. The degradation efficiency and rate constant followed the order: sunlight >UV>visible light as shown in **Table 3.2**.

Table 3.2. Comparison of different photocatalysts for MB degradation.

Photocatalyst	Time (min)/ light source	% degradation	Rate constant k (min^{-1})
TiO_2 P25	150 /visible light	64.0 %	0.0060
Bulk Sb_2S_3 powder	150 /visible light	75.0 %	0.0077
Sb_2S_3/SiO_2	150 /visible light	92.5 %	0.014
Sb_2S_3/SiO_2	150/ UV light	94.0 %	0.0154
Sb_2S_3/SiO_2	150/ Sunlight	96.0 %	0.018

3.3.9.5 GC-MS analysis of MB-degradation

For the identification of intermediates and products in the photodegradation reaction of MB, GC-MS analysis was carried out. The GC chromatogram and mass spectrum of MB after treatment are shown in **Fig. 3.11 (a)** and **(b)**, respectively. The proposed degradation pathway has been displayed in **Scheme 3.2**. MB is decomposed by the attack of hydroxyl radical and demethylation could cause breakage of N-CH_3 to form 5-chloro-5λ^4-phenothiazine-3,7-diamine (m/z=263.02) [M+2]+ which is further oxidized to form 4-aminobenzene-1,2-diol and 2-aminobenzenesulfonic acid (m/z=173.01) [M+2]+. The latter may further undergo N-C bond cleavage to form benzenesulfonic acid (m/z=158) [M]+ and then gets oxidized to phenol (m/z=94.04) [M+H]+. On the other hand, the oxidation of 2-aminobenzenesulfonic acid leads to formation of pyrocatechol (m/z=110.04) [M+H]+ and then cyclohexa-3,5-diene-1,2-dione (m/z=108.02) [M+H]+. These organic intermediates could finally get transformed into CO_2, H_2O, Cl^-, SO_4^{2-}, and NO_3^-. The findings were in accordance with the literature reports.[32,33]

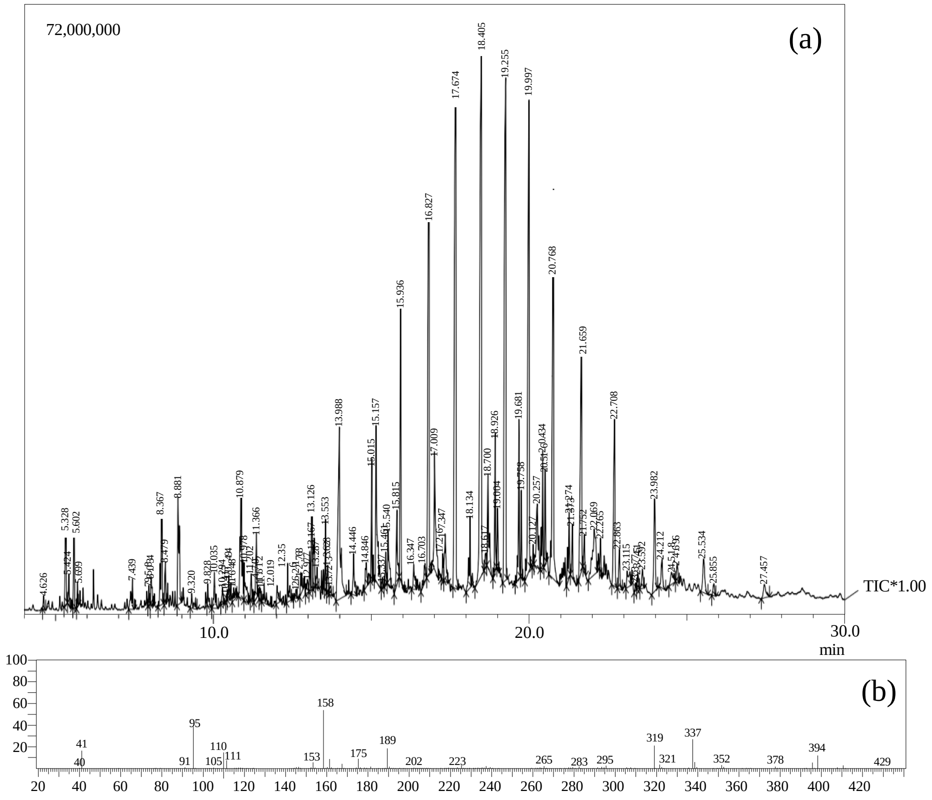

Fig. 3.11. (a) GC spectra of MB after photocatalytic degradation and **(b)** MS spectra of MB after photodegradation at retention time of 18.405 min.

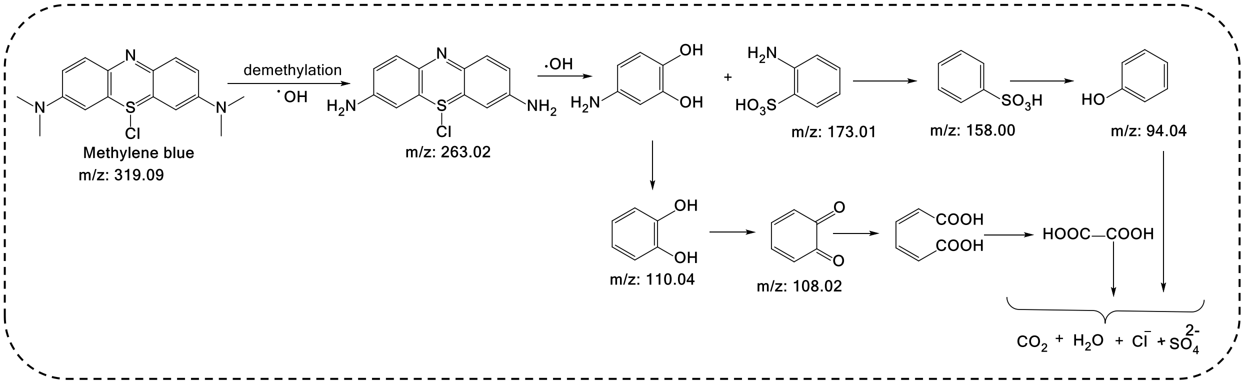

Scheme 3.2. Possible degradation pathway of MB by Sb_2S_3/SiO_2 monoliths.

3.3.10 Photocatalytic degradation of TM

To make a distinction if the photocatalysis is direct or indirect, the photodegradation of colorless insecticide, TM was performed. The experiments under various light sources was performed and further experiments were carried out in UV light as the best results were achieved in that condition **(Fig. 3.12(a))**. The concentration of catalyst was optimized by performing the photodegradation of 55 ppm TM under UV light illumination for 180 min. The catalyst concentration was varied from 0.01-0.1 g/L and 0.05 g/L was found to be the optimum concentration. Only ~16 % degradation was observed (without catalyst) on photolysis **(Fig. 3.12(b))**.

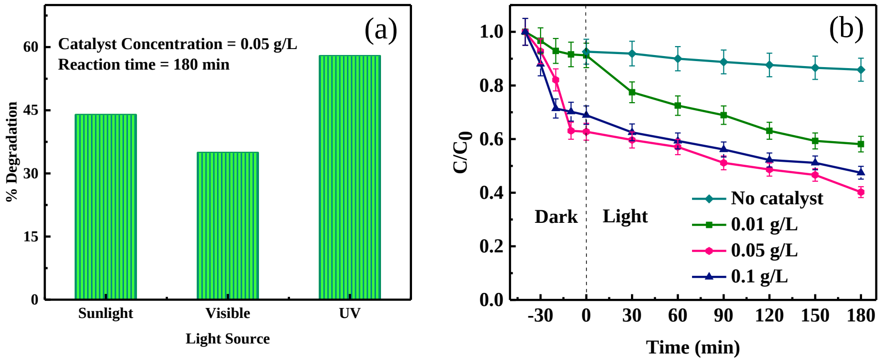

Fig. 3.12. Plot showing the effect of **(a)** light sources and **(b)** catalyst concentration on TM degradation using Sb_2S_3/SiO_2 monolith.

The influence of pH on the photodegradation of TM was also studied from pH 1-10. It is perceptible from **Fig. 3.13(a)** that initially the degradation increases as pH increases from 1 to 3 and then decreases when the medium changes to alkaline. Therefore, the optimum pH was found to be 3 and it can be justified from pzc value (3.8). The catalyst surface is positively charged whereas TM is anionic at pH 3 favoring better adsorption and enhanced photocatalytic degradation. At higher pH, there are significant repulsive forces amongst TM and catalyst surface.[34]

Furthermore, the kinetic analysis was carried out at optimal conditions and **Fig. 3.13(b)** shows the plot for kinetic analysis of photodegradation of TM under optimum conditions. The process follows pseudo first-order kinetics and around 70 % efficiency was achieved with a rate constant of 0.0057 min^{-1}.

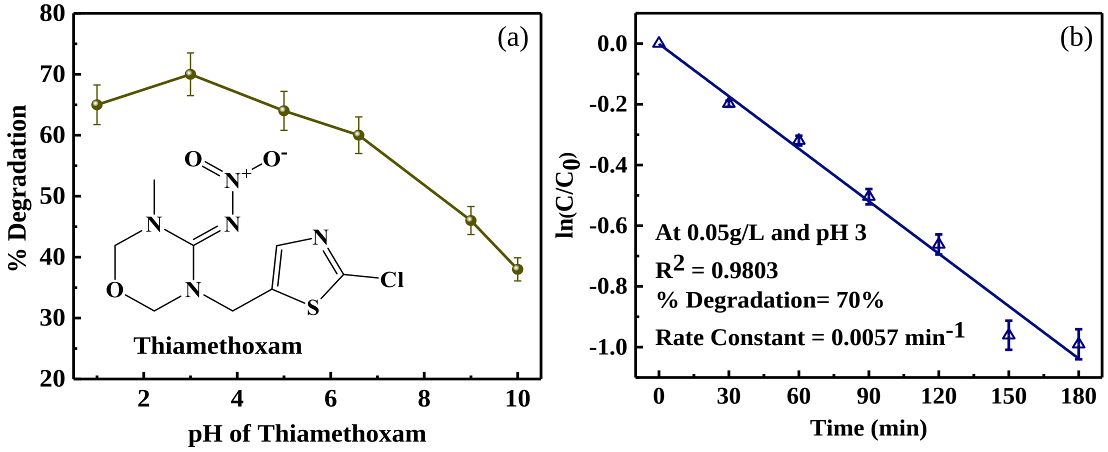

Fig. 3.13. (a) Effect of pH of TM solution and **(b)** kinetic analysis for TM degradation using Sb_2S_3/SiO_2 monolith.

3.3.10.1 GC-MS analysis of TM-degradation

For the identification of intermediates and products in the photodegradation reaction of TM, GC-MS analysis was carried out. The GC chromatogram and mass spectrum of TM after treatment are shown in **Fig. 3.14 (a)** and **(b)**, respectively.

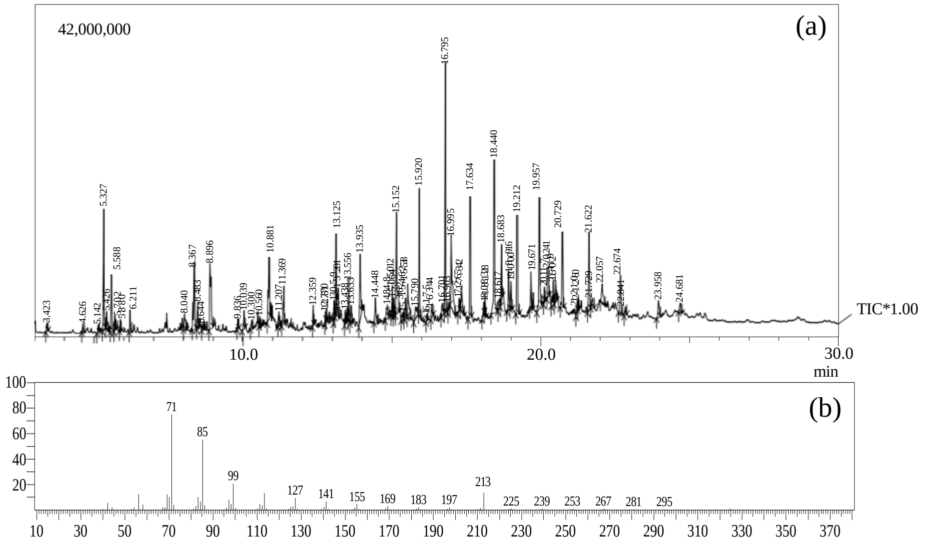

Fig. 3.14. (a) GC spectra of TM after photocatalytic degradation and **(b)** MS spectra of TM after photodegradation at retention time of 16.795 min.

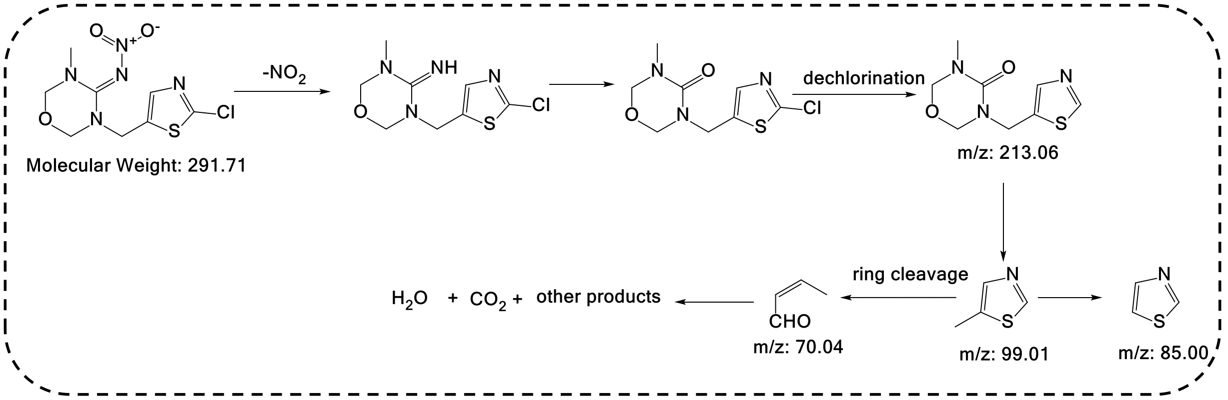

Scheme 3.3. Possible degradation pathway of TM by Sb_2S_3/SiO_2 monoliths.

The proposed degradation pathway has been displayed in **Scheme 3.3.** The de-nitration of TM molecule could lead to the formation of 3-((2-chlorothiazol-5-yl) methyl)-5-methyl-1,3,5-oxadiazinan-4-imine and the further oxidation of imine group oxidation of imine group to carbonyl group generates 3-((2-chlorothiazol-5-yl)methyl)-5-methyl-1,3,5-oxadiazinan-4-one. The dechlorination of this molecule forms 3-methyl-5-(thiazol-5-ylmethyl)-1,3,5-oxadiazinan-4-one (m/z=213.06) [M+]+. The N-C bond cleavage may then occur which removes the oxadiazinan-4-one ring to form 5-methylthiazole (m/z=99.01) [M+]+. This compound could either undergo demethylation to produce thiazole (m/z=85) [M+]+ or could undergo ring cleavage to generate (Z)-but-2-enal (m/z=70.04) [M+H]+. These compounds can further decompose to simpler hydrocarbons. The findings were in accordance with the literature reports.[35,36]

3.3.11 Comparison with literature

A comparative study of photodegradation of the pollutats with different photocatalysts accounted in the literature is presented in **Table 3.3.**

Table 3.3. Comparison of different photocatalysts for pollutant photodegradation.

Catalyst	Pollutant conc.	Catalyst conc. (g/L)	Time (min)/ light source	% degradation	Rate constant *k* (min^{-1})	Ref.
(1:4) ZnS:CdS	MB (10 ppm)	0.1	360/ visible light	73 %	0.0036	37
α-Fe_2O_3	MB (20 ppm)	2.5	498/ sunlight	97 %	0.0046	38
WO_3/TiO_2	MB (10 ppm)	0.5	120/ visible light	27 %	0.00197	39
WO_3/TiO_2	MB (10 ppm)	0.5	120/ UV light	90 %	0.018	39
(Yb, N)-TiO_2	MB (10 ppm)	3	300/ visible light	93.5 %	0.0091	40
SnO_2 quantum dots	TM (50 ppm)	0.1	45/ solar light	57 %	-	41
Sulfate doped-Ag_3PO_4	TM (5 ppm)	0.8	60 /visible light	39.94 %	0.008	42
CuO powder	TM (5 ppm)	1	60 /visible light	48.65	0.0109	43
Sb_2S_3/SiO_2	MB (6 ppm)	0.5	150 /visible light	92.5 %	0.014	This study
Sb_2S_3/SiO_2	TM (55 ppm)	0.05	180 /UV light	70 %	0.0057	This study

3.3.12 Reusability studies

From the perspective of the practical large-scale application, photocatalyst lifetime is of paramount importance. Hence it is essential to assess the photocatalytic stability of the photocatalyst for multiple experimental runs of degradation. The major advantage of the monolithic Sb_2S_3/SiO_2 is its easy-to-separate nature because of its solid rock-like structure (1 cm in length and 0.5 cm in diameter). The photocatalyst was washed using dilute NaOH then dried at 40 ºC for regeneration. The reproducibility of the as-prepared monoliths was investigated for 4 successive runs in the MB degradation in optimal conditions and around 71 % efficiency was noted exhibiting high reusability tendency **(Fig. 3.15)**.

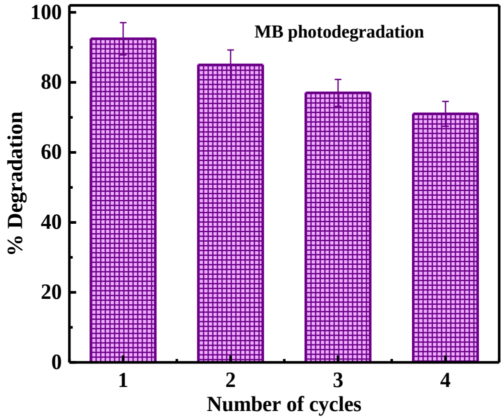

Fig. 3.15. Reusability studies of Sb_2S_3/SiO_2 monolith for photodegradation of MB.

3.3.12 Plausible mechanism

To investigate the major governing radical species in the photodegradation of MB and TM, trapping experiments were conducted using various scavengers like methanol, benzoquinone (BQ), IPA and DMSO for trapping holes (h^+), superoxide radicals ($O_2^{\bullet-}$), hydroxyl radicals ($^{\bullet}OH$) and electrons (e^-), respectively.[31] As shown in **Fig. 3.16 (a)**, in case of MB, the reaction was highly inhibited by BQ ($O_2^{\bullet-}$ scavenger) while in case of TM, the reaction was significantly repressed by methanol (h^+ scavenger). This implies that the degradation of TM and MB by Sb_2S_3/SiO_2 monolith was influenced primarily by holes and superoxide anion radicals, respectively which are the respective dominant photogenerated species in degradation mechanism. The Sb_2S_3/SiO_2 monolith absorbs photons of light having energy higher than its band gap energy due to which VB electrons (e^-) get excited to conduction band (CB) creating holes (h^+) in the VB. The holes then react with ^-OH to generate $^\bullet OH$ while e^- in CB react with O_2 to form $O_2^{\bullet-}$ respectively and these reactive species cause degradation of toxins (**Fig. 3.16(b)).**

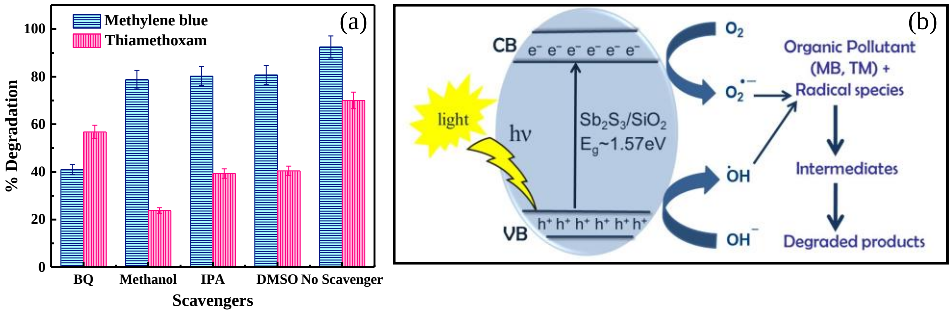

Fig. 3.16. (a) Effect of various scavengers on the photocatalytic degradation of pollutants and **(b)** mechanism for the photodegradation of MB and TM.

The possible reaction steps are shown in **Eqs. (3.1)-(3.6)**.

$$Sb_2S_3/SiO_2 + h\nu \rightarrow e^- + h^+ \tag{3.1}$$

$$H_2O + h^+ \rightarrow H_2O^+ \rightarrow {}^\bullet OH + H^+ \tag{3.2}$$

$$O_2 + e^- \rightarrow O_2^{\bullet-} \tag{3.3}$$

$$H_2O^+ \rightarrow {}^-OH + H^+ \tag{3.4}$$

$${}^-OH + h^+ \rightarrow {}^\bullet OH \tag{3.5}$$

$${}^\bullet OH/\ O_2^{\bullet-} + MB/TM \rightarrow \text{intermediates} \rightarrow \text{degraded products} \tag{3.6}$$

3.4 Conclusions

Fabrication of mesoporous visible-light-driven nanoflower-like Sb_2S_3/SiO_2 monoliths was done in this chapter and were afterwards employed for the photocatalytic degradation of model pollutants; MB and TM. The characterization results verified that Sb_2S_3 nanoflowers were very well decorated onto the SiO_2 surface and the composite had a high surface area which is suitable for photocatalytic degradation. The prepared-monoliths had a widespread light absorption range covering almost entire visible range. The narrow band gap energy and low recombination rate of the material justify its excellent photocatalytic activity. Different tests were conducted to examine the influence of solution pH, concentration of catalyst, light source, and illumination area on the photodegradation. The catalyst exhibited good efficiency in sunlight also with a high rate constant for MB degradation. The reusability studies suggested that the catalyst was highly reusable. The trapping experiments revealed that the superoxide anion radicals and holes were the major reactive species in the MB and TM degradation, respectively. The degraded products have also been analyzed through GC-MS studies. This study shows that the 'mimosa pudica' nanoflower-like Sb_2S_3/SiO_2 monolithic photocatalyst has a huge scope in wastewater treatment at a large scale primarily due to easy-to-separate and economical nature.

References

(1) Dong, S.; Feng, J.; Fan, M.; Pi, Y.; Hu, L.; Han, X.; Liu, M.; Sun, J.; Sun, J. Recent Developments in Heterogeneous Photocatalytic Water Treatment Using Visible Light-Responsive Photocatalysts: A Review. *RSC Adv.* **2015**, *5* (19), 14610–14630. https://doi.org/10.1039/c4ra13734e.

(2) Pietrzak, D.; Kania, J.; Kmiecik, E.; Malina, G.; Wątor, K. Fate of Selected Neonicotinoid Insecticides in Soil–Water Systems: Current State of the Art and Knowledge Gaps. *Chemosphere* **2020**, *255*, 126981. https://doi.org/10.1016/j.chemosphere.2020.126981.

(3) Zhao, Y.; Li, Y. Design of Environmentally Friendly Neonicotinoid Insecticides with Bioconcentration Tuning and Bi-Directional Selective Toxic Effects. *J. Clean. Prod.* **2019**. https://doi.org/10.1016/j.jclepro.2019.02.156.

(4) Dashairya, L.; Sharma, M.; Basu, S.; Saha, P. Enhanced Dye Degradation Using Hydrothermally Synthesized Nanostructured Sb_2S_3/RGO under Visible Light Irradiation. *J. Alloys Compd.* **2018**, *735*, 234–245. https://doi.org/10.1016/j.jallcom.2017.11.063.

(5) Ayappan, C.; Jayaraman, V.; Palanivel, B.; Pandikumar, A.; Mani, A. Facile Preparation

of Novel Sb2S3 Nanoparticles/Rod-like α-Ag_2WO_4 Heterojunction Photocatalysts: Continuous Modulation of Band Structure towards the Efficient Removal of Organic Contaminants. *Sep. Purif. Technol.* **2020**, *236*, 116302. https://doi.org/10.1016/j.seppur.2019.116302.

(6) Song, Y. T.; Lin, L. Y.; Chen, Y. S.; Chen, H. Q.; Ni, Z. De; Tu, C. C.; Yang, S. S. Novel TiO_2/Sb_2S_3 Heterojunction with Whole Visible-Light Response for Photoelectrochemical Water Splitting Reactions. *RSC Adv.* **2016**, *6* (54), 49130–49137. https://doi.org/10.1039/c6ra04094b.

(7) Baral, A.; Dhara, A.; Sinha, A.; Mukherjee, N. Chemically Synthesized Sb_2S_3 Hollow-Spheres for Significantly Fast and Reliable Visible Light Driven Dye Photodegradation. *Spectrochim. Acta Part A Mol. Biomol. Spectrosc.* **2021**, *250*, 119368. https://doi.org/10.1016/j.saa.2020.119368.

(8) Dashairya, L.; Sharma, S.; Rathi, A.; Saha, P.; Basu, S. Solar-Light-Driven Photocatalysis by Sb_2S_3/Carbon Based Composites towards Degradation of Noxious Organic Pollutants. *Mater. Chem. Phys.* **2021**, *273* (June), 125120. https://doi.org/10.1016/j.matchemphys.2021.125120.

(9) Hao, Q.; Niu, X.; Nie, C.; Hao, S.; Zou, W.; Ge, J.; Chen, D.; Yao, W. A Highly Efficient G-C_3N_4/SiO_2 Heterojunction: The Role of SiO_2 in the Enhancement of Visible Light Photocatalytic Activity . *Phys. Chem. Chem. Phys.* **2016**, *18* (46), 31410–31418. https://doi.org/10.1039/c6cp06122b.

(10) Shalom, M.; Inal, S.; Neher, D.; Antonietti, M. SiO_2/Carbon Nitride Composite Materials: The Role of Surfaces for Enhanced Photocatalysis. *Catal. Today* **2014**, *225*, 185–190. https://doi.org/10.1016/j.cattod.2013.12.013.

(11) Smått, J. H.; Weidenthaler, C.; Rosenholm, J. B.; Lindén, M. Hierarchically Porous Metal Oxide Monoliths Prepared by the Nanocasting Route. *Chem. Mater.* **2006**, *18* (6), 1443–1450. https://doi.org/10.1021/cm051880p.

(12) Li, X.; Yu, J.; Jaroniec, M. Hierarchical Photocatalysts. *Chem. Soc. Rev.* **2016**, *45*, 2603–2636. https://doi.org/10.1039/c5cs00838g.

(13) Almarzooqi, S. H.; Katsiotis, M. S.; Alhassan, S. M. Hybrid Porous Molybdenum Disulfide Monolith for Liquid Removal of Dibenzothiophene. *Ind. Eng. Chem. Res.* **2017**, *56* (51), 15049–15057. https://doi.org/10.1021/acs.iecr.7b03313.

(14) Korala, L.; Germain, J. R.; Chen, E.; Pala, I. R.; Li, D.; Brock, S. L. CdS Aerogels as Efficient Photocatalysts for Degradation of Organic Dyes under Visible Light Irradiation. *Inorg. Chem. Front.* **2017**, *4* (9), 1451–1457. https://doi.org/10.1039/c7qi00140a.

(15) Fleischmann, S.; Dörr, T. S.; Frank, A.; Hieke, S. W.; Doblas-Jimenez, D.; Scheu, C.; de Oliveira, P. W.; Kraus, T.; Presser, V. Gyroidal Niobium Sulfide/Carbon Hybrid Monoliths for Electrochemical Energy Storage. *Batter. Supercaps* **2019**, *2* (8), 668–672. https://doi.org/10.1002/batt.201900035.

(16) Chen, L.; Zhu, W.; Han, Q.; Yang, X.; Lu, L.; Wang, X. Preparation of Rod-like Sb2S3 Dendrites Processed in Conventional Hydrothermal. *Mater. Lett.* **2009**, *63* (15), 1258–1261. https://doi.org/10.1016/j.matlet.2009.02.055.

(17) Khalil, A.; Aboamera, N. M.; Nasser, W. S.; Mahmoud, W. H.; Mohamed, G. G. Photodegradation of Organic Dyes by PAN/SiO_2-TiO_2-NH_2 Nanofiber Membrane under Visible Light. *Sep. Purif. Technol.* **2019**, *224*, 509–514. https://doi.org/10.1016/j.seppur.2019.05.056.

(18) Sri Devi Kumari, T.; Jeyakumar, D.; Prem Kumar, T. Nano Silicon Carbide: A New Lithium-Insertion Anode Material on the Horizon. *RSC Adv.* **2013**, *3* (35), 15028–15034. https://doi.org/10.1039/c3ra40798e.

(19) Ji, L.; Yan, P.; Zhu, C.; Ma, C.; Wu, W.; Wei, C.; Shen, Y.; Chu, S.; Wang, J.; Du, Y.; et al. One-Pot Synthesis of Porous 1T-Phase MoS2 Integrated with Single-Atom Cu Doping for Enhancing Electrocatalytic Hydrogen Evolution Reaction. *Appl. Catal. B Environ.* **2019**, *251*, 87–93. https://doi.org/10.1016/j.apcatb.2019.03.053.

(20) Gajraj, V.; Mariappan, C. R. Electrochemical Performances of Asymmetric Aqueous Supercapacitor Based on Porous $Cu_3Mo_2O_9$ Petals and $La_2Mo_3O_{12}$ Nanoparticles Fabricated through a Simple Co-Precipitation Method. *Appl. Surf. Sci.* **2020**, *512*, 145648. https://doi.org/10.1016/j.apsusc.2020.145648.

(21) Gil, J. .; Ferreira, L. F.; Silva, V. C.; Oliveira, A. C.; de Oliveira, R. R.; Jacinto, M. J. Facile Fabrication of Functionalized Core-Shell Fe_3O_4@SiO_2@Pd Microspheres by Urea-Assisted Hydrothermal Route and Their Application in the Reduction of Nitro Compounds. *Environ. Nanotechnology, Monit. Manag.* **2019**, *11*, 100220. https://doi.org/10.1016/j.enmm.2019.100220.

(22) Ota, J.; Srivastava, S. K. Tartaric Acid Assisted Growth of Sb_2S_3 Nanorods by a Simple

Wet Chemical Method. *Cryst. Growth Des.* **2007**, *7* (2), 343–347. https://doi.org/10.1021/cg0605537.

(23) Méndez-Romero, U. A.; Pérez-García, S. A.; Xu, X.; Wang, E.; Licea-Jiménez, L. Functionalized Reduced Graphene Oxide with Tunable Band Gap and Good Solubility in Organic Solvents. *Carbon N. Y.* **2019**, *146*, 491–502. https://doi.org/10.1016/j.carbon.2019.02.023.

(24) Li, K. Q.; Huang, F. Q.; Lin, X. P. Pristine Narrow-Bandgap Sb_2S_3 as a High-Efficiency Visible-Light Responsive Photocatalyst. *Scr. Mater.* **2008**, *58* (10), 834–837. https://doi.org/10.1016/j.scriptamat.2007.12.033.

(25) Wang, J.; Zhang, G.; Li, J.; Wang, K. Novel Three-Dimensional Flowerlike BiOBr/Bi_2 SiO_5 p–n Heterostructured Nanocomposite for Degradation of Tetracycline: Enhanced Visible Light Photocatalytic Activity and Mechanism. *ACS Sustain. Chem. Eng.* **2018**, *6* (11), 14221–14229. https://doi.org/10.1021/acssuschemeng.8b02869.

(26) Yang, L.; Wang, P.; Yin, J.; Wang, C.; Dong, G.; Wang, Y.; Ho, W. Engineering of Reduced Graphene Oxide on Nanosheet–g-C_3N_4/Perylene Imide Heterojunction for Enhanced Photocatalytic Redox Performance. *Appl. Catal. B Environ.* **2019**, *250* (February), 42–51. https://doi.org/10.1016/j.apcatb.2019.02.076.

(27) Shitole, K. D.; Patil, A. B.; Thakur, P. Preparation and Characterization of Sb_2S_3-TiO_2 Nanocomposite for the Enhanced Photocatalytic Degradation and Mineralization of Azo Dye. *Environ. Eng. Sci.* **2016**, *33* (8), 536–543. https://doi.org/10.1089/ees.2016.0086.

(28) Dashairya, L.; Mehta, A.; Saha, P.; Basu, S. Visible-Light-Induced Enhanced Photocatalytic Degradation of Rhodamine-B Dye Using $Bi_xSb_{2-X}S_3$ Solid-Solution Photocatalysts. *J. Colloid Interface Sci.* **2020**, *561*, 71–82. https://doi.org/10.1016/j.jcis.2019.11.118.

(29) Aanchal; Barman, S.; Basu, S. Complete Removal of Endocrine Disrupting Compound and Toxic Dye by Visible Light Active Porous G-C_3N_4/H-ZSM-5 Nanocomposite. *Chemosphere* **2020**, *241*, 124981. https://doi.org/10.1016/j.chemosphere.2019.124981.

(30) Mittal, H.; Maity, A.; Ray, S. S. Effective Removal of Cationic Dyes from Aqueous Solution Using Gum Ghatti-Based Biodegradable Hydrogel. *Int. J. Biol. Macromol.* **2015**, *79*, 8–20. https://doi.org/10.1016/j.ijbiomac.2015.04.045.

(31) Mehta, A.; Mishra, A.; Basu, S. Fluorescent Carbon Dot Decorated MnO_2 Nanorods for

Complete Photomineralization of Phenol from Water. *Environ. Sci. Water Res. Technol.* **2018**, *4* (12), 2012–2020. https://doi.org/10.1039/c8ew00235e.

(32) Wang, Q.; Tian, S.; Ning, P. Degradation Mechanism of Methylene Blue in a Heterogeneous Fenton-like Reaction Catalyzed by Ferrocene. *Ind. Eng. Chem. Res.* **2014**, *53* (2), 643–649. https://doi.org/10.1021/ie403402q.

(33) Houas, A.; Lachheb, H.; Ksibi, M.; Elaloui, E.; Guillard, C.; Herrmann, J. M. Photocatalytic Degradation Pathway of Methylene Blue in Water. *Appl. Catal. B Environ.* **2001**, *31* (2), 145–157. https://doi.org/10.1016/S0926-3373(00)00276-9.

(34) Mir, N. A.; Khan, A.; Muneer, M.; Vijayalakhsmi, S. Photocatalytic Degradation of a Widely Used Insecticide Thiamethoxam in Aqueous Suspension of TiO_2: Adsorption, Kinetics, Product Analysis and Toxicity Assessment. *Sci. Total Environ.* **2013**, *458–460*, 388–398. https://doi.org/10.1016/j.scitotenv.2013.04.041.

(35) Singla, S.; Sharma, S.; Basu, S. MoS_2/WO_3 Heterojunction with the Intensified Photocatalytic Performance for Decomposition of Organic Pollutants under the Broad Array of Solar Light. *J. Clean. Prod.* **2021**, *324* (May), 129290. https://doi.org/10.1016/j.jclepro.2021.129290.

(36) Rani, M.; Shanker, U. Removal of Chlorpyrifos, Thiamethoxam, and Tebuconazole from Water Using Green Synthesized Metal Hexacyanoferrate Nanoparticles. *Environ. Sci. Pollut. Res.* **2018**, *25* (11), 10878–10893. https://doi.org/10.1007/s11356-018-1346-2.

(37) Soltani, N.; Saion, E.; Hussein, M. Z.; Erfani, M.; Abedini, A. Visible Light-Induced Degradation of Methylene Blue in the Presence of Photocatalytic ZnS and CdS Nanoparticles. *Int. J. Mol. Sci.* **2012**, *4*, 12242–12258. https://doi.org/10.3390/ijms131012242.

(38) Tan, W. F.; Yu, Y. T.; Wang, M. X.; Liu, F.; Koopal, L. K. Shape Evolution Synthesis of Monodisperse Spherical, Ellipsoidal, and Elongated Hematite (α-Fe_2O_3) Nanoparticles Using Ascorbic Acid. *Cryst. Growth Des.* **2014**, *14* (1), 157–164. https://doi.org/10.1021/cg401334d.

(39) Yang, L.; Si, Z.; Weng, D.; Yao, Y. Synthesis, Characterization and Photocatalytic Activity of Porous WO_3/TiO_2 Hollow Microspheres. *Appl. Surf. Sci.* **2014**, *313*, 470–478. https://doi.org/10.1016/j.apsusc.2014.05.230.

(40) Zhang, J.; Xu, L. J.; Zhu, Z. Q.; Liu, Q. J. Synthesis and Properties of (Yb, N)-TiO_2

Photocatalyst for Degradation of Methylene Blue (MB) under Visible Light Irradiation. *Mater. Res. Bull.* **2015**, *70*, 358–364. https://doi.org/10.1016/j.materresbull.2015.04.060.

(41) Das, J.; Dhar, S. S. Synthesis of SnO_2 Quantum Dots Mediated by Camellia Sinensis Shoots for Degradation of Thiamethoxam. *Toxicol. Environ. Chem.* **2020**, *102* (1–4), 186–196. https://doi.org/10.1080/02772248.2020.1776285.

(42) Lee, Y.-J.; Kang, J.-K.; Park, S.-J.; Lee, C.-G.; Moon, J.-K.; Alvarez, P. J. J. Photocatalytic Degradation of Neonicotinoid Insecticides Using Sulfate-Doped Ag_3PO_4 with Enhanced Visible Light Activity. *Chem. Eng. J.* **2020**, *402*, 126183. https://doi.org/10.1016/j.cej.2020.126183.

(43) Jansanthea, P.; Saovakon, C.; Chomkitichai, W.; Ketwaraporn, J.; Maneepong, S.; Chaiwong, N.; Jaisee, K.; Wansao, C.; Wanaek, A.; Pookmanee, P. Thiamethoxam Insecticide Degradation with a Leaf-Like Cupric Oxide Monoclinic Structure Synthesized via the Microwave Method. *Russ. J. Inorg. Chem.* **2021**, *66* (5), 667–678. https://doi.org/10.1134/S0036023621050089.

Chapter 4

Photocatalytic abatement of recalcitrant pollutants by visible-light-driven centimeter-length MoO_3/SiO_2 monoliths

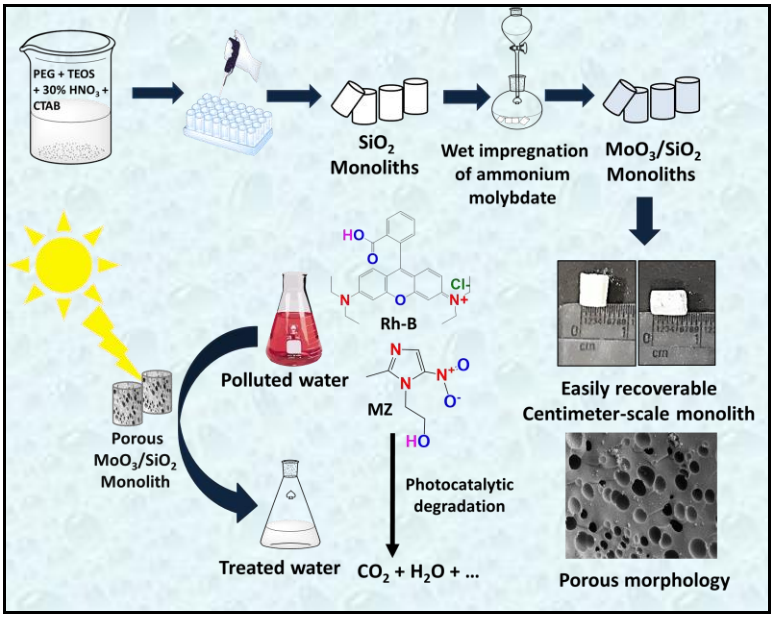

Highlights

- MoO_3/SiO_2 monoliths with a high surface-area at centimeter-level were prepared via wet impregnation method.
- The material was tested for the photodegradation of rhodamine-B dye and metronidazole antibiotic in visible/sunlight which were degraded around 88.6 % and 67.4%, respectively.
- Photodegradation of raw industrial wastewater was also carried out to gauge its effectiveness and almost 64% COD and 57% TOC-removal.

4.1 Introduction

Pharmaceutical pollutants, particularly antibiotics have also become a serious concern in modern times as they exhibit adverse effects on the environment.[1] Metronidazole (MZ) is a highly water-soluble, non-biodegradable antibiotic drug that is progressively found in groundwater as well as surface water in residual concentrations.[2] The accumulation of MZ can occur in water and can result in mutagenicity and carcinogenicity.[3] In addition to MZ, Rh-B was used as model pollutant in this chapter. Rh-B is a fluorescent xanthene dye soluble in water and is largely used in the dyeing industry.[4] Exposure to Rh-B may lead to nausea, skin allergies, nasal burning and itching, gastrointestinal disorders, eye allergies, and neuro as well as reproductive toxicity.[5]

Lately, MoO_3 has received considerable recognition in the domain of energy storage, gas sensors, photochromic and electrochromic devices besides catalysis.[6] MoO_3-based photocatalysts reportedly have high photon absorbing capacity[7] and are non-toxic and chemically stable in nature.[8] The estimated VB and CB band positions for MoO_3 in literature are 3.32 eV and 0.47 eV, respectively.[9] The VB edge potential is more positive than oxidation potential of $H_2O/{}^\bullet OH$ (2.38 eV) and thus, ${}^\bullet OH$ radicals can be generated. However, the single-electron reduction of oxygen $O_2/O_2^{\bullet-}$ (−0.33 eV) is not feasible.[10] Alex et al.[7] integrated ferroelectric $BaTiO_3$ with MoO_3 to form heterojunction and tested it for the photodegradation of Rh-B (~86% removal). Recently, Z-scheme α-MnO_2 nanorod/α-MoO_3 composite was prepared and utilized for visible-light photodegradation of acid blue 92 dye.[8] The combination of MoO_3 and SiO_2 can be beneficial for augmenting the photocatalytic activity as the presence of SiO_2 affects the recombination rate of charges in addition to increasing the surface area as well as the number of active sites.[11] The monolithic MoO_3 facilitates a large surface area as well as more number of active sites that stimulates the reaction kinetics.[12] Moreover, there is an enhanced light-harvesting character as monolithic catalysts permit multiple reflections as well as the scattering of light not only inside the pore channels but also within the interiors of cavities.[12]

This chapter presents the fabrication of porous MoO_3/SiO_2 monoliths by the wet-impregnation technique and evaluation of their photocatalytic performance for the degradation of

Rh-B and pharmaceutical-contaminant MZ. Diverse factors viz. effects of catalyst as well as pollutant concentrations, light source, illumination area, pH, reusability studies have been thoroughly investigated. The trapping experiments were also performed to discover the photodegradation mechanism. Photocatalytic treatment of raw industrial wastewater by MoO_3/SiO_2 monoliths was also examined.

4.2 Experimental section

This section comprises of the chemicals, materials and the methodologies used for the synthesis of catalysts.

4.2.1 Chemicals and materials

Ammonium molybdate tetrahydrate (98%), methanol (99.8%) (HPLC grade), and Rh-B were obtained from Loba Chemie. TiO_2 P25 nanopowder was gifted by Evonik industries, Germany. MZ antibiotic traded under the brand name of Flagyl was obtained from a local pharmacy. Raw wastewater was obtained from textile industry, Ludhiana, Punjab, India.

4.2.2 Syntheses

This section includes the synthesis methodologies of MoO_3/SiO_2 monoliths and bulk MoO_3 powder.

4.2.2.1 Synthesis of MoO_3/SiO_2 monoliths

Firstly, the silica monoliths were synthesized as per the procedure described in **Chapter 2 (section 2.2.1)**. Thereafter, to fabricate MoO_3/SiO_2 monoliths, wet-impregnation a 0.5 M aqueous solution of ammonium molybdate tetrahydrate was done into properly outgassed SiO_2 monoliths under vacuum and dried at 60°C. These steps were repeated three times for proper impregnation. Lastly, calcination at 500°C for 4 h at the rate of 2 °C min^{-1} was carried out to obtain MoO_3/SiO_2 monoliths. The prepared monoliths were bluish-white having length~ 0.7 cm and diameter~0.5 cm. **Scheme 4.1** illustrates the real pictures regarding preparation of MoO_3/SiO_2 monoliths.

4.2.2.2 Synthesis of bulk MoO_3 powder

Bulk MoO_3 powder was as well prepared for comparing its photocatalytic activity with MoO_3/SiO_2 monolith. Ammonium molybdate tetrahydrate was decomposed at 500 ^oC for 4 h in a muffle furnace. The obtained solid powder was washed thoroughly washed double distilled water thrice and dried up at 60 ^oC.[13]

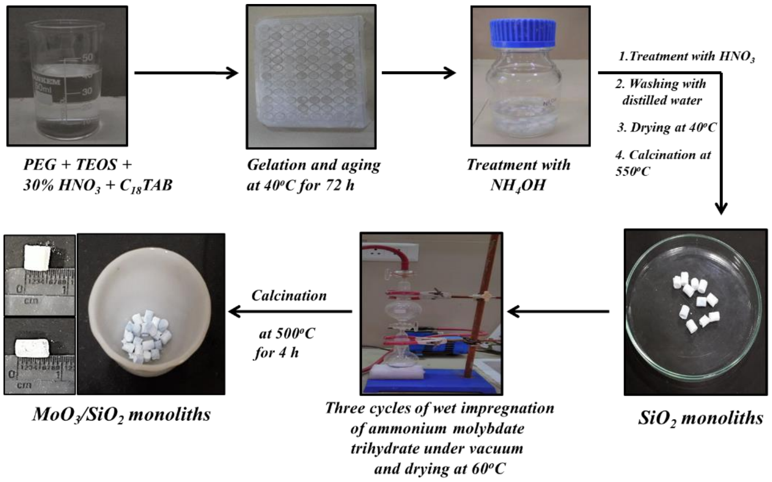

Scheme 4.1. Steps for the preparation of MoO_3/SiO_2 monoliths.

4.2.3 Characterization methods

PANALYTICAL X'Pert PRO X-ray diffractometer was employed for performing X-ray diffraction analysis (XRD) with Cu Kα (λ=1.540Å) radiation. The instrument operated at 45 kV with 2Θ=5 to 80^o and step size of 0.0260^o. The X-ray photon spectroscopy (XPS) was performed using PHI-5000 VersaProbe III system. The FESEM images were acquired through ZEISS FESEM operational at an accelerating voltage of 5 kV. JEOL JSM-6510 with Oxford INCA energy dispersive spectrometer (EDS) operational at an accelerating voltage of 5 kV was employed to acquire SEM-EDS and elemental mapping images. Brunauer-Emmett-Teller (BET) theory was employed for evaluating surface area through Microtrac Belsorp Mini-II (Bel, Japan, Inc) surface area analyzer. The materials were pretreated before measurement under nitrogen atmosphere at 100°C for 6 h in order to refrain from the unwanted impurities/gases. Barrett-

Joyner-Halenda (BJH) model was utilized for evaluating pore size distribution. The HR-TEM (High Resolution Transmission Electron Microscope) analysis was performed on TALOS F200S G2 (200 KV, FEG, CMOS Camera 4 K × 4 K). UV–Vis diffuse reflectance spectroscopy (DRS) has been performed via Hitachi-3900H spectrophotometer through diffuse absorbance mode. Perkin Elmer LS-55, USA photoluminescence (PL) spectrometer was used for PL analysis at an excitation wavelength of 325 nm. The photodegradation of the model pollutants was observed by means of Shimadzu UV-2600 spectrophotometer. Total organic carbon (TOC) analyzer (model: Multi N/C 2100 BU, Analytik Jena AG Corporation) has been employed for evaluating TOC.

4.2.4 Photocatalytic activity

The photocatalytic performance of MoO_3/SiO_2 monoliths was tested for the photodegradation of model dye Rh-B and pharmaceutical-pollutant MZ. Around 0.3 g/L of MoO_3/SiO_2 catalyst was added into 20 mL of aqueous Rh-B solution (5 ppm). The stirring of the solution for 60 min was firstly done in dark for establishing adsorption-desorption equilibrium. Subsequently, it was illumined with visible light (a 45 W CFL lamp (Philips); intensity ~100 W/m^2) for 150 min. Similarly, stirring of 20 mL of aqueous MZ solution (10 ppm) mixed with ~0.1 g/L of the monolith was carried out in dark for 40 min and later irradiated with visible radiation for 180 min. A fixed gap of around 10 cm was kept amongst the light source and the uppermost layer of the solution. The sunlight reaction was carried out during October 2020. The vessel was positioned horizontally to sunlight; the average solar radiation was ~650 W/m^2 for this period. All the tests were conducted thrice and the average was noted and the error bars (source of error ~5 % of the data) have been shown in the plots. The degradation of Rh-B and MZ was monitored using UV–visible spectrophotometer at λ_{max}= 555 and 319 nm, respectively. Degradation efficiency (%D) was evaluated by using **Eq. (2.1)** as discussed in **chapter 2 (section 2.2.4).**

For the analysis of degradation products, GC-MS analysis was done. Samples for GC-MS were prepared as follows: The aqueous reaction mixture was collected after the photocatalytic reaction and catalyst was separated. The solvent was removed by drying at 30°C and the residue was dissolved in methanol. Thermo Trace 1300 GC coupled with ThermoScientific TSQ 8000 triple quadrupole MS equipped with a split/split less injector was used. Conditions - splitless mode injector, column: BP 5MS (30 m × 0.25 mm; 0.25 µm), column makeup: 5% phenyl polysilphenylene-siloxane, helium carrier gas (flow rate=1 mL/min), injection volume= 1 µL, injector temperature= 250^{o}C, MS transfer line temperature =240^{o}C, ion source temperature =230^{o}C. The initial oven temperature was 50^{o}C for 1 min hold time and increased to 150 ^{o}C at a ramp of 10 ^{o}C min^{-1} with a 1 min hold time, this was increased to 250 ^{o}C with a ramp of 8 ^{o}C min^{-1} for a 1 min hold at 15 ^{o}C min^{-1} to 280 ^{o}C for 5 min hold. MS spectra were attained at a range m/z =40-650, scans= 3525. Software used: Xcalibur 2.2SP1 with foundation 2.0SP1.

The photocatalytic treatment of real wastewater was evaluated through COD and TOC analyses. About 50 mL of wastewater was mixed with 0.3 g/L MoO_3/SiO_2 monolith and given treatment in visible irradiation for 150 min. The COD value was estimated through the titrimetric technique while mineralization was estimated in terms of TOC removal. **Eq. (4.1)** and **Eq. (4.2)** were followed for the evaluation of percentage COD and TOC removal, respectively. COD_i, COD_f, TOC_i, and TOC_f are the COD and TOC values of real wastewater at the initial time and a certain time t, respectively.

$$\%COD = \{(COD_i - COD_f)/ COD_i\}\times 100 \qquad (4.1)$$

$$\%TOC = \{(TOC_i - TOC_f)/ TOC_i\}\times 100 \qquad (4.2)$$

4.3 Results and discussion

4.3.1 Nitrogen adsorption-desorption studies

The N_2 sorption studies were performed to evaluate the surface area of the synthesized materials. Type IV isotherms with H1 hysteresis loop in addition to sharp sorption branches in SiO_2 and MoO_3/SiO_2 monolith validated the presence of mesopores **(Fig. 4.1a)**. The specific surface area (SSA), mean pore diameter (MPD), and total pore volume (TPV) of the synthesized materials are mentioned in the plots. The BJH method for determining pore size distribution confirmed the mesoporous nature of SiO_2 as well as MoO_3/SiO_2 monoliths as shown in **Fig. 4.1b**. The SSA and TPV decreased whereas the MPD increased after the transformation of SiO_2

monoliths to MoO_3/SiO_2 monoliths. The SSA of MoO_3/SiO_2 (202 m^2/g) was substantially greater than MoO_3 (2 m^2/g) and thus preferable for the adsorption-photodegradation process.

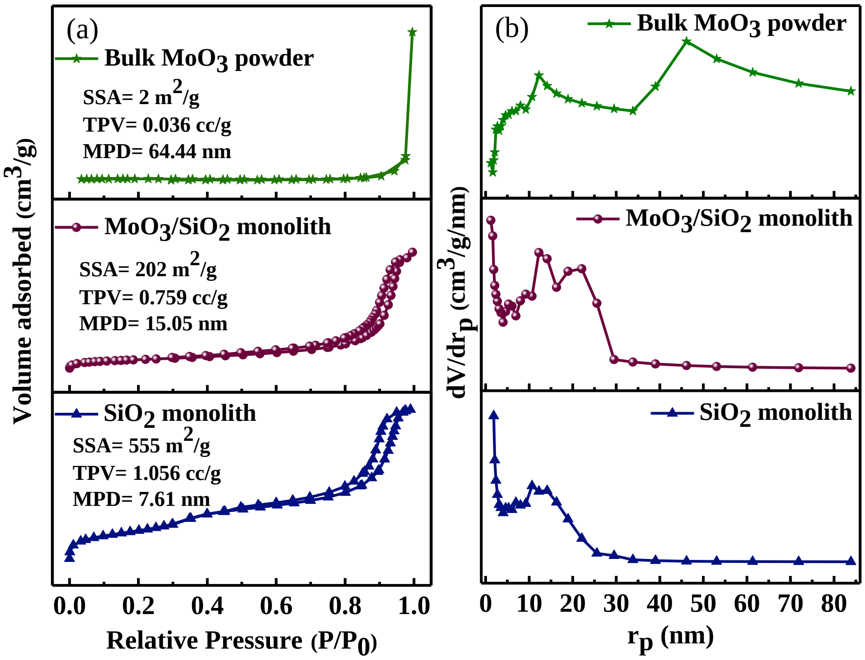

Fig. 4.1. (a) Nitrogen sorption isotherms and **(b)** BJH plot for catalysts (SSA= specific surface area; TPV= total pore volume; MPD= mean pore diameter).

4.3.2 XPS analysis

The oxidation states of different elements in MoO_3/SiO_2 monolith were investigated through XPS analysis. **Fig. 4.2(a)** displays a typical survey spectrum for MoO_3/SiO_2 monolith and the peaks corresponding to oxygen, silicon and molybdenum are present. The appearance of C 1s could be attributed to the adventitious carbon from the instrument. The deconvolution of peaks was done using Gaussian fit program. A single de-convoluted peak at 103.8 eV displayed in **Fig. 4.2(b)** corresponds to Si 2p and can be accredited to SiO_2.[14] **Fig. 4.2(c)** represents the de-convoluted peaks for O 1s at 530.2 and 533.1 eV that can be ascribed to O^{2-} anions,[15] and SiO_2,[16] respectively. The de-convoluted asymmetric peaks for Mo 3d are exhibited in **Fig. 4.2(d)**; the peak obtained at 232.6 eV corresponds to Mo^{6+} $3d_{5/2}$ while the one at 235.8 eV corresponds to Mo^{6+} $3d_{3/2}$.[17] The formation of MoO_3/SiO_2 was confirmed from these observations.

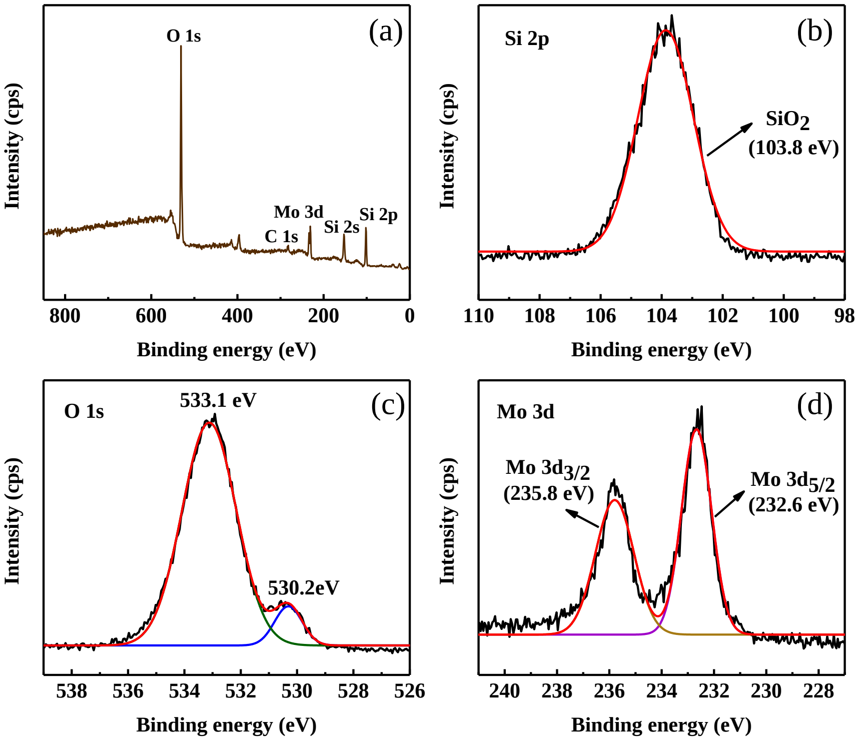

Fig. 4.2. XPS spectra of MoO_3/SiO_2 monolith; **(a)** survey spectrum, **(b)** Si 2p, **(c)** O 1s, and **(d)** Mo 3d.

4.3.3 XRD analysis

The XRD patterns of fabricated materials are displayed in **Fig. 4.3(a)**. The broad peak at 22.3^{o} affirms the construction of amorphous SiO_2 monolith.[18] In the case of MoO_3/SiO_2 monoliths, a broad peak centered at 22^{o} appeared owing to the presence of amorphous SiO_2. The additional diffraction peaks matched with bulk MoO_3 powder (JCPDS card No. 05-0508) were found at 2Θ ~12.76^{o} (020), 23.43^{o} (110), 25.68^{o} (040), 27.38^{o} (021), 29.63^{o} (130), 33.04^{o} (101), 33.78^{o} (111), 35.5^{o} (041), 39.01^{o} (060), 39.60^{o} (150), 45.73^{o} (200), 46.27^{o} (210), 49.20^{o} (002), 52.78^{o} (211), 54.17^{o} (221), 55.28^{o} (112), 56.30^{o} (042), 57.60^{o} (171), and 58.86^{o} (081). It suggests that the SiO_2 monolith is loaded with MoO_3 and thus the formation of pure MoO_3/SiO_2 monolith is confirmed.

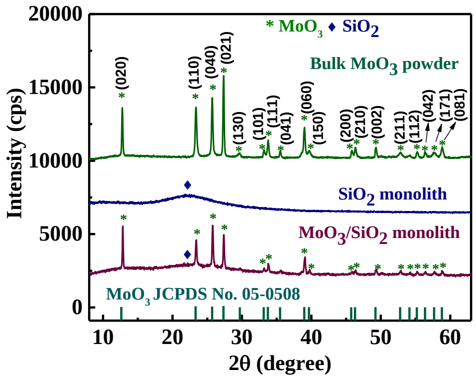

Fig. 4.3. XRD analysis of the prepared materials.

4.3.4 EDS-Color mapping

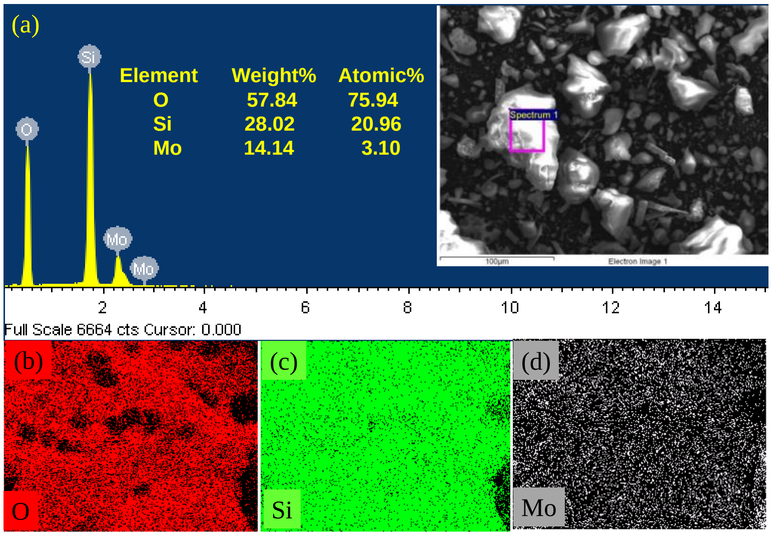

Element	Weight%	Atomic%
O	57.84	75.94
Si	28.02	20.96
Mo	14.14	3.10

Fig. 4.4. (a) EDS spectra and **(b-d)** color mapping images of different elements in MoO_3/SiO_2 monoliths.

The constituent elements of as-synthesized monolith were analyzed through EDS analysis and elemental X-ray mapping. The EDS spectra of MoO_3/SiO_2 monolith asserts the occurrence of O, Si, and Mo as shown in **Fig. 4.4(a)**. The elemental X-ray mapping **(Fig. 4.4(b-d))** exhibited a uniform dispersal of the elements indicating that precursor i.e., ammonium molybdate is homogeneously dispersed throughout the SiO_2 monoliths.

4.3.5 FESEM and HRTEM analyses

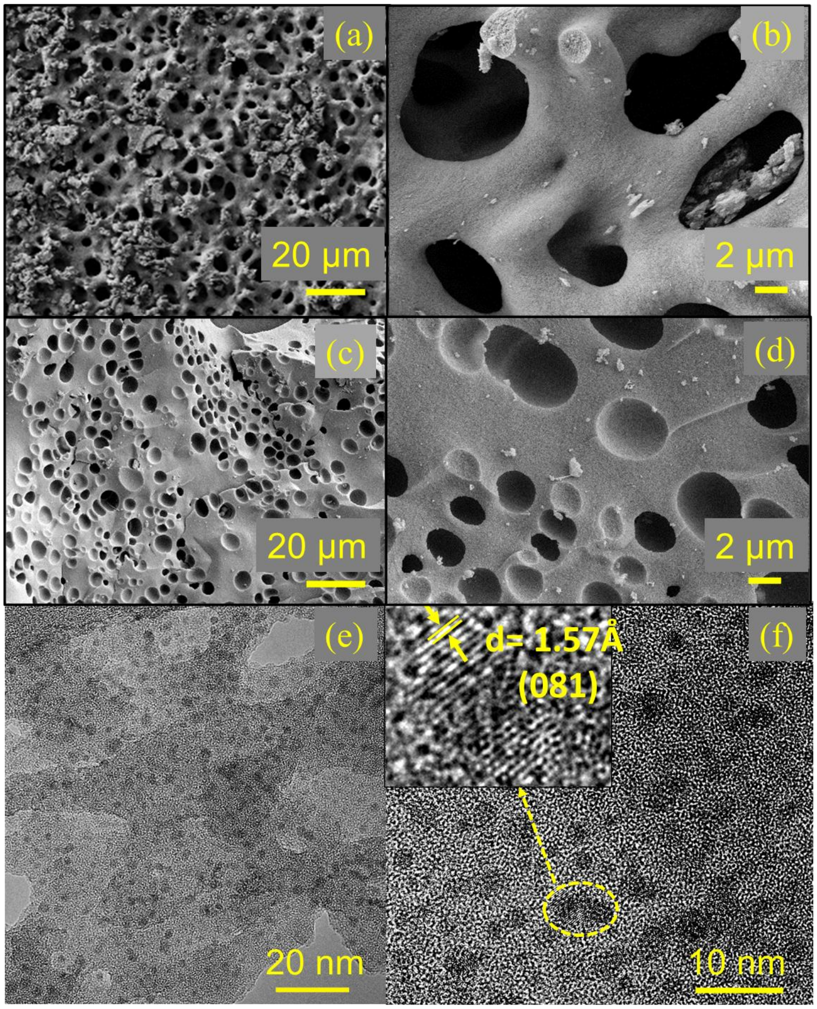

Fig. 4.5. FESEM images of **(a-b)** SiO_2 and **(c-d)** MoO_3/SiO_2 monoliths; **(e-f)** HRTEM images of MoO_3/SiO_2 monoliths.

The morphological details of the prepared-monoliths were assessed through FESEM analyses. The SiO_2 monoliths had a connected network porous structure **(Fig. 4.5(a-b))**. It is evident from **Fig. 4.5(c-d)** that the MoO_3/SiO_2 monoliths are highly porous and have suitability for efficacious adsorption and photocatalysis. HRTEM images **(Fig. 4.5(e-f))** show the formation of MoO_3 (darker particles) over the SiO_2 monoliths. The inset of **Fig. 4.5(f)** (containing magnified view) shows the presence of 1.57 Å lattice spacing that can be accredited to (081) crystal plane of MoO_3 which matches with the XRD pattern (JCPDS card No. 05-0508).

4.3.6 Optical properties

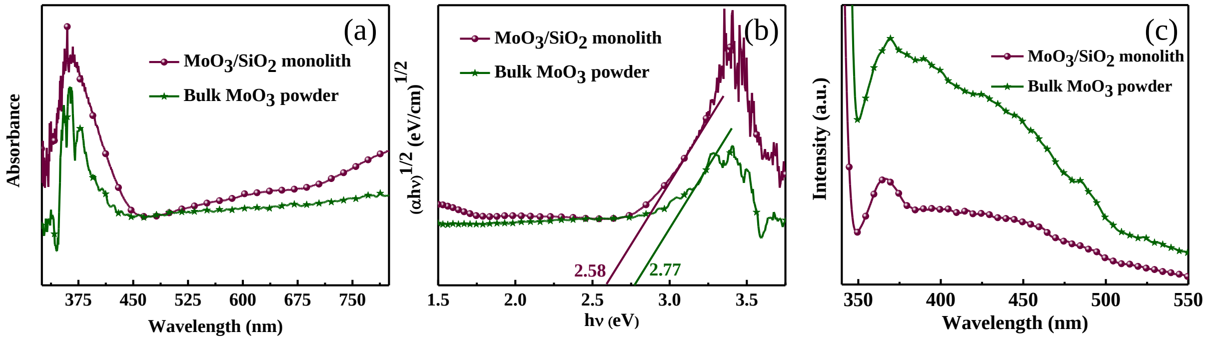

Fig. 4.6. (a) UV-Vis DRS, **(b)** Tauc plot, and **(c)** PL spectra for MoO_3/SiO_2 monolith.

An efficient photocatalyst must have supreme light-harvesting properties and a narrow band gap in addition to a low recombination rate of photogenerated electron-hole (e^-/h^+) pairs and better charge separation and transfer.[19,20] The UV-visible DRS technique was utilized to evaluate the absorption range of prepared catalysts. The absorption edge of MoO_3/SiO_2 monolith is around 480 nm and it can therefore absorb in the visible region **(Fig. 4.6(a))**. Furthermore, the band gap energies of the materials were calculated through Tauc's equation (**Eq. (2.2), chapter 2).** The band gap energies of MoO_3/SiO_2 monolith and bulk MoO_3 powder were found to be 2.58 and 2.77 eV, respectively **(Fig. 4.6(b))**. The PL emission spectra of the synthesized catalysts were determined at an excitation wavelength of 325 nm **(Fig. 4.6(c))**. The exciton recombination has a direct correlation with the PL emission signal. Lower the PL intensity, slower the recombination rate and better the charge separation. The PL intensity of bulk MoO_3 powder was higher in comparison to MoO_3/SiO_2 monolith implying an improved charge separation besides a low recombination rate of e^-/h^+ in the latter.[21] This is probably because of the heterojunction formed amongst MoO_3 and SiO_2 and the e^- transport facilitates the reduction of the recombination of charges.[22] There is a possibility of the excitation of e^- at the surface states of SiO_2 in visible irradiation encouraging the separation along with transfer of photogenerated e^- and h^+.[23] Thus, the as-prepared MoO_3/SiO_2 monoliths have favorable optical properties which render them suitable for visible light-driven photocatalysis.

4.3.7 Photocatalytic activity

The photoactivity of MoO_3/SiO_2 monolith was evaluated through the photodegradation of Rh-B dye and colorless antibiotic MZ. The photolysis of Rh-B **(Fig. 4.7(a))** and MZ **(Fig. 4.7(b))** (without catalyst) under visible light manifested ~14% and 27.6% degradation in 150 and 180 min, respectively. The photocatalytic degradation of Rh-B and MZ using 0.3 and 0.1 g/L MoO_3/SiO_2 monolith exhibited 88.6% and 67.4% photodegradation, respectively **(Fig. 4.7(a-b))**.

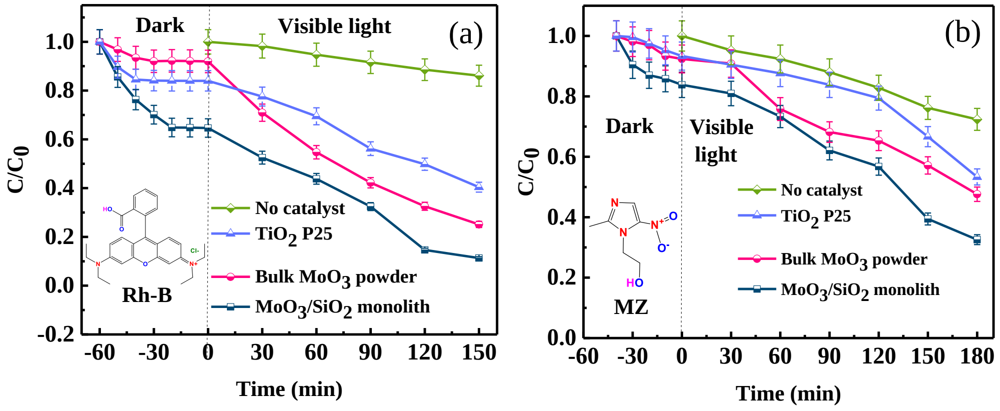

Fig. 4.7. Plot showing kinetic analysis for **(a)** Rh-B degradation and **(b)** MZ degradation.

A comparison was drawn between the photoactivity of the prepared monolith with bulk MoO_3 powder and commercial TiO_2 P25 powder and the as-synthesized monolith demonstrated supreme activity **(Table 4.1)**.

Table 4.1. Degradation parameters of pollutants using different catalysts under visible light.

Material	Rh-B		MZ	
	% Degradation	Rate constant (min^{-1})	% Degradation	Rate constant (min^{-1})
No catalyst	14	0.0010	27.6	0.0018
Bulk MoO_3powder	75	0.0087	52	0.0036
TiO_2 P25	60	0.0049	47	0.0028
MoO_3/SiO_2 monolith	88.6	0.0129	67.4	0.0054

The rate constant was evaluated after the kinetic studies through **Eq. (2.3)** mentioned in **Chapter 2**. The reaction obeys pseudo-first order and the rate constant values were 0.0129 min^{-1} for Rh-B degradation **(Fig. 4.8(a))** while 0.0054 min^{-1} for MZ degradation by MoO_3/SiO_2 monolith **(Fig. 4.8(b))** and the values were higher in comparison to bulk MoO_3 powder and P25 as listed in **Table 4.1**.

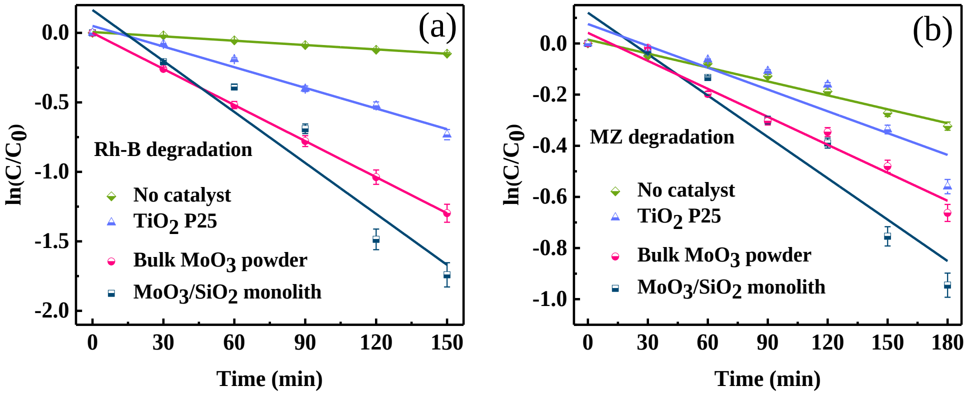

Fig. 4.8. Linear fit plot for **(a)** Rh-B degradation and **(b)** MZ degradation.

A synergy factor (R) was evaluated by **Eq. (4.3)** for quantifying the degree of synergy effect of MoO_3/SiO_2 composite as compared to pure MoO_3.[24]

$$R = k_{MoO3/SiO2} / k_{MoO3} \qquad (4.3)$$

The value of R was calculated to be ~1.5 for MZ degradation and ~1.4 for Rh-B degradation which demonstrates the synergistic effect amongst MoO_3 and SiO_2 in the photodegradation process.

4.3.7.1 Effect of catalyst concentration

The catalyst concentration was optimized by performing the photocatalytic treatment with various catalyst concentrations (0.025, 0.05, 0.1, 0.3, and 0.5 g/L) **(Fig. 4.9(a))**. The greatest removal was achieved at 0.3 g/L in the case of Rh-B and 0.1 g/L for MZ and there was a decrease thereafter because of the opaqueness of solution and blocking of active sites.[25]

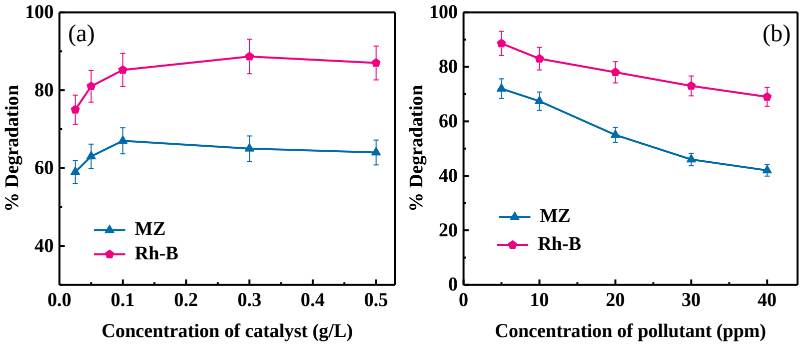

Fig. 4.9. Effect of **(a)** catalyst concentration and **(b)** pollutant concentration on the photodegradation of Rh-B and MZ.

4.3.7.2 Effect of pollutant concentration

The influence of the concentration of the pollutant was examined and it was observed that degradation efficiency dropped as the concentration of MZ and Rh-B increased from 5 to 40 ppm **(Fig. 4.9(b)).** This is because, at a fixed catalytic dose, a greater number of pollutants compete for a fixed number of active sites resulting in reduced efficacy.[26]

4.3.7.3 Effect of pH

The influence of pH on the photocatalytic degradation of MZ and Rh-B was investigated across ranges {1, 3, 5, 6.9 (natural pH), 9, and 11}. The pH variations can be accredited to the surface charge of catalyst at different pH values along with electrical charges of pollutant. The point of zero charge (pzc) on the MoO_3/SiO_2 surface was estimated at pH 8.5[27] **(Fig. 4.10(a))**. $M{-}O^-$ (M is metal) is the major species on the oxide surface at pH> 8.5, which is beneficial for adsorbing of cationic species whereas at pH<8.5, the primary species is $M{-}OH_2^+$ favoring adsorption of anionic species. As displayed in **Fig. 4.10(b)**, the degradation efficiencies at natural pH were found to be ~88.6 % and 67.4% for Rh-B and MZ, respectively.

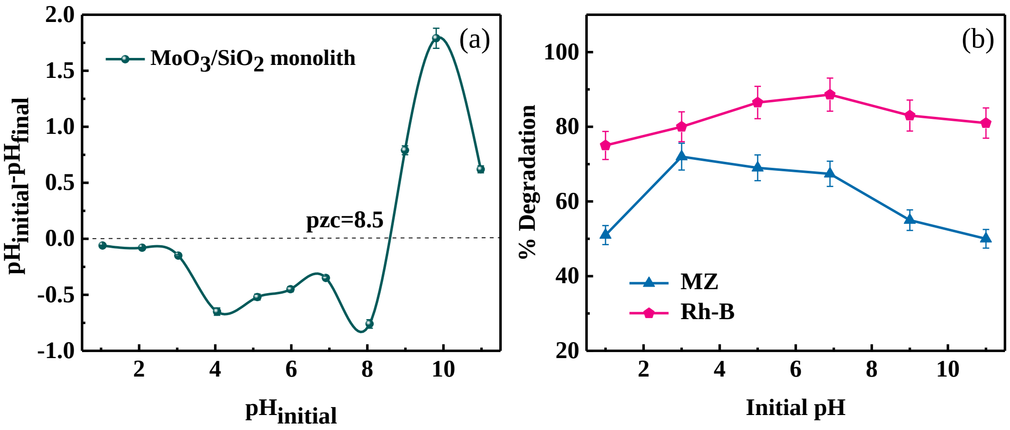

Fig. 4.10. Plot showing **(a)** pzc studies and **(b)** effect of pH on the photodegradation of Rh-B and MZ using MoO_3/SiO_2 monolith.

In the case of Rh-B, maximum removal was attained in the neutral range. In aqueous media, Rh-B exists in cationic form (Rh-B^+) at pH<3.7 ($pka_{Rh\text{-}B}$) and in zwitterionic form (Rh-$B^{\pm}$) at pH>3.7 attributing to the carboxyl group deprotonation. In the range of pH 1 to 3, the cationic surface of Rh-B repels the positively charged catalyst surface leading to low efficiency. Above this range, degradation efficiency increases due to electrostatic attraction among catalyst and Rh-$B^{\pm}$ and maximum efficiency was achieved at natural pH (6.9). At pH>8.5, there is again a decline in the efficacy owing to repulsion amongst negatively charged catalyst surface and Rh-$B^{\pm}$.[28] In the case of MZ, degradation was facilitated in the range of pH 3-7 and the supreme efficacy of 72% was obtained at pH 3. The pKa of MZ is reported to be 2.55 and it exists in protonated form at pH<2.55 ($MZ\text{-}H^+$) thereby repelling positive surface of catalyst.[29] At 8.5>pH>2.55, species $MZ{-}OH^-$ and $M{-}OH_2^+$ are attracted and thus better adsorption occurs.[30] As the pH range changes to alkaline region (pH ~9), there is a poor efficiency due to repulsion amongst anionic surfaces. At highly basic pH, the % degradation decreases in both cases as dissolution of monolithic surface starts and the metal hydroxide precipitates on the surface.[31] This optimum concentration and natural pH (6.9) were used in further experiments to avoid the use of any harsh chemicals. For comparing the activity of as-prepared monolith with the ones prepared in previous chapters, the activity for degradation of MB dye at optimum conditions was also noted which was ~87.3%.

4.3.7.4 Effect of illumination area

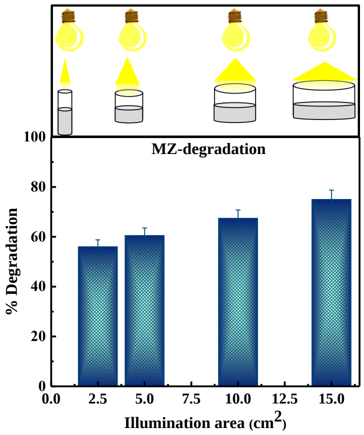

Fig. 4.11. Effect of illumination area on the photodegradation of MZ by MoO_3/SiO_2 monolith.

To study the function of total effective illumination area on the photodegradation of MZ, stirring of the same volume of MZ solution with fixed catalyst concentration (0.1 g/L) was done in reaction vessels with varying diameters. The area of the solution coming in contact with the light directly was thereby different (~2.5, 5, 10, and 12.5 cm^2). A fixed gap of around 10 cm was kept amongst the lamp and the uppermost layer of the solution in all experiments. The efficacy accelerated with the increase in illumination area of the reactor (area of t6he solution in contact with the visible light) as displayed in **Fig. 4.11**.

4.3.7.5 Effect of light source

The experiment under optimal conditions was also performed in natural sunlight. About 91% efficiency (in 150 min) and a rate constant value of 0.0136 min^{-1} in the case of Rh-B while ~75% photodegradation (in 180 min) with a rate constant value of 0.0067 min^{-1} in the case of MZ was achieved **(Fig. 4.12)**. It can be inferred that even a small dose of MoO_3/SiO_2 is quite effective for the degradation process in solar radiation.

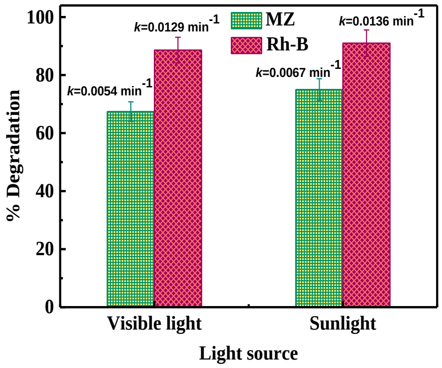

Fig. 4.12. Effect of light sources on the photodegradation of Rh-B and MZ by MoO_3/SiO_2 monolith.

4.3.8 Plausible mechanism

Scavenger tests were executed to find out the active species having a pivotal role in the degradation process. Different scavengers i.e., methanol, DMSO, and benzoquinone were employed for the trapping of h^+, hydroxyl radicals ($^\bullet OH$), and superoxide radicals ($O_2^{\bullet -}$), respectively.[32] It is evident from **(Fig. 4.13)** that maximum inhibition in both the MZ and Rh-B degradation processes was due to methanol (h^+ scavenger). Therefore, holes have a dominant role in the process.

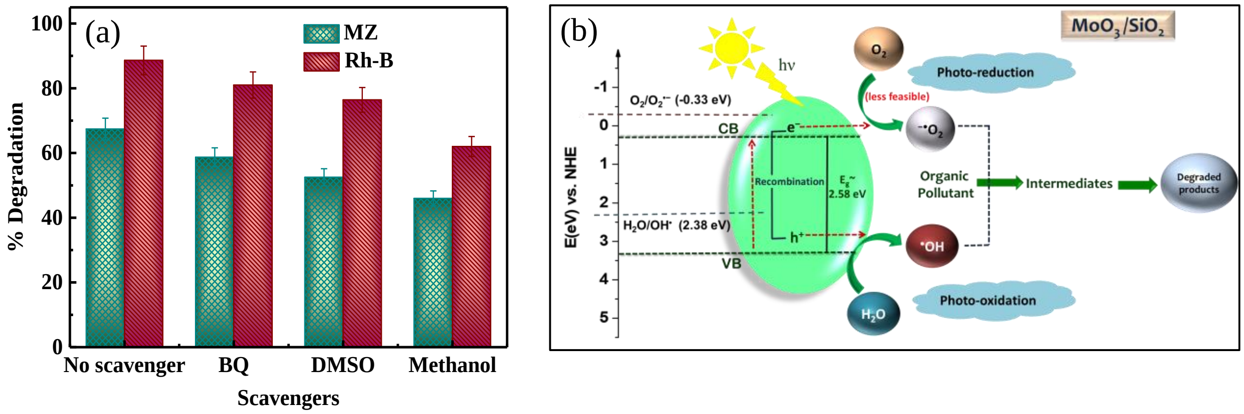

Fig. 4.13. (a) Effect of various scavengers on the photocatalytic degradation of Rh-B and MZ and **(b)** Mechanism for the photodegradation of pollutants by MoO_3/SiO_2 monolith.

In the presence of light, MoO_3/SiO_2 monolith absorbs photons ($h\nu \geq E_g$) causing excitation of e^- from VB to CB and generating h^+ in VB. The reported approximate VB and CB band positions for MoO_3 in literature are 3.32 eV and 0.47 eV, respectively.[9] The VB edge potential is more positive than oxidation potential of $H_2O/{}^\bullet OH$ (2.38 eV) which affirmed that h^+ can oxidize H_2O to ${}^\bullet OH$. However, the single-electron reduction of oxygen $O_2/O_2^{\bullet-}$ (−0.33 eV) is not feasible.[10] This confirmed that holes had a major role in the mechanism. These reactive species react with the pollutant and carry forward the degradation process **Fig. 4.13(b)**. The possible reaction steps involved in the mechanism are presented in **Eq. (4.4) – Eq. (4.8)**.

$$MoO_3/SiO_2 + h\nu \rightarrow e^- + h^+ \quad (4.4)$$

$$H_2O + h^+ \rightarrow H_2O^+ \quad (4.5)$$

$$H_2O^+ \rightarrow {}^\bullet OH + H^+ \quad (4.6)$$

$$O_2 + e^- \rightarrow O_2^{\bullet-} \quad (4.7)$$

$${}^\bullet OH/\ O_2^{\bullet-} + MZ/Rh\text{-}B \rightarrow \text{intermediates} \rightarrow \text{degraded products} \quad (4.8)$$

4.3.9 Comparison with literature

A comparative study of the prepared monolith with recently reported photocatalysts for the degradation of different pollutants is shown in **Table 4.2**. MZ degradation has evidently not been previously examined by MoO_3/SiO_2 catalyst in sunlight.

Table 4.2. Comparison of different photocatalysts for pollutant photodegradation.

Catalyst	Pollutant conc.	Catalyst conc. (g/L)	Time (min)	Light source	Light intensity	% degradation	Rate constant *k* (min^{-1})	Ref.
$BaTiO_3/MoO_3$ layers	Rh-B (0.5 mM)	N/A	60	Visible light (150 W halogen lamp)	-	86	0.0286	[7]
$g\text{-}C_3N_4/MoO_3$	Rh-B (10 ppm)	0.3	120	Visible light (250 W Xe lamp)	-	71.86	-	[33]
$MoO_3/CoFe_2O_4$	Rh-B (5 ppm)	N/A	120	Visible light (200 W low pressure lamp)	-	54	-	[34]
Phosphorus-doped $g\text{-}C_3N_4$ /Co_3O4 quantum dots	MZ (10 ppm)	1	180	Visible light (250 W Xe lamp)	-	68.9	0.0064	[35]
$CuBi_2O_4/CuO$	MZ (50 ppm)	1	120	Simulated solar light (150 W Xe lamp)	100 mW cm^{-2}	36	-	[36]
$CoFe_2O_4$@methylcellulose	MZ (5 ppm)	0.67	120	UV light (6 W lamp)	-	85.3	0.0087	[37]
MoO_3/SiO_2 monolith	Rh-B (5 ppm)	0.3	150	Visible light (45 W CFL lamp)	10 mW cm^{-2}	88.6	0.0129	This study
MoO_3/SiO_2 monolith	MZ (10 ppm)	0.1	180	Visible light (45 W CFL lamp)	10 mW cm^{-2}	67.4	0.0054	This study

4.3.10 Reusability studies

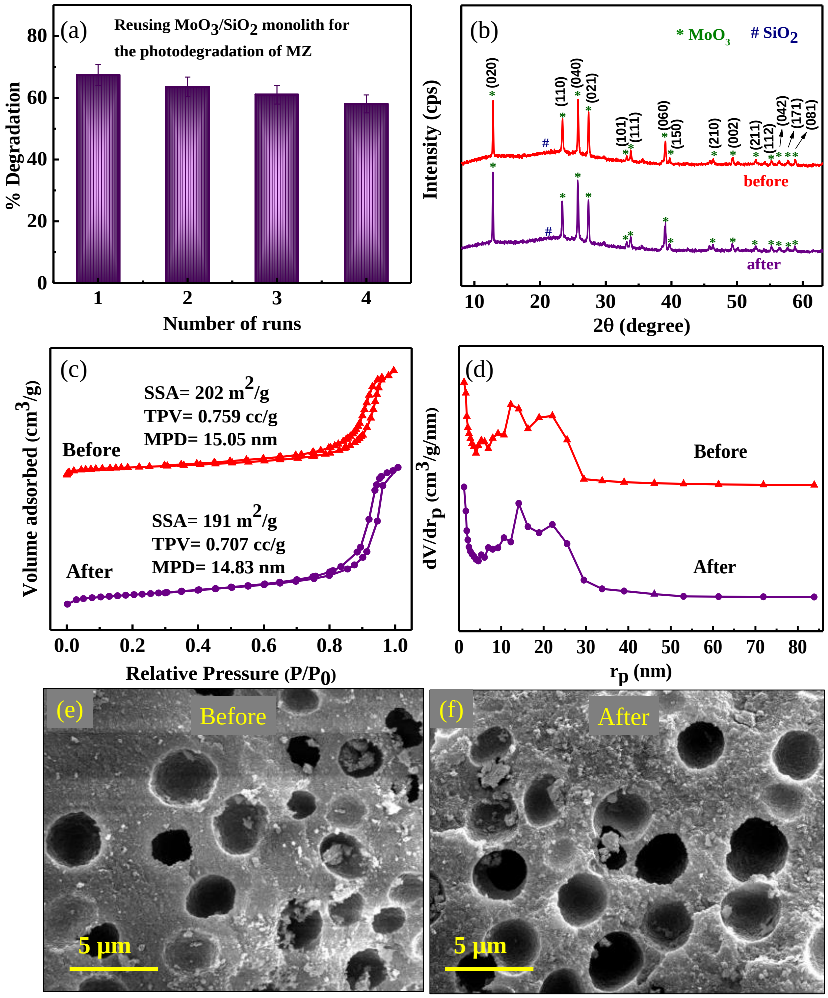

Fig. 4.14. (a) Reusability experiment, **(b)** XRD, **(c)** N_2 sorption isotherms, **(d)** BJH plot, and **(e-f)** SEM images of MoO_3/SiO_2 monolith before and after photocatalytic reaction.

Photocatalyst lifetime holds immense significance considering the practical large-scale application. Thereby, it is imperative to examine the photocatalytic stability of the material for several degradation cycles. The biggest advantage of the MoO_3/SiO_2 monolith is its easy recovery that can be attributed to its solid rock-like structure. After the photocatalytic reaction, the photocatalyst was washed using double distilled water thoroughly and dried at 40 °C. The reusability was analyzed for four continuous cycles in the MZ degradation under optimum conditions. The photocatalytic efficiency decreased by ~9% **(Fig. 4.14a)**. The XRD diffraction peaks were intact after the reaction **(Fig. 4.14b)**. **Fig. 4.14(c)** shows the N_2 sorption isotherms while **(Fig. 4.14(d))** displays BJH plot for the monolithic photocatalyst before and after photodegradation. Type IV isotherm and BJH plot confirmed that the mesoporous nature was maintained after the reaction. The surface morphology of as-prepared monolith was also not much disturbed after the photocatalytic reaction which was validated through SEM analysis **Fig. 4.14(e-f)**.

4.3.11 GC-MS analysis

For the identification of intermediates and products in the photodegradation reaction of MZ, GC-MS analysis was carried out. The GC chromatogram and mass spectrum of MZ after treatment are shown in **Fig. 4.15 (a)** and **(b)**, respectively.

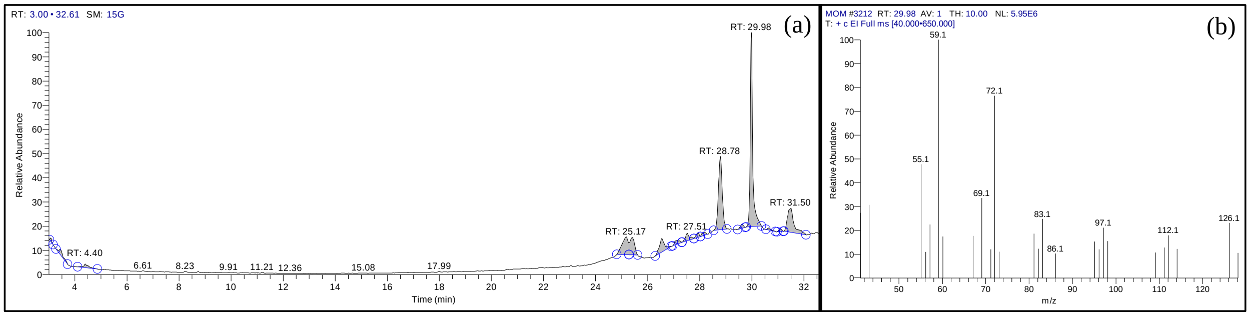

Fig. 4.15. (a) GC chromatogram of MZ after photodegradation and **(b)** MS spectra of MZ after photodegradation at retention time of 29.98 min.

The proposed degradation pathway has been displayed in **Scheme 4.2**. MZ might convert to 2-(2-methyl-1H-imidazol-1-yl)ethan-1-ol [M+]+ via denitration which could then transform into 2-methyl-1H-imidazol-5-ol by the hydroxyl attack and hydroxyethyl group cleavage. This compound could produce 1H-imidazole [M+H]+ via loss of nitrate ion or nitrogen while the breaking of imidazole moiety could form 4-amino-4-oxobut-2-enoic acid which later decomposes to prop-2-en-1-ol [M+H]+. On the other hand, the hydroxyethyl cleavage of metronidazole forms 2-methyl-5-nitro-1H-imidazole which undergoes nitro group reduction to form 2-methyl-1H-imidazol-5-amine, whereas on hydroxyl attack, it forms 2-methyl-1H-imidazole-4,5-dione [M+]+. The latter compound can form N-ethylideneformamide [M+H]+ upon ring cleavage. These compounds can further decompose to simpler hydrocarbons. The findings were in accordance with the literature reports.[3,38–40]

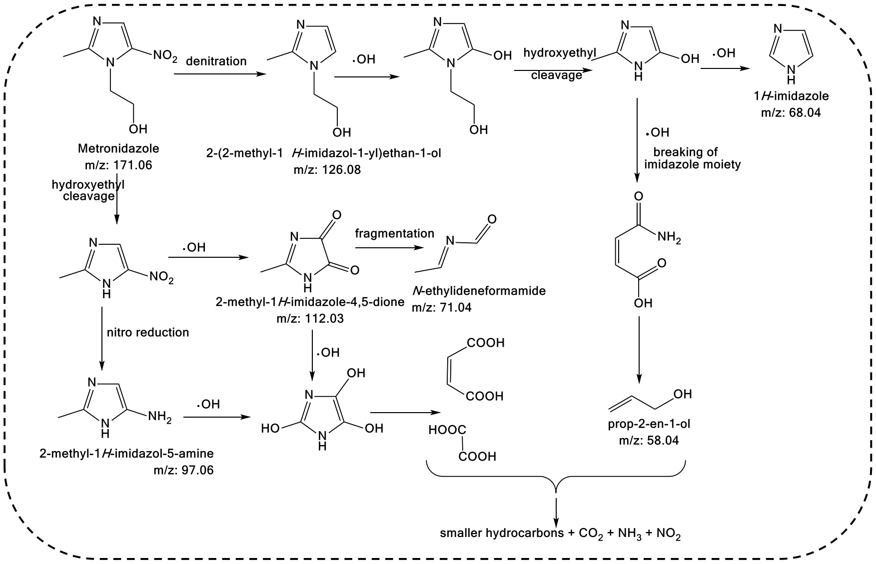

Scheme 4.2. Possible degradation pathway of MZ by MoO_3/SiO_2 monoliths.

4.3.12 Photocatalytic treatment of raw wastewater

The real wastewater was treated by MoO_3/SiO_2 monolith to gauge its efficacy. The raw wastewater effluent had high turbidity and had a strong grey color, indicating a high proportion of organic matter. Photocatalytic treatment was performed under the following conditions: 0.3 g/L monoliths; natural pH; time=150 min. The %COD and %TOC removal of industrial wastewater was ~64% and 57%, respectively **(Fig. 4.16)**. The high turbidity content inhibits the infiltration of adequate light energy and catalyst for the degradation of recalcitrant organics in the effluent as the treatment was done without any physicochemical pretreatment.[41] The removal efficiency is still high validating the effectiveness of the MoO_3/SiO_2 monolith.

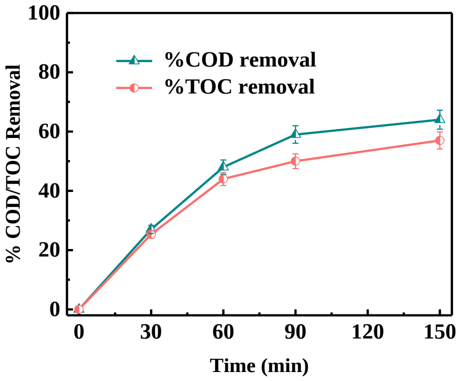

Fig. 4.16. COD and TOC analysis of raw wastewater.

4.4. Conclusions

In this chapter, mesoporous and reusable visible-light-driven MoO_3/SiO_2 monoliths were constructed through wet impregnation method and were tested for the photocatalytic degradation of model dye Rh-B and pharmaceutical pollutant MZ. The monoliths had a high surface area and favorable optical properties for effective photocatalytic activity. Various parameters namely solution pH, catalyst and pollutant concentration, and illumination area were examined. The degradation was also quite effectual in natural sunlight even at a very low catalyst dose. The predominant role of holes in the photodegradation process was confirmed by scavenger studies. The easy recovery of monolithic photocatalyst is one of its top advantages that was reasserted by reusability studies. The characterization results after the photocatalytic reaction revealed that the monolith retained its crystallinity, surface area and porous morphology. The intermediate products obtained after the photodegradation of MZ were analyzed through GC–MS analysis. Photocatalytic treatment of real wastewater by the monoliths unveiled its effectiveness through substantial %COD and %TOC removal in the absence of any physicochemical treatment. The investigation asserted that easily-recoverable and economical MoO_3/SiO_2 monolith could be competent for large-scale wastewater treatment.

References

(1) Gholami, P.; Khataee, A.; Soltani, R. D. C.; Dinpazhoh, L.; Bhatnagar, A. Photocatalytic Degradation of Gemifloxacin Antibiotic Using Zn-Co-LDH@biochar Nanocomposite. *J. Hazard. Mater.* **2020**, *382*, 121070. https://doi.org/10.1016/j.jhazmat.2019.121070.

(2) Cao, J.; Li, J.; Chu, W.; Cen, W. Facile Synthesis of Mn-Doped BiOCl for Metronidazole Photodegradation: Optimization, Degradation Pathway, and Mechanism. *Chem. Eng. J.* **2020**, *400*, 125813. https://doi.org/10.1016/j.cej.2020.125813.

(3) Martins, P. M.; Salazar, H.; Aoudjit, L.; Gonçalves, R.; Zioui, D.; Fidalgo-Marijuan, A.; Costa, C. M.; Ferdov, S.; Lanceros-Mendez, S. Crystal Morphology Control of Synthetic Giniite for Enhanced Photo-Fenton Activity against the Emerging Pollutant Metronidazole. *Chemosphere* **2021**, *262*, 128300. https://doi.org/10.1016/j.chemosphere.2020.128300.

(4) Khamparia, S.; Jaspal, D. K. Xanthium Strumarium L. Seed Hull as a Zero Cost Alternative for Rhodamine B Dye Removal. *J. Environ. Manage.* **2017**, *197*, 498–506. https://doi.org/10.1016/j.jenvman.2017.03.099.

(5) Baldev, E.; MubarakAli, D.; Ilavarasi, A.; Pandiaraj, D.; Ishack, K. A. S. S.; Thajuddin, N. Degradation of Synthetic Dye, Rhodamine B to Environmentally Non-Toxic Products Using Microalgae. *Colloids Surfaces B Biointerfaces* **2013**, *105*, 207–214. https://doi.org/10.1016/j.colsurfb.2013.01.008.

(6) Liu, H.; Lv, T.; Zhu, C.; Zhu, Z. Direct Bandgap Narrowing of TiO_2/MoO_3 Heterostructure Composites for Enhanced Solar-Driven Photocatalytic Activity. *Sol. Energy Mater. Sol. Cells* **2016**, *153*, 1–8. https://doi.org/10.1016/j.solmat.2016.04.013.

(7) Alex, K. V.; Prabhakaran, A.; Jayakrishnan, A. R.; Kamakshi, K.; Silva, J. P. B.; Sekhar, K. C. Charge Coupling Enhanced Photocatalytic Activity of $BaTiO_3$ /MoO_3 Heterostructures. *ACS Appl. Mater. Interfaces* **2019**, *11* (43), 40114–40124. https://doi.org/10.1021/acsami.9b14919.

(8) Salari, H. Efficient Photocatalytic Degradation of Environmental Pollutant with Enhanced Photocarrier Separation in Novel Z-Scheme a-MnO_2 Nanorod/a-MoO_3 Nanocomposites. *J. Photochem. Photobiol. A Chem.* **2020**, *401*, 112787. https://doi.org/10.1016/j.jphotochem.2020.112787.

(9) Liu, Y.; Feng, P.; Wang, Z.; Jiao, X.; Akhtar, F. Novel Fabrication and Enhanced Photocatalytic MB Degradation of Hierarchical Porous Monoliths of MoO_3 Nanoplates. *Sci. Rep.* **2017**, *7* (1), 1845. https://doi.org/10.1038/s41598-017-02025-3.

(10) Salari, H.; Kohantorabi, M. Fabrication of Novel Fe_2O_3/MoO_3/AgBr Nanocomposites with Enhanced Photocatalytic Activity under Visible Light Irradiation for Organic Pollutant Degradation. *Adv. Powder Technol.* **2020**, *31* (1), 493–503. https://doi.org/10.1016/j.apt.2019.11.005.

(11) Shalom, M.; Inal, S.; Neher, D.; Antonietti, M. SiO_2/Carbon Nitride Composite Materials: The Role of Surfaces for Enhanced Photocatalysis. *Catal. Today* **2014**, *225*, 185–190. https://doi.org/10.1016/j.cattod.2013.12.013.

(12) Li, X.; Yu, J.; Jaroniec, M. Hierarchical Photocatalysts. *Chem. Soc. Rev.* **2016**, *45*, 2603–2636. https://doi.org/10.1039/c5cs00838g.

(13) Huang, L.; Xu, H.; Zhang, R.; Cheng, X.; Xia, J.; Xu, Y.; Li, H. Synthesis and Characterization of G-C_3N_4/MoO_3 Photocatalyst with Improved Visible-Light Photoactivity. *Appl. Surf. Sci.* **2013**, *283*, 25–32. https://doi.org/10.1016/j.apsusc.2013.05.106.

(14) Sri Devi Kumari, T.; Jeyakumar, D.; Prem Kumar, T. Nano Silicon Carbide: A New Lithium-Insertion Anode Material on the Horizon. *RSC Adv.* **2013**, *3* (35), 15028–15034. https://doi.org/10.1039/c3ra40798e.

(15) Gajraj, V.; Mariappan, C. R. Electrochemical Performances of Asymmetric Aqueous Supercapacitor Based on Porous $Cu_3Mo_2O_9$ Petals and $La_2Mo_3O_{12}$ Nanoparticles Fabricated through a Simple Co-Precipitation Method. *Appl. Surf. Sci.* **2020**, *512*, 145648. https://doi.org/10.1016/j.apsusc.2020.145648.

(16) Gil, J. .; Ferreira, L. F.; Silva, V. C.; Oliveira, A. C.; de Oliveira, R. R.; Jacinto, M. J. Facile Fabrication of Functionalized Core-Shell Fe_3O_4@SiO_2@Pd Microspheres by Urea-Assisted Hydrothermal Route and Their Application in the Reduction of Nitro Compounds. *Environ. Nanotechnology, Monit. Manag.* **2019**, *11*, 100220. https://doi.org/10.1016/j.enmm.2019.100220.

(17) Su, Y.; Zhao, X.; Bi, Y.; Li, C.; Feng, Y.; Han, X. High-Concentration Organic Dye Removal Using $Fe_2O_3 \cdot 3.9MoO_3$ Nanowires as Fenton-like Catalysts. *Environ. Sci. Nano* **2018**, *5* (9), 2069–2076. https://doi.org/10.1039/c8en00346g.

(18) Wang, W.; Fang, J.; Chen, H. Nano-Confined g-C_3N_4 in Mesoporous SiO_2 with Improved Quantum Size Effect and Tunable Structure for Photocatalytic Tetracycline Antibiotic Degradation. *J. Alloys Compd.* **2020**, *819*, 153064. https://doi.org/10.1016/j.jallcom.2019.153064.

(19) Akhtar, J.; Tahir, M. B.; Sagir, M.; Bamufleh, H. S. Improved Photocatalytic Performance of Gd and Nd Co-Doped ZnO Nanorods for the Degradation of Methylene Blue. *Ceram. Int.* **2020**, *46* (8), 11955–11961. https://doi.org/10.1016/j.ceramint.2020.01.234.

(20) Asadzadeh-Khaneghah, S.; Habibi-Yangjeh, A. G-C_3N_4/Carbon Dot-Based Nanocomposites Serve as Efficacious Photocatalysts for Environmental Purification and Energy Generation: A Review. *J. Clean. Prod.* **2020**, *276*, 124319. https://doi.org/10.1016/j.jclepro.2020.124319.

(21) J. Wang, G. Zhang, K. W. Novel Heterostructured Nanocomposite for Degradation of Tetracycline : Enhanced Visible Light Photocatalytic Activity and Mechanism. *ACS Sustain. Chem. Eng.* **2018**, *6* (11), 14221–14229. https://doi.org/10.1021/acssuschemeng.8b02869.

(22) Yang, L.; Wang, P.; Yin, J.; Wang, C.; Dong, G.; Wang, Y.; Ho, W. Engineering of Reduced Graphene Oxide on Nanosheet–g-C_3N_4/Perylene Imide Heterojunction for Enhanced Photocatalytic Redox Performance. *Appl. Catal. B Environ.* **2019**, *250* (February), 42–51. https://doi.org/10.1016/j.apcatb.2019.02.076.

(23) Hao, Q.; Niu, X.; Nie, C.; Hao, S.; Zou, W.; Ge, J.; Chen, D.; Yao, W. A Highly Efficient G-C_3N_4/SiO_2 Heterojunction: The Role of SiO_2 in the Enhancement of Visible Light Photocatalytic Activity . *Phys. Chem. Chem. Phys.* **2016**, *18* (46), 31410–31418. https://doi.org/10.1039/c6cp06122b.

(24) Wang, R.; Shi, K.; Huang, D.; Zhang, J.; An, S. Synthesis and Degradation Kinetics of TiO_2/GO Composites with Highly Efficient Activity for Adsorption and Photocatalytic Degradation of MB. *Sci. Rep.* **2019**, *9* (1), 18744. https://doi.org/10.1038/s41598-019-54320-w.

(25) Aanchal; Barman, S.; Basu, S. Complete Removal of Endocrine Disrupting Compound and Toxic Dye by Visible Light Active Porous G-C_3N_4/H-ZSM-5 Nanocomposite. *Chemosphere* **2020**, *241*, 124981. https://doi.org/10.1016/j.chemosphere.2019.124981.

(26) Surenjan, A.; Sambandam, B.; Pradeep, T.; Philip, L. Synthesis, Characterization and Performance of Visible Light Active C-TiO_2 for Pharmaceutical Photodegradation. *J. Environ. Chem. Eng.* **2017**, *5* (1), 757–767. https://doi.org/10.1016/j.jece.2016.12.044.

(27) Lam, S. M.; Sin, J. C.; Abdullah, A. Z.; Mohamed, A. R. Investigation on Visible-Light Photocatalytic Degradation of 2,4-Dichlorophenoxyacetic Acid in the Presence of MoO_3/ZnO Nanorod Composites. *J. Mol. Catal. A Chem.* **2013**, *370*, 123–131. https://doi.org/10.1016/j.molcata.2013.01.005.

(28) Xiao, W.; Garba, Z. N.; Sun, S.; Lawan, I.; Wang, L.; Lin, M.; Yuan, Z. Preparation and Evaluation of an Effective Activated Carbon from White Sugar for the Adsorption of Rhodamine B Dye. *J. Clean. Prod.* **2020**, *253*, 119989. https://doi.org/10.1016/j.jclepro.2020.119989.

(29) Nasseh, N.; Barikbin, B.; Taghavi, L.; Nasseri, M. A. Adsorption of Metronidazole Antibiotic Using a New Magnetic Nanocomposite from Simulated Wastewater (Isotherm, Kinetic and Thermodynamic Studies). *Compos. Part B Eng.* **2019**, *159*, 146–156. https://doi.org/10.1016/j.compositesb.2018.09.034.

(30) Bashiri, F.; Khezri, S. M.; Kalantary, R. R.; Kakavandi, B. Enhanced Photocatalytic

Degradation of Metronidazole by TiO_2 Decorated on Magnetic Reduced Graphene Oxide: Characterization, Optimization and Reaction Mechanism Studies. *J. Mol. Liq.* **2020**, *314*, 113608. https://doi.org/10.1016/j.molliq.2020.113608.

(31) Sharma, M.; Singh, J.; Basu, S. Efficient Metal Ion Adsorption and Photodegradation of Rhodamine-B by Hierarchical Porous Fe-Ni@SiO_2 Monolith. *Microchem. J.* **2019**, *145* (November 2018), 708–717. https://doi.org/10.1016/j.microc.2018.11.042.

(32) Sedaghati, N.; Habibi-Yangjeh, A.; Pirhashemi, M.; Asadzadeh-Khaneghah, S.; Ghosh, S. Integration of BiOI and Ag_3PO_4 Nanoparticles onto Oxygen Vacancy Rich-TiO_2 for Efficient Visible-Light Photocatalytic Decontaminations. *J. Photochem. Photobiol. A Chem.* **2020**, *400*, 112659. https://doi.org/10.1016/j.jphotochem.2020.112659.

(33) Zhang, X.; Yi, J.; Chen, H.; Mao, M.; Liu, L.; She, X.; Ji, H.; Wu, X.; Yuan, S.; Xu, H.; et al. Construction of a Few-Layer g-C_3N_4/α-MoO_3 Nanoneedles All-Solid-State Z-Scheme Photocatalytic System for Photocatalytic Degradation. *J. Energy Chem.* **2019**, *29*, 65–71. https://doi.org/10.1016/j.jechem.2018.01.014.

(34) Tariq, N.; Fatima, R.; Zulfiqar, S.; Rahman, A.; Warsi, M. F.; Shakir, I. Synthesis and Characterization of MoO_3/$CoFe_2O_4$ Nanocomposite for Photocatalytic Applications. *Ceram. Int.* **2020**, *46* (13), 21596–21603. https://doi.org/10.1016/j.ceramint.2020.05.264.

(35) Zhao, Z.; Fan, J.; Deng, X.; Liu, J. One-Step Synthesis of Phosphorus-Doped g-C_3N_4/Co_3O_4 Quantum Dots from Vitamin B12 with Enhanced Visible-Light Photocatalytic Activity for Metronidazole Degradation. *Chem. Eng. J.* **2019**, *360*, 1517–1529. https://doi.org/10.1016/j.cej.2018.10.239.

(36) Nogueira, A. C.; Gomes, L. E.; Ferencz, J. A. P.; Rodrigues, J. E. F. S.; Goncąlves, R. V.; Wender, H. Improved Visible Light Photoactivity of $CuBi_2O_4$/CuO Heterojunctions for Photodegradataaion of Methylene Blue and Metronidazole. *J. Phys. Chem. C* **2019**, *123* (42), 25680–25690. https://doi.org/10.1021/acs.jpcc.9b06907.

(37) Nasiri, A.; Tamaddon, F.; Mosslemin, M. H.; Gharaghani, M. A.; Asadipour, A. New Magnetic Nanobiocomposite $CoFe_2O_4$@methycellulose: Facile Synthesis,

Characterization, and Photocatalytic Degradation of Metronidazole. *J. Mater. Sci. Mater. Electron.* **2019**, *30* (9), 8595–8610. https://doi.org/10.1007/s10854-019-01182-7.

(38) Du, W.; Xu, Q.; Jin, D.; Wang, X.; Shu, Y.; Kong, L.; Hu, X. Visible-Light-Induced Photo-Fenton Process for the Facile Degradation of Metronidazole by Fe/Si Codoped TiO_2. *RSC Adv.* **2018**, *8* (70), 40022–40034. https://doi.org/10.1039/c8ra08114j.

(39) Dai, Q.; Zhou, J.; Weng, M.; Luo, X.; Feng, D.; Chen, J. Electrochemical Oxidation Metronidazole with Co Modified PbO_2 Electrode: Degradation and Mechanism. *Sep. Purif. Technol.* **2016**, *166*, 109–116. https://doi.org/10.1016/j.seppur.2016.04.028.

(40) El Bouraie, M. M.; Ibrahim, S. S. Comparative Study Between Metronidazole Residues Disposal by Using Adsorption and Photodegradation Processes onto MgO Nanoparticles. *J. Inorg. Organomet. Polym. Mater.* **2021**, *31* (1), 344–364. https://doi.org/10.1007/s10904-020-01711-6.

(41) Jorfi, S.; Barzegar, G.; Ahmadi, M.; Darvishi Cheshmeh Soltani, R.; Alah Jafarzadeh Haghighifard, N.; Takdastan, A.; Saeedi, R.; Abtahi, M. Enhanced Coagulation-Photocatalytic Treatment of Acid Red 73 Dye and Real Textile Wastewater Using UVA/Synthesized MgO Nanoparticles. *J. Environ. Manage.* **2016**, *177*, 111–118. https://doi.org/10.1016/j.jenvman.2016.04.005.

Chapter 5

Efficient and durable hierarchical porous CuO/SiO$_2$ monolith for synergistically boosting the visible-light-driven degradation of organic pollutants

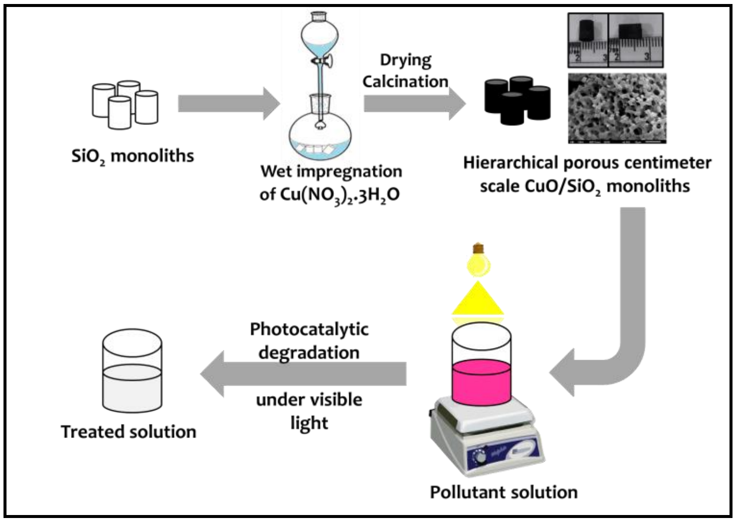

Highlights

- Hierarchical porous CuO/SiO$_2$ monoliths in centimeter-length-scale were prepared via wet impregnation method.
- The photoactivity of the material was tested for the degradation of Rh-B dye and TM insecticide under visible light which were degraded up to 90.5 % (rate constant~ 0.01255 min^{-1}) and 55% (rate constant~ 0.00443 min^{-1}), respectively.
- TOC analysis revealed that ~60.03% of Rh-B and ~ 20.05% of TM was mineralized.
- The characterization results after reaction supported the reusability efficiency of the monoliths.

5.1. Introduction

In this chapter, Rh-B and TM were used as colored and colorless model pollutants, respectively, using copper oxides (CuO) monolith. The toxic effects of Rh-B and TM have been descried in the previous chapters. Copper oxides have gained reputation as they are abundant, chemically stable in aqueous media, have good electrical conductivity along with excellent catalytic properties.[1–3] CuO is a handy photocatalyst that is not only economical but also quite simple to synthesize. It is a p-type semiconductor with narrow band gaps in the range of ~1.2-1.9 eV and can be used under solar light.[4] The theoretical photocurrent of ~35 mA/cm^2 can be produced in the case of CuO which is much greater as compared to Cu_2O (~14.7 mA/cm^2).[5] The estimated CuO has been exploited for heterogeneous catalysis, solar cells, gas sensors, and as electrode material in Li-ion batteries.[6] However, there are inadequate reports discussing the photocatalytic behavior of CuO. The combination of CuO with SiO_2 can aid in avoiding the agglomeration of smaller metal species, ameliorating the net surface area besides the total number of active sites for catalysis.[7] Additionally, under the visible light irradiance, the electrons from the surface states of SiO_2 can get excited from the valence band (VB). This assists the reduction of recombination rate and improves both the separation and transfer of electron-hole (e^-/h^+).[8] Ramya et al.[9] synthesized SiO_2 nanoparticles from rice husk and then doped with CuO nanoparticles. The material was tested for nitrophenol reduction under visible light. Rajabzadeh et al.[10] fabricated CuO@SiO_2 multi-yolk@shell composite such that CuO nanoparticles reside inside hollow SiO_2 nanospheres. The material was utilized for the application of CO_2 fixation process. Xu et al.[3] constructed CuO nanoparticles set in a SiO_2 matrix for the catalytic degradation of dye.

However, there is no report available till date regarding the construction of CuO/SiO_2 monolith via wet impregnation route in SiO_2 monolithic template. This chapter presents the synthesis of CuO/SiO_2 monoliths via the wet impregnation of the precursor metal salt into silica monoliths. The as-prepared monoliths were later utilized for the abatement of textile pollutant Rh-B and colorless insecticide TM. The impact of contaminant-pH, catalyst concentrations, scavengers as well as illumination area was tested. The reusability studies were also carried out and characterization of the material after photocatalysis was also performed.

5.2. Experimental section

This section comprises of the chemicals, materials and the methodologies used for the synthesis of catalysts.

5.2.1. Chemicals and materials

Copper (II) oxide (CuO) nanopowder (<50 nm particle size) were acquired from Sigma-Aldrich. Copper nitrate trihydrate ($Cu(NO_3)_2 \bullet 3H_2O$) was purchased from Loba Chemie. TiO_2 P25 nanopowder was generously gifted by Evonik industries (Hanau, Germany).

5.2.2. Syntheses

5.2.2.1 Synthesis of CuO/SiO_2 monoliths

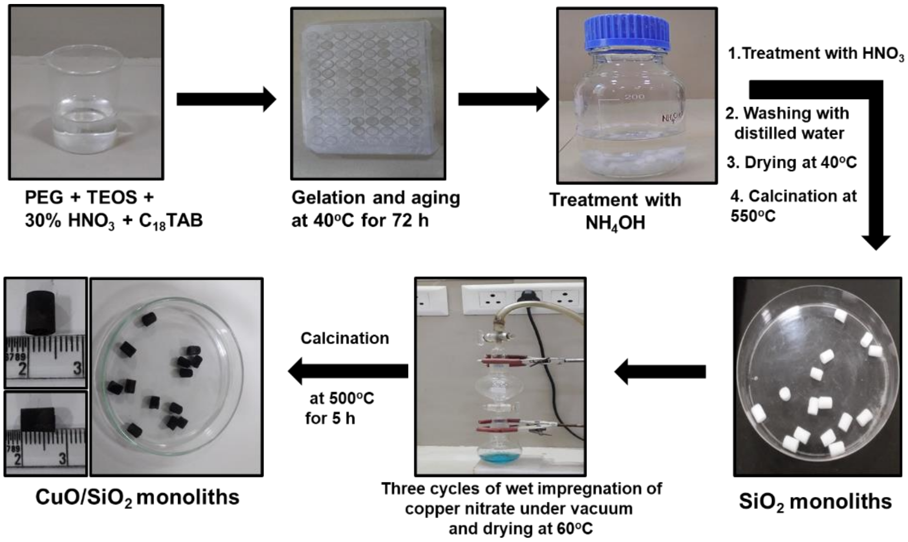

Scheme 5.1. Steps for the synthesis of SiO_2 and CuO/SiO_2 monoliths.

Firstly, the silica monoliths were synthesized as per the procedure described in **Chapter 2 (section 2.2.1)**. To prepare CuO/SiO_2 monoliths, wet impregnation of aqueous solution of copper nitrate trihydrate (concentration~ 0.5 M) was performed by pouring this solution into appropriately degassed SiO_2 monoliths under vacuum followed by drying at 60°C.[11] These steps were repeated thrice for proper impregnation. Finally, monoliths were calcined at 500°C for 5 h at 2 °C /min to acquire black-colored CuO/SiO_2 monoliths that were about 0.7 cm long and 0.5 cm in diameter and the real digital images for the preparation of monoliths are portrayed in **Scheme 5.1**.

5.2.3 Characterization methods

X-ray diffractometer (PANALYTICAL X'Pert PRO) was used for carrying out X-ray diffraction analysis (XRD) with Cu Kα (λ=1.540Å) radiation worked at 45 kV with the diffraction angle ~5-80^o and step size ~0.0260^o. The X-ray photon spectroscopy (XPS) was carried out through PHI-5000 VersaProbe III system. Scanning electron microscope (SEM) images and energy dispersive spectroscopy (EDS) - elemental mapping images were obtained from JEOL JSM-6510 with Oxford INCA operational at 5 kV. Brunauer-Emmett-Teller (BET) theory was used for surface area determination using Microtrac Belsorp Mini-II (Bel, Japan, Inc) surface area analyzer. The pretreatment of materials was conducted in N_2 atmosphere at 100°C for 6 h before the measurement to avoid the undesirable impurities. The pore size distribution was evaluated using Barrett-Joyner-Halenda (BJH) method while micropores were evaluated by MP-plot. UV–Vis diffuse reflectance spectroscopy (DRS) was performed in diffuse absorbance mode employing Hitachi-3900H spectrophotometer. Photoluminescence (PL) analysis was conducted through Perkin Elmer LS-55, USA (PL) spectrometer using 280 nm excitation wavelength. The photocatalytic degradation of the pollutants was observed through Shimadzu UV-2600 spectrophotometer.

5.2.4 Photocatalytic activity

To test the photoactivity of as-synthesized CuO/SiO_2 monoliths, the photocatalytic detoxification of model pollutants i.e., Rh-B dye and colorless insecticide TM was carried out. Approximately 0.25 g/L of the material was taken into a 20 mL aqueous solution of 5 ppm Rh-B. The dark stirring was done for almost 40 min until there was an accomplishment of adsorption-desorption equilibrium. Thereafter, the solution was illuminated with visible radiation using a 45 W Philips bulb (intensity ~100 W/m^2) for 180 min. Likewise, ~0.1 g/L of the monolith was mixed with a 20 mL aqueous solution of 25 ppm TM and stirred in dark for 40 min and then in visible light for 180 min. A constant distance (~10 cm) between the light source and topmost layer of the solution was maintained in all the experiments. The treatment of the pollutants was also done for 180 min in dark (lamp OFF) using the same concentration of catalyst. All experiments were performed three times and the error bars (source of error ~5% of the data) are indicated in all the plots.

The degradation of Rh-B and TM was watched at λ_{max}= 555 and 249 nm, respectively, through a UV–visible spectrophotometer. Degradation efficiency (%D) was evaluated by using **Eq. (2.1)** as discussed in **chapter 2 (section 2.2.4)**. TOC measurements for analyzing the mineralization degree of the pollutants were conducted using a titrimetric method. **Eq. (4.2)** was followed to estimate percentage TOC removal as discussed in **chapter 2 (section 4.2.4)**. For the analysis of degradation products, GC-MS analysis was done. Samples for GC-MS were prepared as follows: The aqueous reaction mixture was collected after the photocatalytic reaction and catalyst was separated. The solvent was removed by drying at 40^{o}C and the residue was dissolved in dichloromethane. Shimadzu QP-2010 Plus with Thermal Desorption System TD 20. Conditions - split mode injector, helium carrier gas (flow rate=1 mL/min), injection volume= 1.21 µL, injector temperature= 260^{o}C, ion source temperature =220^{o}C. The initial oven temperature was 100^{o}C for 2 min hold time and increased to 280 ^{o}C at a ramp of 10 ^{o}C min^{-1} with a 20 min hold time. MS spectra were attained at a range m/z =40-650, scan speed=3333.

5.3 Results and discussion

5.3.1 XPS analysis

The XPS analysis for CuO/SiO$_2$ monolith was conducted to discover the oxidation states of the constituent elements. **Fig. 5.1(a)** displays the XPS survey spectra of the monolith. The peaks verify the occurrence of oxygen, silicon, and copper. The C 1s peak appeared because of the adventitious carbon from the instrument since C 1s signal is used as the reference at 284.5 eV. A single peak at 104 eV corresponds to Si 2p confirming the presence of tetravalent Si **(Fig. 5.1(b))**.[12] The de-convoluted asymmetric peaks for O 1s were obtained at 530. 1 and 533.3 eV which were credited to lattice oxygen and adsorbed water[13] **(Fig. 5.1(c))**. **Fig. 5.1(d)** shows the de-convoluted peaks for Cu 2p; two peaks observed at 933.8 and 953.8 eV corresponding to Cu $2p_{3/2}$ and Cu $2p_{1/2}$, respectively which could be attributed to Cu^{2+} in CuO.[14] Additionally, two satellite peaks at ~942.05 eV (A) and 962.8 eV (B) indicate the occurrence of oxidation state of +2 for cupric CuO.[3,14] The XPS analysis therefore affirmed the construction of pure CuO/SiO_2.

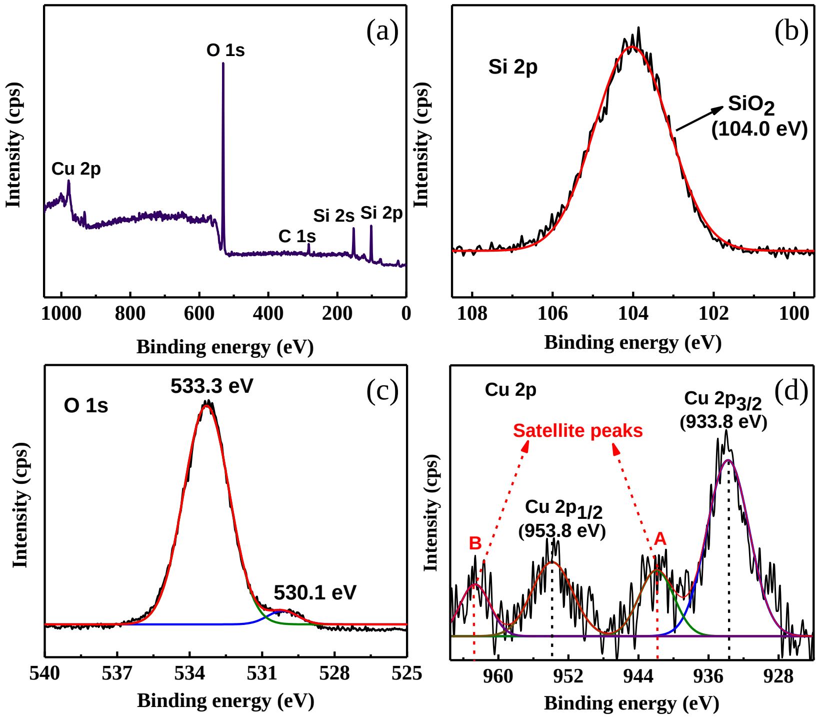

Fig. 5.1. XPS spectra of CuO/SiO_2 monolith; **(a)** survey spectrum, **(b)** Si 2p, **(c)** O 1s, and **(d)** Cu 2p.

5.3.2 XRD analysis

The XRD patterns of as-synthesized materials are demonstrated in **Fig. 5.2(a)**. The formation of pure SiO_2 monoliths was confirmed by broad peak at 22.3°.[15] In the case of CuO/SiO_2 monoliths, a broad peak located at around 22° occurred that can be attributed to SiO_2. The extra diffraction peaks can be indexed to pure CuO (JCPDS card No. 72-0629) ~32.50°

(110), 35.53° $(\bar{1}11)$, 38.73° (111), 48.78° $(\bar{2}02)$, 53.48° (020), 58.29° (202), 61.56° $(\bar{1}13)$, 66.25° $(\bar{3}11)$, 68.07° (220), 72.42° (311), and 75.05° (004). It validates that SiO_2 is properly loaded with CuO and CuO/SiO_2 monolith is successfully formed.

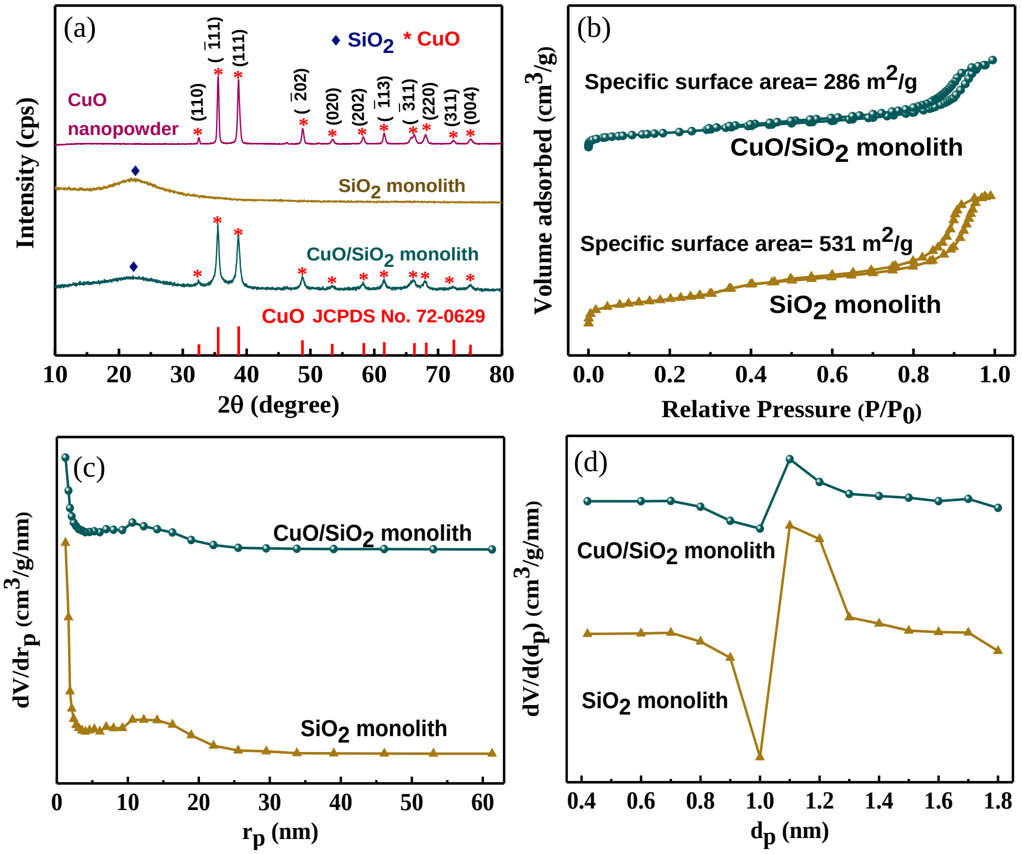

Fig. 5.2. (a) XRD analysis, **(b)** nitrogen adsorption-desorption isotherms, **(c)** BJH plot, and **(d)** MP plot for as-prepared materials.

5.3.3 N_2 adsorption-desorption studies

The N_2 adsorption-desorption experiments were performed for the evaluation of the surface parameters of the as-prepared monoliths. Both SiO_2 and CuO/SiO_2 monolith manifested Type-IV isotherms along with H1 hysteresis loop besides sharp sorption branches which affirmed that material was largely mesoporous **(Fig. 5.2b)**. The BJH plot **(Fig. 5.2c)** and MP plot **(Fig. 5.2d)** collectively revealed the hierarchical porosity as both types of monoliths had a large number of mesopores and additionally consisted of micropores. The specific surface area for SiO_2 and CuO/SiO_2 monolith was noted to be 531 and 286 m^2/g, respectively. The surface properties determined from these analyses are tabulated in **Table 5.1**.

Table 5.1. Surface properties of as-prepared monoliths.

Monolith	Specific surface area (m^2/g)	Total pore volume (cc/g)	Mesopore size (nm)	Micropore size (nm)
SiO_2	531	1.044	7.86	1.1
CuO/SiO_2	286	0.694	9.72	1.1

5.3.4 SEM-EDS analysis

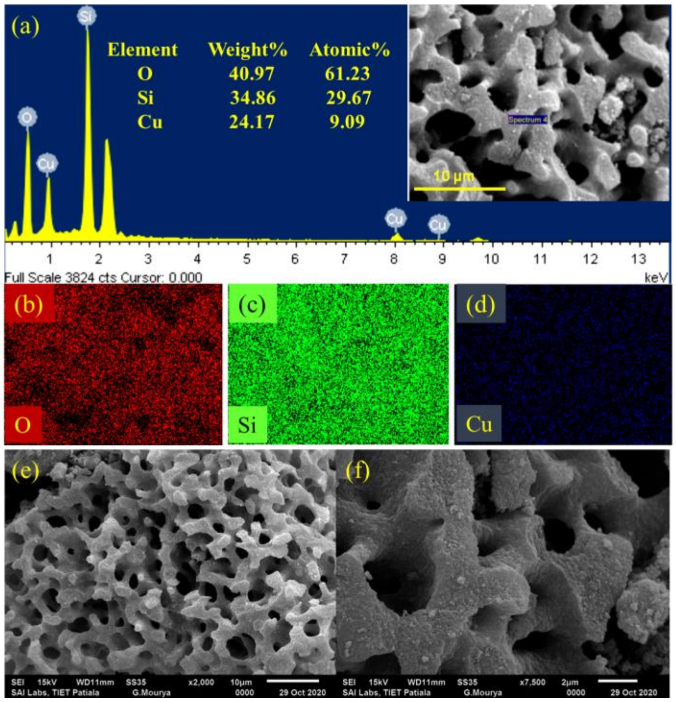

Element	Weight%	Atomic%
O	40.97	61.23
Si	34.86	29.67
Cu	24.17	9.09

Fig. 5.3 (a) EDS spectra, **(b-d)** color mapping, and **(e-f)** SEM images of CuO/SiO_2 monoliths.

The EDS analysis was conducted to examine the composition of the material which confirmed the presence of O, Si, and Cu as displayed in **Fig. 5.3(a)**. The uniform dispersal of the present elements in the CuO/SiO_2 monolith was affirmed through elemental mapping **(Fig. 3(b-d))**. The homogeneity could be ascribed to the uniform distribution of the precursor $Cu(NO_3)_2 \cdot 3H_2O$ salt solution. The SEM analysis was done to know the morphology of the CuO/SiO_2 monoliths. The highly porous connected network structure (fine mesopore/micropore structure in the macropore walls) is evident from the SEM images **(Fig. 5.3(e-f))**.

5.3.5 UV-visible DRS studies

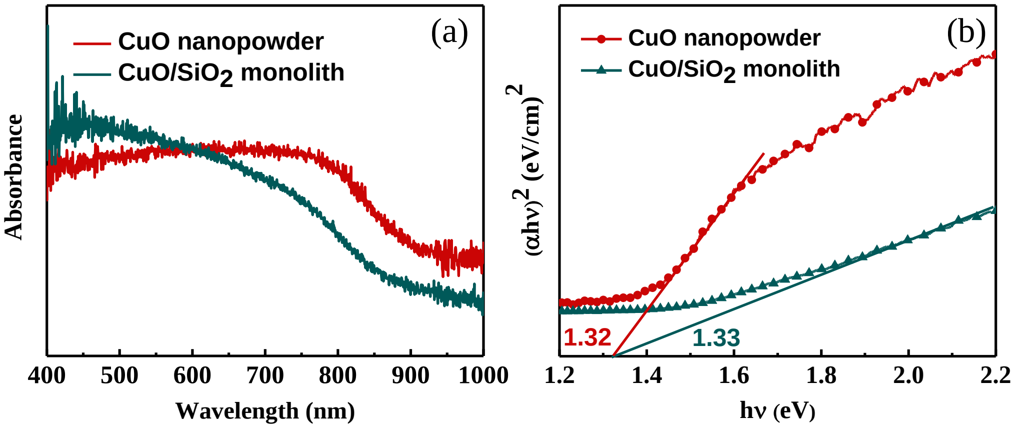

Fig. 5.4. (a) UV-visible DRS plot and **(b)** Tauc plot of CuO/SiO_2 monolith and CuO nanopowder.

Good light-harvesting ability and optimum band gap are essential features of a desirable photocatalyst.[16] The UV-visible DRS spectroscopy was used to estimate the absorption range of CuO/SiO_2 monolith and CuO powder. The absorption range of both CuO/SiO_2 monolith and CuO nanopowder is up to 800 nm and thus shows activity in visible-light **(Fig. 5.4(a))**. Tauc's equation **Eq. (5.1)** was followed for estimating the band gap energies.[17]

$$(\alpha h\nu)^2 = A(h\nu - E_g) \tag{5.1}$$

Here, α indicates the absorption coefficient, h represents the Planck constant, A is the proportionality constant, E_g is the band gap energy, and ν denotes light frequency. The band gap values of CuO nanopowder and CuO/SiO_2 monolith were close to each other **(Fig. 5.4(b))** and were evaluated to be 1.32 and 1.33 eV, respectively. The as-synthesized monolith is, therefore, visible-light responsive with a narrow band gap.[18]

5.3.6 PL analysis

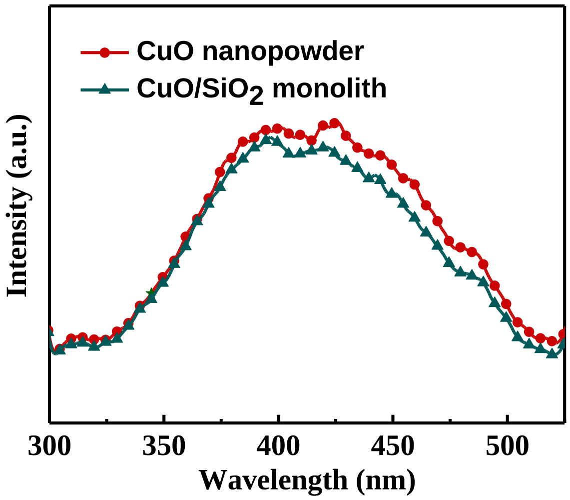

Fig. 5.5. PL spectra of CuO/SiO_2 monolith and CuO nanopowder.

A slow recombination rate, as well as efficacious charge separation and transfer of e^-/h^+ pairs, is crucial in photocatalysis. The e^-/h^+ recombination is directly associated with the intensity of PL emission signal. The PL spectra of the synthesized catalysts were monitored at an excitation wavelength of 280 nm.[19] CuO/SiO_2 monolith had a slightly lower PL intensity in comparison to CuO nanopowder implying a slower e^-/h^+ recombination rate in the former as shown in **Fig. 5.5**.[8]

5.3.7 Photocatalytic experiments

5.3.7.1 Kinetic analyses for Rh-B and TM degradation

For the assessment of the photocatalytic performance of CuO/SiO_2 monolith, model pollutants, xanthene dye Rh-B and colorless insecticide TM, were used. First of all, in the absence of any catalyst, about ~17.6% Rh-B **(Fig. 5.6(a))** and 15% TM **(Fig. 5.6(b))** were degraded in 180 min in visible light irradiation due to photolysis. The adsorption-desorption equilibrium was achieved in around 40 min in dark and %adsorption in case of Rh-B and TM was ~22% and 4%, respectively. After that visible lamp was turned ON and overall around 90.5% Rh-B was abated by using 0.25 g/L CuO/SiO_2 monolith **(Fig. 5.6(a))** while 55% photodegradation of TM was achieved by using 0.1 g/L monolith **(Fig. 5.6(b))** within 180 min of visible-light treatment. On the contrary, the treatment of the Rh-B and TM for 180 min under dark conditions (lamp OFF) demonstrated only about 23.5% and 4% removal, respectively as shown in **Fig. 5.6(c)**.

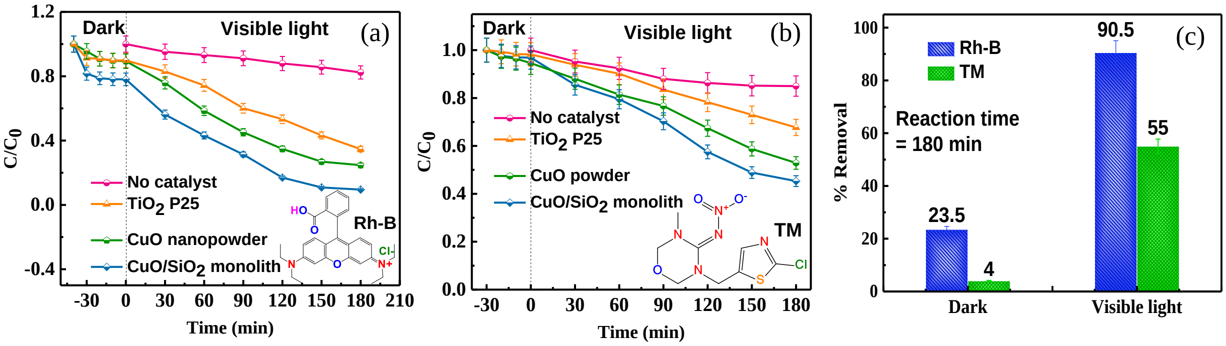

Fig. 5.6. Kinetic analyses for **(a)** Rh-B degradation, **(b)** TM degradation using various materials, and **(c)** comparison of removal in dark and visible light using CuO/SiO_2 monolith.

The as-synthesized monolith also manifested superior photoactivity as compared to commercial catalysts TiO_2 P25 and CuO nanopowders **(Table 5.2)**. The rate constant was evaluated after the kinetic studies through **Eq. (2.3)** mentioned in **Chapter 2.** The photodegradation reaction followed pseudo-first order kinetics **(Fig. 5.7(a-b))** and the rate constants for Rh-B and TM degradation were 0.01255 and 0.00443 min^{-1}, respectively, using

CuO/SiO_2 monolith. These values were greater as compared to commercial TiO_2 P25 and CuO nanopowder as tabularized in **Table 5.2**.

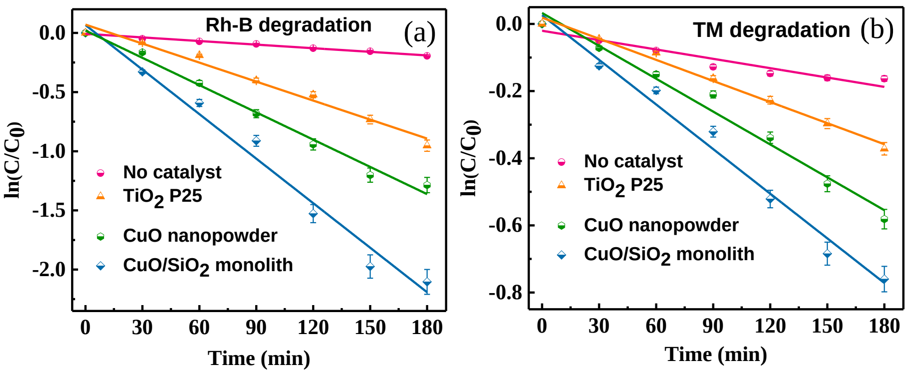

Fig. 5.7. First-order kinetics for degradation of **(a)** Rh-B and **(b)** TM.

Table 5.2. Degradation parameters of Rh-B and TM using different catalysts.

Catalyst	Rh-B			TM		
	% Degradation	Rate constant (min^{-1})	R^2	% Degradation	Rate constant (min^{-1})	R^2
No catalyst	17.6	0.00102	0.9882	15	0.00093	0.9058
CuO nanopowder	75.3	0.00768	0.9877	47.12	0.00326	0.9764
TiO_2 P25 nanopowder	65.35	0.00535	0.9758	32.3	0.00210	0.9885
CuO/SiO_2 monolith	90.5	0.01255	0.9771	55	0.00443	0.9811

A synergy factor (R) was also calculated through **Eq. (5.2)** for the quantification of the degree of synergy effect of CuO/SiO_2 in contrast to pure CuO.[20]

$$R = k_{CuO/SiO2} / k_{CuO} \qquad (5.2)$$

R was evaluated to be ~1.63 for Rh-B degradation and ~1.36 for TM degradation demonstrating the synergistic effect amid CuO and SiO_2 in the process.

The effect of CuO loading on the degradation efficiency was also observed by preparing CuO/SiO_2 monoliths by impregnating varying concentrations of $Cu(NO_3)_2•3H_2O$ (0.1, 0.5 and 1 M) into SiO_2 monoliths. It was noted that photoactivity was increased when precursor concentration increased from 0.1 to 0.5 M and remained almost constant thereafter at 1 M as displayed in **Fig. 5.8**.

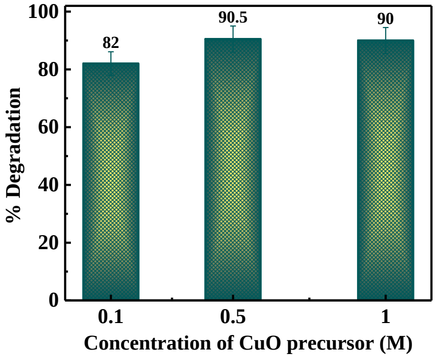

Fig. 5.8. Kinetic analysis for the photodegradation of RhB using 0.25 g/L CuO/SiO_2 prepared by using different concentrations of $Cu(NO_3)_2•3H_2O$ for impregnation into fixed amount of SiO_2 monoliths.

5.3.7.2 Effect of catalyst concentration

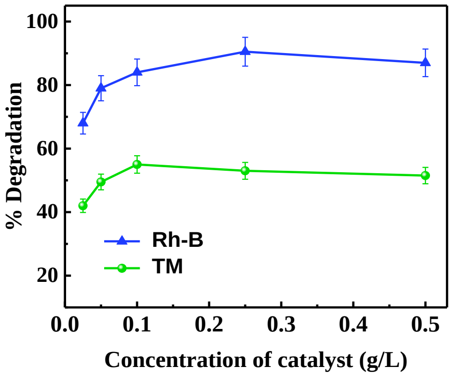

Fig. 5.9. Effect of catalyst concentration on the photocatalytic degradation of Rh-B and TM.

To analyze the influence of the monolith concentration on the photodegradation process, the same experiment was conducted using different catalyst concentrations (0.025, 0.05, 0.1, 0.25, and 0.5 g/L) as illustrated in **Fig. 5.9**. The maximum percent degradation was noted at 0.25 g/L for Rh-B while at 0.1 g/L for TM. Attributing to the opaqueness of solution along with the blockage of active sites, a decline in the removal efficacy was observed thereafter in both the cases.

5.3.7.3 Effect of pH

The impact of pollutant solution-pH on the photodegradation efficacy was examined across a pH range (1, 3, 5, 7 (natural pH of solutions), 9, and 11). The differing surface charge of CuO/SiO$_2$ at distinct pH values as well as the electrical charges of pollutant is responsible for the dissimilar photoactivity as the solution pH varies. The point of zero charge (pzc) on the surface of prepared monolith was around pH 7.6 **(Fig. 5.10(a))**. The material has thus a positive surface below pH 7.6 (facilitating adsorption of anionic pollutants) while the surface charge is negative above this value (preferring adsorption of cationic pollutants).

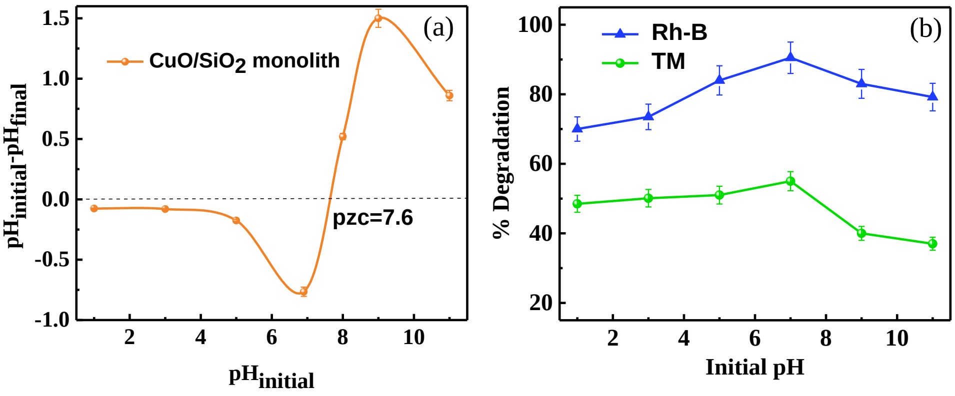

Fig. 5.10. Plot showing **(a)** pzc studies and **(b)** effect of pH on the photodegradation of Rh-B and TM using CuO/SiO$_2$ monolith.

The maximum degradation efficacies were noted at natural pH of the solutions i.e., ~90.5 % for Rh-B and 55% for TM **(Fig. 5.10(b))**. Aqueous Rh-B solution has pka~3.7 and it occurs as Rh-B$^+$ (cationic form) below pH 3.7 and exists as Rh-B$^\pm$ (zwitterionic form) above pH 3.7

ascribing to the carboxyl group deprotonation. From pH 1 to 3, there is repulsion amongst the positive surface of both Rh-B and catalyst causing poor efficiency. Beyond pH 3, the efficiency rises owing to the electrostatic attraction between catalyst and Rh-$B^{\pm}$. At pH>pzc, a drop was noticed because the negatively charged surface of monolith and Rh-$B^{\pm}$ repel each other.[21] Regarding TM, photocatalytic degradation was aided in the acidic and neutral range because the surface of TM is anionic and above pzc there was a decline because of repulsive forces among TM and catalyst.[22] The optimal monolithic concentration and pH 7 were the set conditions for further experiments. To compare the activity of as-prepared monolith with those prepared in previous chapters, the activity for degradation of MB dye at optimal conditions was also noted which was ~86.2%.

5.3.7.4 Effect of illumination area

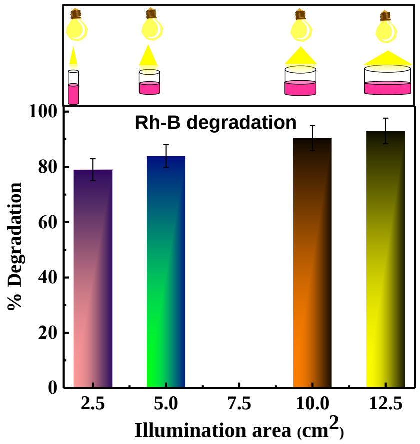

Fig. 5.11. Effect of illumination area on the photodegradation of Rh-B by CuO/SiO_2 monolith.

For the inspection of the role of total effective illumination area on the detoxification efficacy of Rh-B, the same experiment was conducted in reaction flasks with distinct diameters and keeping the CuO/SiO_2 monolith concentration (0.25 g/L) and the gap among visible lamp and topmost layer of solution (10 cm) fixed. The area of the solution that came under exposure to direct visible light was therefore variable (~2.5, 5, 10, and 12.5 cm^2). The removal efficacy was noted to accelerate as there was a surge in the illumination area of the reactor (exposed area of the solution) **(Fig. 5.11)**.

5.3.7.5 TOC analyses

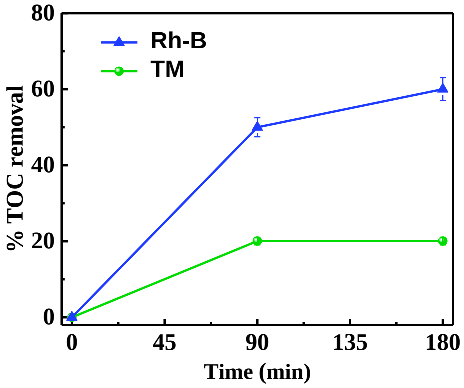

Fig. 5.12. TOC analyses after photocatalytic treatment with CuO/SiO$_2$ monolith.

TOC measurements were also conducted to evaluate the mineralization degree of organic pollutants. The experiments were carried out at optimal experimental conditions. The plot displaying %TOC removal of Rh-B and TM with respect to time after treating with CuO/SiO$_2$ monolith is shown in **Fig. 5.12**. Around 60.03% TOC removal was noted in case of Rh-B while ~20.05% was observed in case of TM after 180 min of treatment. Low mineralization in case of TM is possibly because of its recalcitrant nature. The difference between %degradation and %TOC removal can be ascribed to the formation of intermediates during the process. Similar observations were also reported in literature.[23,24]

5.3.8 Plausible mechanism

To determine the primary active species in the reaction mechanism, scavenger tests were conducted. Different scavengers with concentrations ~1 mM were utilized for this purpose; methanol as a hole scavenger, DMSO as a quencher for hydroxyl radicals ($^{\bullet}$OH), and benzoquinone (BQ) for trapping superoxide radicals ($O_2^{\bullet-}$). The reaction in both the cases (Rh-B and TM degradation) got retarded to the maximum extent when methanol was used as displayed in **Fig. 5.13(a)**. This implied that holes were majorly involved in the degradation process using CuO/SiO_2 monolith.

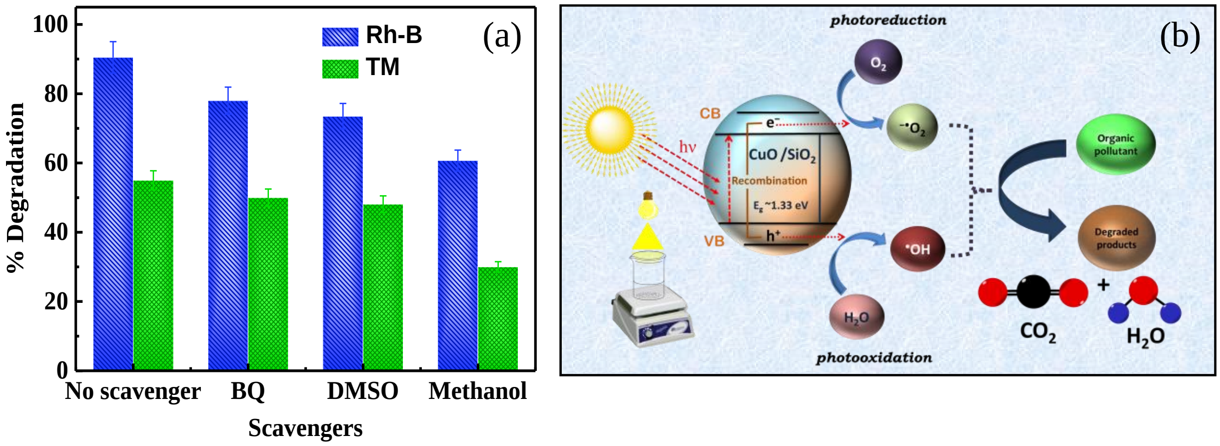

Fig. 5.13. (a) Effect of various scavengers and **(b)** photodegradation mechanism of Rh-B and TM via CuO/SiO_2 monolithic photocatalyst.

When visible radiation is illumined, CuO/SiO_2 monolith undergoes absorption of photons (hν ≥ E_g) and consequently there is excitation of e^- from VB to conduction band (CB) and h^+ is left behind in VB. The reaction of h^+ with ^-OH gives rise to $^{•}OH$ whereas the reaction of O_2 with e^- in CB forms $O_2^{•-}$. These active species undergo reaction with Rh-B and TM and take the degradation process further by attacking the bonds **(Fig. 5.13(b)).** The possible reaction steps are presented in **Eq. (5.3)** - **Eq. (5.7)**.

$$\mathrm{CuO/SiO_2} + h\nu \rightarrow e^- + h^+ \tag{5.3}$$

$$H_2O + h^+ \rightarrow H_2O^+ \tag{5.4}$$

$$H_2O^+ \rightarrow {}^{•}OH + H^+ \tag{5.5}$$

$$O_2 + e^- \rightarrow O_2^{•-} \tag{5.6}$$

$$h^+/{}^{•}OH/\ O_2^{•-} + \text{Rh-B/TM} \rightarrow \text{intermediates} \rightarrow \text{degraded products} \tag{5.7}$$

5.3.9 GC-MS analysis

5.3.9.1 GC-MS analysis of Rh-B-degradation

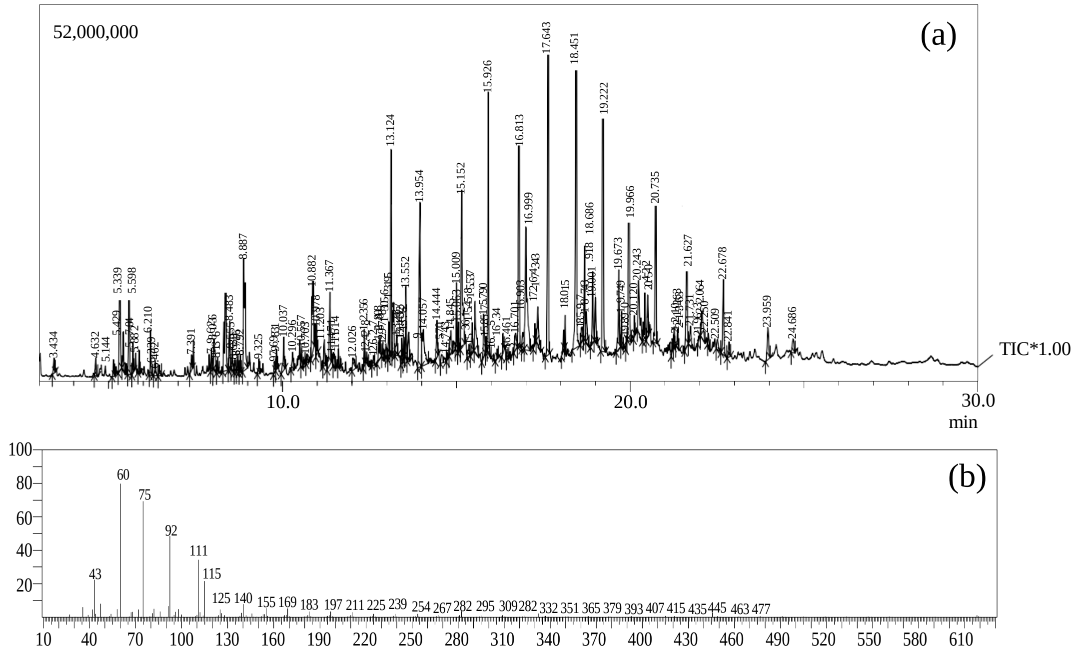

Fig. 5.14. (a) GC spectra of Rh-B after photocatalytic degradation and **(b)** MS spectra of Rh-B after photodegradation at retention time of 17.643 min.

For the identification of intermediates and products in the photodegradation reaction of Rh-B, GC-MS analysis was carried out. The GC chromatogram and mass spectrum of Rh-B after treatment are shown in **Fig. 5.14 (a)** and **(b)**, respectively. The proposed degradation pathway has been displayed in **Scheme 5.2.** The N-de-ethylation of Rh-B may generate compound (I) and (II) (m/z=415.2) [M+]+. The further N-de-ethylation of compound (I) and (II) may lead to the formation of (III, IV) and (V, VI), respectively. These N-de-ethylated intermediates may get degraded into intermediate (XI) (m/z=331.11) [M+H]+ which may further be degraded to intermediates XVI (m/z=115.04) [M+]+. The N-de-ethylation and subsequent carboxylation of (I) could also form intermediates VI (m/z=282.10) [M+]+ and X (m/z=254.07) [M+]+. The formed intermediates were finally oxidized via chromophoric cleavage into nontoxic organic compounds like pyrocatechol (m/z=110.04) [M+H]+, propane-1,2,3-triol (m/z=92.05) [M+]+, and organic acids like propionic acid (m/z=74.04) [M+H]+, and acetic acid (m/z=60.02) [M+]+. These products finally get mineralized into CO_2, H_2O, NO_3^- and NH_4^+.[25,26]

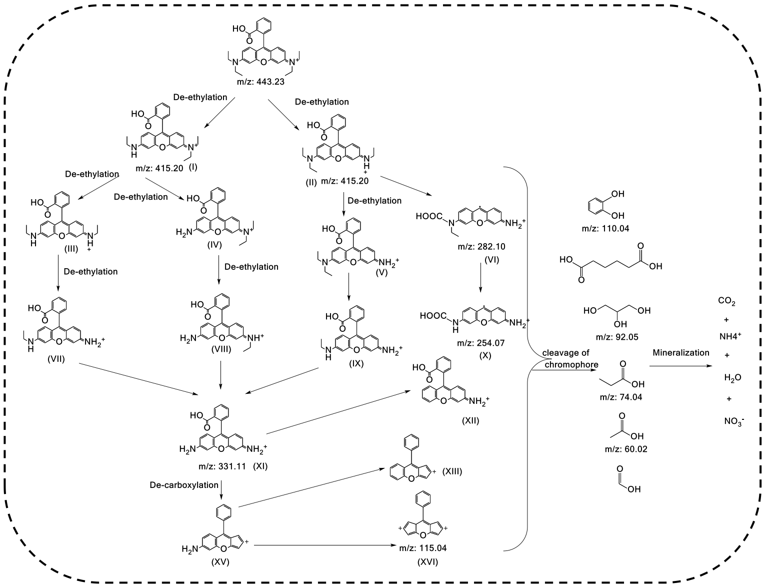

Scheme 5.2. Possible degradation pathway of Rh-B by CuO/SiO_2 monoliths.

5.3.9.2 GC-MS analysis of TM-degradation

The GC chromatogram and mass spectrum of TM after treatment are shown in **Fig. 5.15 (a)** and **(b)**, respectively. The proposed degradation pathway has been displayed in **Scheme 5.3.** In the first pathway, the de-nitration of TM molecule could lead to the formation of 3-((2-chlorothiazol-5-yl) methyl)-5-methyl-1,3,5-oxadiazinan-4-imine which could lose chlorine group to form 3-methyl-5-(thiazol-5-ylmethyl)-1,3,5-oxadiazinan-4-imine and the H-atom abstraction product, (E)-4-imino-5-methyl-3-(thiazol-5-ylmethylene)-1,3,5-oxadiazinan-3-ium (m/z=211.06) [M+]+, generated via the attack of hydroxyl group. Subsequently, the fragmentation of methine connecting the 1,3,5-oxadiazinane ring and thiazole ring together via attack of hydroxyl radical could produce 3-methyl-1,3,5-oxadiazinan-4-imine (m/z=115.07) [M+]+ and 5-methylthiazole (m/z=99.01) [M+]+. This compound could either undergo demethylation to produce thiazole (m/z=85) [M+]+ or could undergo ring cleavage to generate (Z)-but-2-enal (m/z=70.04)

[M+H]+. In the second pathway, the attack of hydroxyl attack on thiamethoxam could replace –Cl with –OH which would immediately undergo keto-enol tautomerism to form (E)-N-(3-methyl-5-((2-oxo-2,3-dihydrothiazol-5-yl)methyl)-1,3,5-oxadiazinan-4-ylidene)nitramide. Then the further hydroxylation might procure (I), and H-atom abstraction products (II), and (III). The subsequent ring decomposition ascribing to hydroxyl attack could generate acrylaldehyde (m/z=56.03) [M+H]+. The findings were in accordance with the literature reports.[27,28]

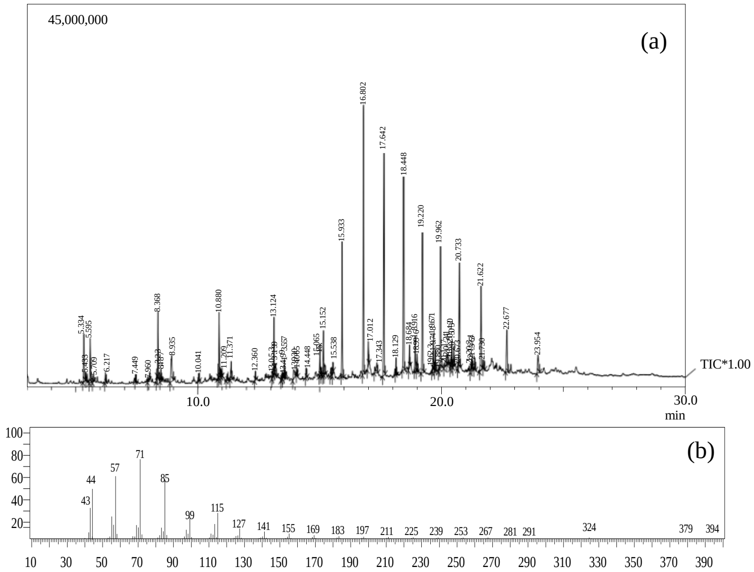

Fig. 5.15. (a) GC spectra of TM after photocatalytic degradation and **(b)** MS spectra of TM after photodegradation at retention time of 16.802 min.

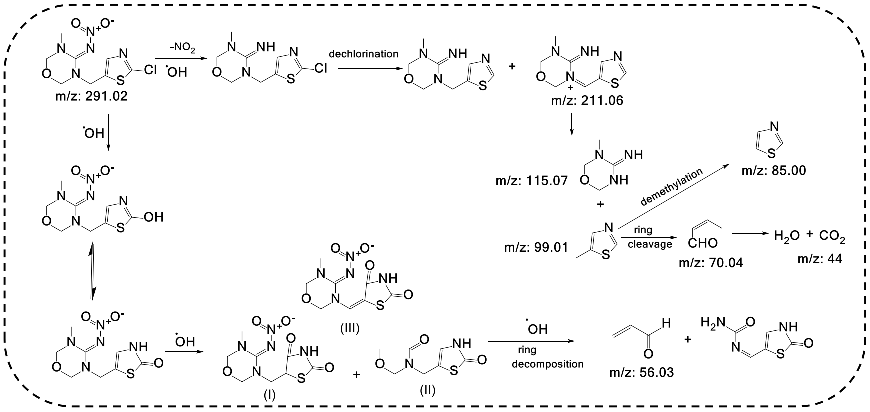

Scheme 5.3. Possible degradation pathway of TM by CuO/SiO$_2$ monoliths.

5.3.10 Comparison with literature

A comparison of the as-prepared CuO/SiO_2 monolith was carried out with recently reported CuO based photocatalysts and other catalysts for the photocatalytic removal of Rh-B and TM as tabularized in **Table 5.3**. Degradation of both the contaminants was not earlier studied by CuO/SiO_2 monolithic catalyst in visible light as evident from literature. It can be deduced that a low dose of as-prepared monolith can effectively abate recalcitrant contaminants under visible light illumination at natural pH and ambient conditions. Moreover, the photocatalytic degradation of colorless pollutant affirms the occurrence of indirect mechanism.

Table 5.3. Comparison of various photocatalysts for photodegradation of Rh-B and TM.

Catalyst	Pollutant conc.	Catalyst conc. (g/L)	Time (min)	Light source	Light intensity	% degradation	Rate constant *k* (min^{-1})	Ref.
CuO nanoparticles	Rh-B (100 µM)	1	150	Visible light (fluorescent lamp)	-	83	-	[29]
ZnO/CuO composite on Cu foam	Rh-B (5 ppm)	-	120	Visible light (300 W Xe lamp)	-	63.8	0.0078	[30]
Ta_3N_5/ Bi_2MoO_6	Rh-B (5 ppm)	0.3	60	Visible light (Xe lamp)	-	99.5	0.0776	[31]
Ag_2O/ Ta_3N_5	Rh-B (10 ppm)	-	60	Visible light (300 W Xe lamp)	-	99.5	0.0702	[32]
Bi_2WO_6/ calcined mussel shell	Rh-B (20 ppm)	-	150	Visible light	-	98.4	0.0248	[33]

SnO_2 quantum dots	TM (50 ppm)	0.1	45	Solar light	-	57	-	[34]
Sulfate doped-Ag_3PO_4	TM (5 ppm)	0.8	60	Visible light (six 4 W fluorescent lamps)	1.03 mW cm^{-2}	39.94	0.008	[35]
CuO powder	TM (5 ppm)	1	60	Visible light (72 W LED lamp)	-	48.65	0.0109	[36]
CuO/SiO_2 monolith	Rh-B (5 ppm)	0.25	180	Visible light (45 W CFL lamp)	10 mW cm^{-2}	90.5	0.01255	This study
CuO/SiO_2 monolith	TM (25 ppm)	0.1	180	Visible light (45 W CFL lamp)	10 mW cm^{-2}	55	0.00443	This study

5.3.11 Reusability experiments

The main highlight of the CuO/SiO_2 monolithic catalyst that, it is easily recoverable ascribing to single rock-like form. The washing of the photocatalyst was done by employing double distilled water properly after the photocatalytic reaction and later it was dried at 40 ºC. The assessment of the reusable nature of the as-prepared monolith was assessed for five successive cycles for Rh-B degradation. The photocatalytic efficacy reduced by ~12% after five runs as displayed in **Fig. 5.16a**. The reusability efficiency was justified by characterization results after photocatalytic experiment. The XRD and surface area analyses of CuO/SiO_2 monolith were also performed after the photocatalytic degradation (five cycles). The XRD diffraction peaks in the reused catalyst were almost unchanged after the reaction **(Fig. 5.16b)**. The N_2 sorption isotherms of the monolith before and after photodegradation is exhibited in **Fig. 5.16(c)** while BJH plot and MP plot are displayed in **Fig. 5.16(d-e)**. The isotherms and BJH-MP plot affirmed that the hierarchical nature of the material was intact after the reaction and the material's surface area reduced from 286 to 259 m^2/g. The surface parameters of the monolith before and after the photocatalytic experiments are tabulated in **Table 5.4**. Moreover, the monolith retained networked porous structure after the photocatalytic reaction which as confirmed by SEM analysis **Fig. 5.16(f)**. The results justified the reusability efficiency and demonstrated that the CuO/SiO$_2$ monolith is a potent material for large-scale applications.

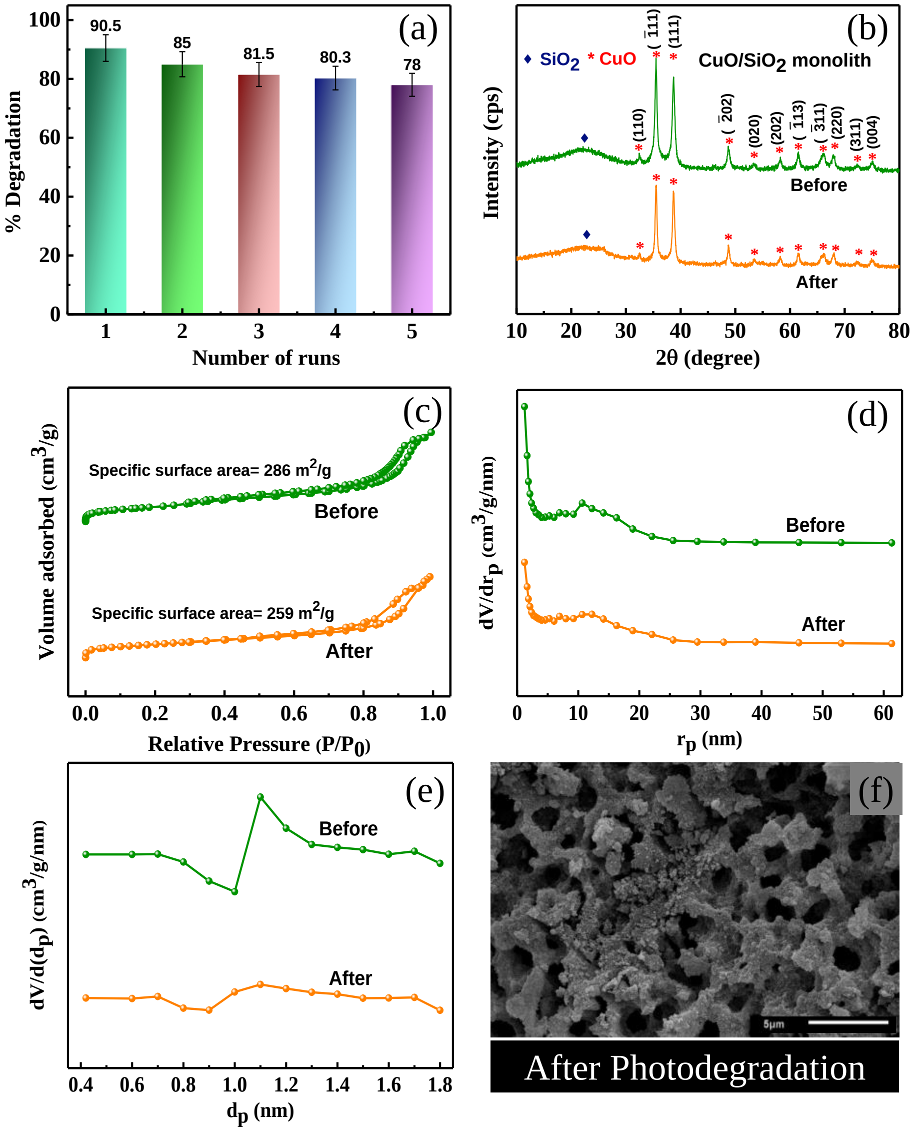

Fig. 5.16. (a) Reusability tests of CuO/SiO$_2$ monolith for Rh-B degradation, **(b)** XRD plot, **(c)** N$_2$ sorption isotherms, **(d)** BJH plot, **(e)** MP plot of the CuO/SiO$_2$ monolith prior to and post the photocatalytic experiment, and **(f)** SEM image of the CuO/SiO$_2$ monolith after photocatalytic experiment.

Table 5.4. Surface properties of as-prepared materials before and after degradation.

CuO/SiO_2 monolith	Specific surface area (m^2/g)	Total pore volume (cc/g)	Mesopore size (nm)	Micropore size (nm)
Before degradation	286	0.694	9.72	1.1
After degradation	259	0.627	9.68	1.1

5.4 Conclusions

In this chapter, hierarchical porous visible-light-active CuO/SiO_2 monoliths in centimeter-scale were prepared by wet impregnation technique. The material was later assessed for the photocatalytic abatement of model contaminants Rh-B and TM. The interconnected porous network structure, enormous surface area, and suitable optical properties rendered the monoliths promising for photocatalysis. Impact on the degradation due to diverse factors like pH of the contaminant, catalyst concentration, and illumination area was also scrutinized. Holes were discovered to have a predominant role in the degradation process as validated through scavenger experiments. The degraded products have also been analyzed through GC-MS studies. The mineralization degree of the contaminants was gauged through TOC measurements. The easily recoverable nature of monolithic photocatalyst was restated by the reusability experiments. The XRD and surface area analyses after the photocatalysis demonstrated that the crystallinity and surface properties and morphological features of the material were almost intact post the photocatalytic process. The study established that easy-to-recover CuO/SiO_2 monoliths possess high competence for wastewater treatment.

References

(1) Liu, S.; Ru, J.; Liu, F. NiP/CuO Composites: Electroless Plating Synthesis, Antibiotic Photodegradation and Antibacterial Properties. *Chemosphere* **2021**, *267*, 129220. https://doi.org/10.1016/j.chemosphere.2020.129220.

(2) Nogueira, A. C.; Gomes, L. E.; Ferencz, J. A. P.; Rodrigues, J. E. F. S.; Goncąlves, R. V.; Wender, H. Improved Visible Light Photoactivity of $CuBi_2O_4$/CuO Heterojunctions for Photodegradation of Methylene Blue and Metronidazole. *J. Phys. Chem. C* **2019**, *123* (42), 25680–25690. https://doi.org/10.1021/acs.jpcc.9b06907.

(3) Xu, L.; Zhang, J.; Li, Z.; Ma, Q.; Wang, Y.; Cui, F.; Cui, T. In Situ Generation of Ultrasmall Sized and Highly Dispersed CuO Nanoparticles Embedded in Silica Matrix and Their Catalytic Application. *New J. Chem.* **2019**, *43* (1), 520–526. https://doi.org/10.1039/C8NJ04517H.

(4) Li, X.; Zhang, W.; Liu, N.; Qu, R.; Wei, Y.; Feng, L. Superwetting Copper Meshes Based on Self-Organized Robust CuO Nanorods: Efficient Water Purification for in Situ Oil Removal and Visible Light Photodegradation. *Nanoscale* **2018**, *10* (9), 4561–4569. https://doi.org/10.1039/C7NR09201F.

(5) Lim, Y.-F.; Chua, C. S.; Lee, C. J. J.; Chi, D. Sol–Gel Deposited Cu_2O and CuO Thin Films for Photocatalytic Water Splitting. *Phys. Chem. Chem. Phys.* **2014**, *16* (47), 25928–25934. https://doi.org/10.1039/C4CP03241A.

(6) Anu Prathap, M. U.; Kaur, B.; Srivastava, R. Hydrothermal Synthesis of CuO Micro-/Nanostructures and Their Applications in the Oxidative Degradation of Methylene Blue and Non-Enzymatic Sensing of Glucose/H_2O_2. *J. Colloid Interface Sci.* **2012**, *370* (1), 144–154. https://doi.org/10.1016/j.jcis.2011.12.074.

(7) Geng, L.; Li, G.; Zhang, X.; Wang, X.; Li, C.; Liu, Z.; Zhang, D. S.; Zhang, Y. Z.; Wang, G.; Han, H. Rational Design of CuO/SiO_2 Nanocatalyst with Anchor Structure and Hydrophilic Surface for Efficient Hydrogenation of Nitrophenol. *J. Solid State Chem.* **2021**, *296* (January), 121960. https://doi.org/10.1016/j.jssc.2021.121960.

(8) Hao, Q.; Niu, X.; Nie, C.; Hao, S.; Zou, W.; Ge, J.; Chen, D.; Yao, W. A Highly Efficient G-C_3N_4/SiO_2 Heterojunction: The Role of SiO_2 in the Enhancement of Visible Light Photocatalytic Activity . *Phys. Chem. Chem. Phys.* **2016**, *18* (46), 31410–31418. https://doi.org/10.1039/c6cp06122b.

(9) Ramya, E.; Thirumurugan, A.; Rapheal, V. S.; Anand, K. CuO@SiO_2 Nanoparticles Assisted Photocatalytic Degradation of 4-Nitrophenol and Their Antimicrobial Activity Studies. *Environ. Nanotechnology, Monit. Manag.* **2019**, *12*, 100240. https://doi.org/10.1016/j.enmm.2019.100240.

(10) Rajabzadeh, M.; Khalifeh, R.; Eshghi, H.; Hafizi, A. Design and Synthesis of CuO@SiO_2 Multi-Yolk@shell and Its Application as a New Catalyst for CO_2 Fixation Reaction under Solventless Condition. *J. Ind. Eng. Chem.* **2020**, *89*, 458–469. https://doi.org/10.1016/j.jiec.2020.06.020.

(11) Batista, A. P. L.; Carvalho, H. W. P.; Luz, G. H. P.; Martins, P. F. Q.; Gonçalves, M.; Oliveira, L. C. A. Preparation of CuO/SiO_2 and Photocatalytic Activity by Degradation of Methylene Blue. *Environ. Chem. Lett.* **2010**, *8* (1), 63–67. https://doi.org/10.1007/s10311-008-0192-8.

(12) Sri Devi Kumari, T.; Jeyakumar, D.; Prem Kumar, T. Nano Silicon Carbide: A New Lithium-Insertion Anode Material on the Horizon. *RSC Adv.* **2013**, *3* (35), 15028–15034. https://doi.org/10.1039/c3ra40798e.

(13) Zhao, W.; Yang, C.; Huang, J.; Jin, X.; Deng, Y.; Wang, L.; Su, F.; Xie, H.; Wong, P. K.; Ye, L. Selective Aerobic Oxidation of Sulfides to Sulfoxides in Water under Blue Light Irradiation over $Bi_4O_5Br_2$. *Green Chem.* **2020**, *22* (15), 4884–4889. https://doi.org/10.1039/D0GC01930E.

(14) Soleimani, E.; Moghaddami, R. Synthesis, Characterization and Thermal Properties of PMMA/CuO Polymeric Nanocomposites. *J. Mater. Sci. Mater. Electron.* **2018**, *29* (6), 4842–4854. https://doi.org/10.1007/s10854-017-8440-y.

(15) Wang, W.; Fang, J.; Chen, H. Nano-Confined g-C_3N_4 in Mesoporous SiO_2 with Improved Quantum Size Effect and Tunable Structure for Photocatalytic Tetracycline Antibiotic Degradation. *J. Alloys Compd.* **2020**, *819*, 153064. https://doi.org/10.1016/j.jallcom.2019.153064.

(16) Li, X.; Yu, J.; Jaroniec, M. Hierarchical Photocatalysts. *Chem. Soc. Rev.* **2016**, *45*, 2603–

2636. https://doi.org/10.1039/c5cs00838g.

(17) Sharma, A.; Dutta, R. K. Studies on the Drastic Improvement of Photocatalytic Degradation of Acid Orange-74 Dye by TPPO Capped CuO Nanoparticles in Tandem with Suitable Electron Capturing Agents. *RSC Adv.* **2015**, *5* (54), 43815–43823. https://doi.org/10.1039/C5RA04179A.

(18) Balık, M.; Bulut, V.; Erdogan, I. Y. Optical, Structural and Phase Transition Properties of Cu_2O, CuO and Cu_2O/CuO: Their Photoelectrochemical Sensor Applications. *Int. J. Hydrogen Energy* **2019**, *44* (34), 18744–18755. https://doi.org/10.1016/j.ijhydene.2018.08.159.

(19) Praveen, K. H.; Prasad, A. S. Hesperidin Mediated Synthesis, Structure and Optical Emission Analysis on Nanocrystalline CuO. *Mater. Today Proc.* **2021**, *41*, 520–524. https://doi.org/10.1016/j.matpr.2020.05.237.

(20) Wang, R.; Shi, K.; Huang, D.; Zhang, J.; An, S. Synthesis and Degradation Kinetics of TiO_2/GO Composites with Highly Efficient Activity for Adsorption and Photocatalytic Degradation of MB. *Sci. Rep.* **2019**, *9* (1), 18744. https://doi.org/10.1038/s41598-019-54320-w.

(21) Xiao, W.; Garba, Z. N.; Sun, S.; Lawan, I.; Wang, L.; Lin, M.; Yuan, Z. Preparation and Evaluation of an Effective Activated Carbon from White Sugar for the Adsorption of Rhodamine B Dye. *J. Clean. Prod.* **2020**, *253*, 119989. https://doi.org/10.1016/j.jclepro.2020.119989.

(22) Mir, N. A.; Khan, A.; Muneer, M.; Vijayalakhsmi, S. Photocatalytic Degradation of a Widely Used Insecticide Thiamethoxam in Aqueous Suspension of TiO_2: Adsorption, Kinetics, Product Analysis and Toxicity Assessment. *Sci. Total Environ.* **2013**, *458–460*, 388–398. https://doi.org/10.1016/j.scitotenv.2013.04.041.

(23) Isari, A. A.; Payan, A.; Fattahi, M.; Jorfi, S.; Kakavandi, B. Photocatalytic Degradation of Rhodamine B and Real Textile Wastewater Using Fe-Doped TiO 2 Anchored on Reduced Graphene Oxide (Fe-TiO_2/RGO): Characterization and Feasibility, Mechanism and

Pathway Studies. *Appl. Surf. Sci.* **2018**, *462* (July), 549–564. https://doi.org/10.1016/j.apsusc.2018.08.133.

(24) Žabar, R.; Komel, T.; Fabjan, J.; Kralj, M. B.; Trebše, P. Photocatalytic Degradation with Immobilised TiO_2 of Three Selected Neonicotinoid Insecticides: Imidacloprid, Thiamethoxam and Clothianidin. *Chemosphere* **2012**, *89* (3), 293–301. https://doi.org/10.1016/j.chemosphere.2012.04.039.

(25) Gemeay, A. H.; El-Halwagy, M. E.; Elsherbiny, A. S.; Zaki, A. B. Amine-Rich Quartz Nanoparticles for Cu(II) Chelation and Their Application as an Efficient Catalyst for Oxidative Degradation of Rhodamine B Dye. *Environ. Sci. Pollut. Res.* **2021**, *28* (22), 28289–28306. https://doi.org/10.1007/s11356-021-12497-6.

(26) Natarajan, T. S.; Thomas, M.; Natarajan, K.; Bajaj, H. C.; Tayade, R. J. Study on UV-LED/TiO_2 Process for Degradation of Rhodamine B Dye. *Chem. Eng. J.* **2011**, *169* (1–3), 126–134. https://doi.org/10.1016/j.cej.2011.02.066.

(27) Yao, Y.; Huang, C.; Yang, Y.; Li, M.; Ren, B. Electrochemical Removal of Thiamethoxam Using Three-Dimensional Porous PbO_2-CeO_2 Composite Electrode: Electrode Characterization, Operational Parameters Optimization and Degradation Pathways. *Chem. Eng. J.* **2018**, *350* (May), 960–970. https://doi.org/10.1016/j.cej.2018.06.036.

(28) Rani, M.; Shanker, U. Removal of Chlorpyrifos, Thiamethoxam, and Tebuconazole from Water Using Green Synthesized Metal Hexacyanoferrate Nanoparticles. *Environ. Sci. Pollut. Res.* **2018**, *25* (11), 10878–10893. https://doi.org/10.1007/s11356-018-1346-2.

(29) Shayegan Mehr, E.; Sorbiun, M.; Ramazani, A.; Taghavi Fardood, S. Plant-Mediated Synthesis of Zinc Oxide and Copper Oxide Nanoparticles by Using Ferulago Angulata (Schlecht) Boiss Extract and Comparison of Their Photocatalytic Degradation of Rhodamine B (RhB) under Visible Light Irradiation. *J. Mater. Sci. Mater. Electron.* **2018**, *29* (2), 1333–1340. https://doi.org/10.1007/s10854-017-8039-3.

(30) Cao, F.; Wang, T.; Ji, X. Enhanced Visible Photocatalytic Activity of Tree-like ZnO/CuO

Nanostructure on Cu Foam. *Appl. Surf. Sci.* **2019**, *471*, 417–424. https://doi.org/10.1016/j.apsusc.2018.12.034.

(31) Li, S.; Shen, X.; Liu, J.; Zhang, L. Synthesis of Ta_3N_5/Bi_2MoO_6 Core–Shell Fiber-Shaped Heterojunctions as Efficient and Easily Recyclable Photocatalysts. *Environ. Sci. Nano* **2017**, *4* (5), 1155–1167. https://doi.org/10.1039/C6EN00706F.

(32) Li, S.; Hu, S.; Xu, K.; Jiang, W.; Liu, Y.; Leng, Z.; Liu, J. Construction of Fiber-Shaped Silver Oxide/Tantalum Nitride p-n Heterojunctions as Highly Efficient Visible-Light-Driven Photocatalysts. *J. Colloid Interface Sci.* **2017**, *504*, 561–569. https://doi.org/10.1016/j.jcis.2017.06.018.

(33) Li, S.; Wang, C.; Liu, Y.; Xue, B.; Chen, J.; Wang, H.; Liu, Y. Facile Preparation of a Novel Bi_2WO_6/Calcined Mussel Shell Composite Photocatalyst with Enhanced Photocatalytic Performance. *Catalysts* **2020**, *10* (10), 1166. https://doi.org/10.3390/catal10101166.

(34) Das, J.; Dhar, S. S. Synthesis of SnO_2 Quantum Dots Mediated by Camellia Sinensis Shoots for Degradation of Thiamethoxam. *Toxicol. Environ. Chem.* **2020**, *102* (1–4), 186–196. https://doi.org/10.1080/02772248.2020.1776285.

(35) Lee, Y.-J.; Kang, J.-K.; Park, S.-J.; Lee, C.-G.; Moon, J.-K.; Alvarez, P. J. J. Photocatalytic Degradation of Neonicotinoid Insecticides Using Sulfate-Doped Ag_3PO_4 with Enhanced Visible Light Activity. *Chem. Eng. J.* **2020**, *402*, 126183. https://doi.org/10.1016/j.cej.2020.126183.

(36) Jansanthea, P.; Saovakon, C.; Chomkitichai, W.; Ketwaraporn, J.; Maneepong, S.; Chaiwong, N.; Jaisee, K.; Wansao, C.; Wanaek, A.; Pookmanee, P. Thiamethoxam Insecticide Degradation with a Leaf-Like Cupric Oxide Monoclinic Structure Synthesized via the Microwave Method. *Russ. J. Inorg. Chem.* **2021**, *66* (5), 667–678. https://doi.org/10.1134/S0036023621050089.

Conclusions and future perspectives

This thesis establishes the importance of monoliths with hierarchical porosity and unique channel structure and their superiority as photocatalysts. The environmental pollution caused by anthropogenic activities has grievous consequences as these pollutants have a detrimental effect on living beings. Of the numerous techniques to treat water pollution, photocatalysis has come across as the most promising route. However, the employment of powdered photocatalysts restrains the large-scale use of this method. Monolithic photocatalysts come as a savior in this situation which have better transport kinetics and easy recovery due to single rock like structure. The literature survey revealed that there is a dearth of studies where photoactive monolithic materials have been synthesized by wet impregnation method and later utilized for the photodegradation of recalcitrant organic pollutants like pesticides and pharmaceutical compounds.

The visible-light-driven monoliths were constructed by the wet impregnation of aqueous solution of suitable precursor metal salt into silica monoliths. In this context, four different monolithic photocatalysts in centimeter length scale (~0.7 cm in length and 0.5 in diameter) were synthesized in the thesis work i.e., WO_3/SiO_2, Sb_2S_3/SiO_2, MoO_3/SiO_2, and CuO/SiO_2 monoliths. The easy recovery after the photocatalytic treatment and high reusability is their most important attribute. All the monoliths had high surface area, porous morphology and multimodal porosity, and favorable optical properties. The performance evaluation and kinetic studies were conducted for the photocatalytic treatment of various organic pollutants like dyes, pesticides, and pharmaceutical contaminants. The influence of solution pH, concentration of catalyst, light source, and illumination area on the photodegradation was studied. The trapping experiments were also performed to know the photodegradation mechanism. The catalysts exhibited good efficiency compared to corresponding powdered materials ascribing to high surface area and increased number of active sites. Consequently, the increased light-harvesting ability facilitates the speeding up of the reaction kinetics on surface and transport kinetics. The comparison of all the prepared monoliths for the photodegradation of model pollutant MB is displayed in **Table 6.1**. All the prepared monoliths are comparable having favorable surface and optical properties.

But, the WO_3/SiO_2 monolith is still better than all as it exhibits maximum removal efficiency (97.5%) at optimum reaction conditions, making it the best catalyst.

Table 6.1. Comparison of the prepared monoliths for the photodegradation of MB.

Photocatalyst	Pollutant	Maximum percent degradation
WO_3/SiO_2	MB	97.5
Sb_2S_3/SiO_2	MB	92.5
MoO_3/SiO_2	MB	87.3
CuO/SiO_2	MB	86.2

Furthermore, the real wastewater analyses demonstrated that the monolithic catalysts have a high potential for real world application as these manifested decent results without using any physicochemical treatment as used by industries. The application of monolithic photocatalysts/materials can be extended to biological applications like antibacterial/antifungal studies. The inter-connected multi scale pores in monolithic catalyst are useful for gas phase reactions. Finally, a closed pack monolithic column can be designed which can be used for other environmental based applications like nitrogen fixation and CO_2 reduction.

List of Publications

1.1. Related to Ph.D. work (Objectives)

i. **Surbhi Sharma**, Soumen Basu, Highly reusable visible light active hierarchical porous WO_3/SiO_2 monolith in centimeter length scale for enhanced photocatalytic degradation of toxic pollutants, *Separation and Purification Technology*, 231 (2020) 115916. (IF=9.136)

ii. **Surbhi Sharma**, Soumen Basu, Fabrication of centimeter-sized Sb_2S_3/SiO_2 monolithic mimosa pudica nanoflowers for remediation of hazardous pollutants from industrial wastewater, *Journal of Cleaner Production*, 280 (2021) 124525. (IF=11.072)

iii. **Surbhi Sharma**, Soumen Basu, Visible-light-driven efficient photocatalytic abatement of recalcitrant pollutants by centimeter-length MoO_3/SiO_2 monoliths with long service life, *Applied Materials Today*, 23 (2021) 101033. (IF=8.663)

iv. **Surbhi Sharma**, Soumen Basu, construction of an efficient and durable hierarchical porous CuO/SiO2 monolith for synergistically boosting the visible-light-driven degradation of organic pollutants, *Separation and Purification Technology*, 279 (2020) 119759. (IF=9.136)

1.2. Review articles

i. **Surbhi Sharma**, Soumen Basu, Nagaraj P Shetti, Tejaraj M Aminabhavi, Waste-to-energy nexus for circular economy and environmental protection: recent trends in hydrogen energy, *Science of the Total Environment*, 713 (2020) 136633. (IF=10.753)

ii. **Surbhi Sharma**, Aayushi Kundu, Soumen Basu, Nagaraj P Shetti, Tejaraj M Aminabhavi, Sustainable environmental management and related biofuel technologies, *Journal of Environmental Management*, 273 (2020) 111096. (IF=8.910)

iii. **Surbhi Sharma**, Soumen Basu, Nagaraj P Shetti, Mohammadreza Kamali, Pavan Walvekar, Tejaraj M Aminabhavi, Waste-to-energy nexus: A sustainable development, *Environmental Pollution*, 267 (2020) 115501. (IF=9.988)

iv. Shelly Singla, **Surbhi Sharma**, Soumen Basu, Nagaraj P Shetti, Kakarla Raghava Reddy, Graphene/graphitic carbon nitride-based ternary nanohybrids: Synthesis methods, properties, and applications for photocatalytic hydrogen production, *FlatChem*, 24 (2020) 100200. (IF: 5.829)

v. **Surbhi Sharma**, Soumen Basu, Nagaraj P Shetti, Mallikarjuna N Nadagouda, Tejraj M Aminabhavi, Microplastics in the environment: occurrence, perils, and eradication, *Chemical Engineering Journal*, 408 (2021) 127317. (IF=16.744)

vi. Divya Monga[†], **Surbhi Sharma**[†], Nagaraj P Shetti, Soumen Basu, Kakarla Raghava Reddy, Tejraj M Aminabhavi, Advances in transition metal dichalcogenide-based two-dimensional nanomaterials, *Materials Today Chemistry*, 19 (2021) 100399. (IF: 7.613)

vii. Shelly Singla, **Surbhi Sharma**, Soumen Basu, Nagaraj P Shetti, Tejraj M Aminabhavi, Photocatalytic water splitting hydrogen production via environmental benign carbon based nanomaterials, *International Journal of Hydrogen Energy*, 46 (2021) 33696-33717. (IF: 7.139)

viii. **Surbhi Sharma**, Nagaraj P Shetti, Soumen Basu, Mallikarjuna N Nadagouda, Tejraj M Aminabhavi, Remediation of per- and polyfluoroalkyls (PFAS) via electrochemical methods, *Chemical Engineering Journal*, 430 (2022) 132895. (IF= 16.744)

ix. **Surbhi Sharma**, Soumen Basu, Nagaraj P Shetti, Kunal Mondal, Ashutosh Sharma, Tejraj M Aminabhavi, Versatile Graphitized Carbon Nanofibers in Energy Applications, *ACS Sustainable Chemistry & Engineering*, 10 (2022) 1334-1360. (IF=9.224)

1.3. Other publications

i. Jasminder Singh, **Surbhi Sharma**, Aanchal Rathi, Soumen Basu, Synthesis of Fe_2O_3/TiO_2 monoliths for the enhanced degradation of industrial dye and pesticide via photo-Fenton catalysis, *Journal of Photochemistry and Photobiology A Chemistry*, 376 (2019) 32-42. (IF=5.141)

- **ii.** Aayushi Kundu, **Surbhi Sharma**, Soumen Basu, Modulated BiOCl nanoplates with porous g-C_3N_4 nanosheets for photocatalytic degradation of color/colorless pollutants in natural sunlight, *Journal of Physics and Chemistry of Solids*, 154 (2021) 110064. (IF=4.383)
- **iii.** Love Dashairya†, **Surbhi Sharma**†, Aanchal Rathi†, Partha Saha, Soumen Basu, Solar-light-driven photocatalysis by Sb_2S_3/carbon based composites towards degradation of noxious organic pollutants, *Materials Chemistry and Physics*, 273 (2021) 125120. (IF=4.778)
- **iv.** Shelly Singla, **Surbhi Sharma**, Soumen Basu, MoS_2/WO_3 heterojunction with the intensified photocatalytic performance for decomposition of organic pollutants under the broad array of solar light, *Journal of Cleaner Production*, 324 (2021) 129290. (IF=11.072)
- **v.** **Surbhi Sharma**, Soumen Basu, Visible-light-induced photocatalytic response of easily recoverable Mn_2O_3/SiO_2 monolith in centimeter-scale towards degradation of ofloxacin: Performance evaluation and product analysis, *Chemosphere*, 307 (2022) 135973. (IF=8.943)

(† equal contribution)

1.4. Book chapter

- **i.** **Surbhi Sharma**, Soumen Basu, Silicon-based hybrid nanoparticles: An introduction, in: Silicon-Based Hybrid Nanoparticles, Elsevier, 2022: pp. 1–9. (ISBN: 9780128240076)

Conferences and Workshops

1. Oral presentation on the topic "**Enhanced Photocatalytic Degradation of Methylene blue by Hierarchical Porous WO_3/SiO_2 Monoliths**" at International conference, CHEMCON – 2018 held at NIT, Jalandhar on December 27-30, 2018.
2. Poster presentation on the topic "**Synthesis of Nanoflower like Sb_2S_3/SiO_2 Monoliths for Enhanced Photocatalytic Degradation of Methylene blue**" at national conference, RTCES – 2019 held at Punjabi University, Patiala on February 07-08, 2019.
3. Oral presentation on the topic "**Sb_2S_3/SiO_2 monolith at centimeter-level for photocatalytic abatement of thiamethoxam from aqueous media**" at International virtual conference, ACS Spring 2021 held online on April 5-16, 2021
4. DST & ACS virtual workshop "**Mastering the publishing process**" on July 28, 2020.
5. Basic series of the Web of Science Training & Certification program 2020.
6. Advanced series of the Web of Science Training & Certification program 2020